EUROPEAN ORGANISATION FOR NUCLEAR RESEARCH

Studies of Intermediate Vector Boson Production and Decay in UA1 at the CERN Proton-Antiproton Collider

UA1 Collaboration, CERN, Geneva, Switzerland

Aachen[1] - Amsterdam (NIKHEF)[2] - Annecy (LAPP)[3] - Birmingham[4] - CERN[5] - Harvard[6] - Helsinki[7] - Kiel[8] - Imperial College, London[9] - Queen Mary College, London[10] - Madrid (CIEMAT)[11] - MIT[12] - Padua[13] - Paris (College de France)[14] - UCRiverside[15] - Rome[16] - Rutherford Appleton Lab[17] - Saclay (CEN)[18] - Victoria[19] - Vienna[20] - Wisconsin[21] Collaboration

C. Albajar[5], M.G. Albrow[17], O.C. Allkofer[8], G. Arnison[17], A. Astbury[19], B. Aubert[3], T. Axon[9], C. Bacci[16], T. Bacon[9], N. Bains[4], J. R. Batley[10], G. Bauer[6], S. Beingessner[19], J. Bellinger[20], A. Bettini[13], A. Bezaguet[5], R. Bonino[4], K. Bos[2], M. Botlo[20], E. Buckley[6], G. Busetto[13], P. Catz[3], F. Cavanna[16], P. Cennini[5], S. Centro[13], F. Ceradini[16], D.G. Charlton[4], G. Ciapetti[16], S. Cittolin[5], D. Clarke[10], D. Cline[21], C. Cochet[18], J. Colas[3], P. Colas[18], M. Corden[4], J.A. Coughlan[17], G. Cox[4], D. Dau[8], .M. DeBeer[18], J.P. deBrion[18], M. DeGiorgi[13], M. Della Negra[5], M. Demoulin[5], .B. Denby[17], D. Denegri[5,18], A. DiCiaccio[5,16], F.J. Diez Hedo[11], L. Dobrzynski[14], J. Dorenbosch[2], J. D. Dowell[4], E. Duchovni[5], R. Edgecock[4], K. Eggert[1], E. Eisenhandler[10], N. Ellis[4], P. Erhard[1], H. Faissner[1], I.F. Fensome[10], A. Ferrando[11], M. Fincke-Keeler[19], P. Flynn[17], G. Fontaine[14], R. Frey[15], J. Garvey[4], S. Geer[6], A. Geiser[1], C. Ghesquiere[14], P. Ghez[3], C. Ghiglino[3], W.R. Gibson[10], Y. Giraud-Heraud[14], A. Givernaud[5,18], A. Gonidec[5], H. Grassmann[1], G. Grayer[17], J. Gregory[4], W. Haynes[17], S.J. Haywood[4], H. Hoffmann[5], D.J. Holthuizen[2], R.J. Homer[4], A. Honma[10], M. Ikeda[15], W. Jank[5], M. Jimack[4], G. Jorat[5], D. Joyce[15], P.I.P. Kalmus[10], V. Karimäki[7], R. Keeler[19], I. Kenyon[4], A. Kernan[15], A. Khan[9], W. Kienzle[5], R. Kinnunen[7], M. Krammer[20], J. Kroll[6], D. Kryn[14], P. Kyberd[10], F. Lacava[16], M. Landon[10], J.P. Laugier[18], J.P. Lees[3], R. Leuchs[8], S. Levegrün[8], S. Li[19], M. Lindgren[15], D. Linglin[3], P. Lipa[20], E. Locci[5], K. Long[5], T. Markiewicz[21], C. Markou[9], M. Markytan[20], M.A. Marquina[11], G. Maurin[5], J.-P. Mendiburu[14], A. Meneguzzo[13], J. P. Merlo[15], T. Meyer[5], M.-N. Minard[3], M. Mohammadi[21], K. Morgan[15], M Moricca[16], H.-G. Moser[1], A. Moulin[1], B. Mours[3], Th. Muller[5], A. Nandi[10], L. Naumann[5], P. Nedelec[14], A. Nisati[16], A. Norton[5], V.O'Dell[17], G. Pancheri[6], F. Pauss[5], C. Perault[3], E. Petrolo[16], G. Piano Mortari[16], E. Pietarinen[7], C. Pigot[18], M. Pimiä[7], A. Placci[5], J.-P. Porte[5], M. Preischl[8], E. Radermacher[5], J. Randsdell[15], T. Redelberger[1], H. Reithler[1], J.-P. Revol[12], J. Richman[5], D. Robinson[10], T. Rodrigo[11], J. Rohlf[6], C. Rubbia[5], G. Sajot[14], G. Salvini[16], J. Sass[5], D. Samyn[5], A. Savoy-Navarro[18], D. Schinzel[5], M. Schröder[8], A. Schwartz[6], W. Scott[17], C. Seez[9], T. P. Shah[17], I. Sheer[15], I. Siotis[9], D. Smith[15], R. Sobie[19], P. Sphicas[12], J. Strauss[20], J. Streets[4], C. Stubenrauch[18], D. Summers[21], K. Sumorok[6], F. Szoncso[20], C. Tao[14], A. Taurok[20], L. Taylor[9], I. ten Have[2], S. Tether[12], G. Thompson[10], E. Tscheslog[1], J. Tuominiemi[7], W. van de Guchte[2], A. van Dijk[2], B. van Eijk[2], J.P. Vialle[3], L. Villasenor[21], T.S. Virdee[9], W. von Schlippe[10], J. Vrana[14], V. Vuillemin[5], K. Wacker[1], H.D. Wahl[20], G. Walzel[20], .P. Watkins[4], A. Wildish[9], I. Wingerter[3], S. J. Wimpenny[5], X. Wu[12], C. E. Wulz[20], T. Wyatt[5], M. Yvert[3], I. Zacharov[2], N. Zaganidis[18], L. Zanello[16] and P. Zotto[13].

STUDIES OF INTERMEDIATE VECTOR BOSON

PRODUCTION AND DECAY IN UA1

AT THE CERN PROTON-ANTIPROTON COLLIDER

ABSTRACT

An extensive study of production and decay properties of charged and neutral Intermediate Vector Bosons (IVB) at the CERN proton-antiproton collider is presented. Intermediate Vector Bosons were detected in the electron, muon, and tau decay modes at centre-of-mass energies of 0.546 and 0.630 TeV. This paper is a summary, based on all the available data from the UA1 experiment from the running periods 1982-1985. Results are presented and compared with expectations of the Standard Electroweak Model and QCD-improved Drell-Yan annihilation processes.

The general conclusion is that there is an excellent agreement between the predictions of the Standard Model and our measurements.

1. INTRODUCTION

During 1982 and 1983 the UA1 experiment took data to find direct evidence for Intermediate Vector Boson production in proton-antiproton interactions at very high energy via the processes:

$$p + \bar{p} \rightarrow W^{\pm} (\rightarrow \mathscr{l}^{\pm} + \nu) \quad + X \qquad \mathscr{l} = e, \mu, \tau$$

$$p + \bar{p} \rightarrow Z^{0} (\rightarrow \mathscr{l}^{+} + \mathscr{l}^{-}) \quad + X \qquad \mathscr{l} = e, \mu$$

These first results firmly established the existence of the charged ($W^{\pm}$) and neutral (Z^0) Intermediate Vector Bosons [1-5]. The data were taken at a proton-antiproton centre of mass (CMS) energy $\sqrt{s}$=0.546 TeV. Analysis of these early data showed three basic features:

* the masses of the IVBs are in the range expected by the Standard Model [6],
* the production properties are consistent with the Drell-Yan mechanism [7] complemented by QCD corrections (fig. 1), and
* the decay properties of the IVBs are consistent with the Standard Model expectations [8].

These results were based on W and Z detection in both electron and muon decay channels. The analysis of the UA2 collaboration has led to the same conclusions [9].

In the subsequent data taking periods of 1984 and 1985 the CERN collider provided $p\bar{p}$ collisions at an increased CMS energy of $\sqrt{s}$=0.63 TeV, and with higher luminosity reaching a peak value of about $5 \cdot 10^{29} cm^{-2} sec^{-1}$. These data confirmed the earlier results and allowed a more detailed analysis of IVB properties. The masses of the $W^{\pm}$ and Z^0 were remeasured yielding a value of $\sin^2\theta_w$, where θ_w is the Weinberg angle, and of the ρ parameter of the Electroweak Standard Model [10]. The W$\rightarrow$ eν decay angular distribution was found to be consistent with the predictions of the V–A Standard Model [10,11]. The IVB longitudinal and transverse momentum distributions and the jet activity associated with IVB production were shown to be in agreement with QCD expectations [13]. Particular emphasis was put on the study of W's produced at large transverse momentum [14]. The τ decay mode of the W was also observed [15]. This result was part of an extensive study of missing transverse energy events, which are dominated by neutrino production [16]. The partial production cross-sections for the different IVB decay modes gave a test of lepton

universality at a large momentum transfer $Q^2=M_w{}^2$ [17]. Finally, we placed an upper limit on the number of light neutrino types having standard couplings to the vector bosons [11,17].

The present paper summarizes our final results on $W^\pm$ and Z^0 events, using all available data from 1982 to 1985. The results are compared with the results of experiment UA2 and with theoretical expectations from the Electroweak Standard Model and QCD.

2. THE DETECTOR. PARTICLE IDENTIFICATION, ENERGY AND MOMENTUM MEASUREMENTS

The main IVB signature in $p\bar{p}$ collisions is the production of large p_T leptons, accompanied by large missing transverse energy in the case of W production. We first describe the UA1 detector and then the lepton (e, μ, τ, ν) identification capability, which is essential for the detection of W/Z bosons. As the determination of Standard Model parameters strongly depends on electron energy measurements, we discuss this feature in greater detail. Finally, we also discuss the limitations of the present apparatus.

We use the following notation: the x-axis is the direction of the antiproton beam; ϕ is the azimuthal angle around the beam axis; θ is the polar angle with respect to the outgoing antiproton beam; η is the pseudorapidity; $\Delta R = \sqrt{(\Delta\eta^2 + \Delta\phi^2)}$ is the distance in the (pseudorapidity, azimuthal angle) plane, with ϕ in radians.

2.1 The detector

The UA1 detector is a general purpose detector [18] designed to study $p\bar{p}$ collisions at the CERN $p\bar{p}$ collider and to explore IVB physics. It provides:

A) Tracking and momentum measurements of charged particles in the central drift chamber (CD),

B) Electromagnetic and hadronic calorimetry,

C) External drift chambers for muon identification and tracking,

D) Iron absorber walls, instrumented with limited streamer tubes for improved muon measurements.

A side view of the UA1 apparatus is shown in fig. 2. Protons and antiprotons in

4

bunches of about 30 cm length collide at the centre of the apparatus. The interaction region is inside a stainless steel beam pipe of ≈130 mm inner diameter with 0.15 mm thick walls. The pipe is corrugated with a maximum outer diameter of 146 mm. The interaction region is surrounded by successive layers of special purpose detectors. The tracking and magnetic analysis is made in the central drift chamber detector (a in fig. 2), where charged particle tracks are detected in the range $|\eta| \leq 3$. The central detector is completely surrounded by lead/scintillator electromagnetic calorimeters (b in fig. 2) designed to detect electrons and photons and measure their energy. Outside the electromagnetic calorimeters is a magnet coil (c in fig. 2), which produces a uniform horizontal field of 0.7 T in the region of the central detector and electromagnetic calorimeters. The thickness of the coil has been minimized in terms of absorption length λ_a by distributing the coil evenly around the inside field volume and by using aluminium rather than copper. The 13 cm of aluminium represent only 0.34 λ_a which is a 40% improvement over the electrical equivalent of copper. This led to the "warm coffin design" shown in fig. 3, which also has the advantage of providing a very uniform field.

Outside the coil is a large iron-scintillator sandwich hadron calorimeter (d in fig. 2), which also serves as the return yoke of the magnet. This is in turn surrounded by an absorber and drift chambers (e in fig. 2) used to identify muons that pass through the electromagnetic and hadron calorimeters. In the forward and backward regions, within 5° to the beam direction, there are additional drift chambers, electromagnetic calorimeters and hadron calorimeters to detect particles with small emission angles down to 0.2° (f and g in fig. 2).

Two sets of scintillator hodoscopes, one in the proton and the other in the anti-proton direction, are used to provide a pretrigger when at least one hit occurs in each hodoscope in coincidence with a beam crossing. The pretrigger records 96±2% of all non-diffractive inelastic interactions.

A)   The Central Drift Chambers

Trajectories of charged particles are measured in the central detector (CD), a large volume imaging drift chamber assembly, (25 m^3, 6125 sense wires) surrounding the interaction region [19].

The CD is composed of six independent semi-cylindrical chambers assembled to form a cylinder, 5.8 m long and 2.3 m in diameter, covering the polar angle range from 5°

to 175° with respect to the beam direction (fig. 4).

The 6125 sense wires and 17000 field-shaping wires are parallel to the magnetic field. They are organized in horizontal planes in the four forward modules and vertical planes in the two central ones. This geometry has been chosen to give an approximately constant density of points along the tracks over the total detector volume. The wire configuration has been designed to solve directly the "left-right" ambiguity inherent in the drift time measurement [19]. A schematic view of the arrangement of the six modules is shown in fig. 4.

The drift gaps are 18 cm wide. With an electric field of 1.5 kV/cm and a gas mixture of 40% argon and 60% ethane at atmospheric pressure, the drift velocity is 5.3 cm/μs. The drift angle due to the magnetic field is 23° with respect to the electric field direction. All drifting electrons are collected in 3.6 μs, a time smaller than the interval between two successive bunch crossings.

Space points are measured by recording the drift time and the charge division along the wire. The readout system records continuously, in "real time", the information on the drift time, charge division and pulse height from both ends of each wire with fast encoders (FADCs) [20]. A schematic representation of the basic principles of the readout is shown in fig. 5.

The trajectory of a charged track is measured, on the average, at over 100 space points. The momentum is determined by the deflection in the magnetic field. The sagitta in the plane normal to the magnetic field is measured with the drift time, which is two orders of magnitude more precise than the charge-division coordinate ($\Delta L/L = 1.5\%$). The momentum accuracy for high-momentum tracks is limited by systematic errors on the chamber alignment (≤ 100 μm) and by the diffusion of the drifting electrons (≤ 300 μm). This results in a momentum uncertainty of $\Delta p/p^2 = 0.005$ (GeV/c)$^{-1}$ for a 1 m long track perpendicular to the B-field.

The CD information has been fundamental in determining the charged particle topology of an event and, in particular, the isolation properties for lepton tracks. The determination of the lepton charge is essential, for example, to test the V-A aspect of the $W \rightarrow \ell \nu$ decays, and in establishing B^0- $\overline{B}^0$ mixing with equal sign dimuons [46].

B) Calorimetry

Surrounding the CD is the lead/scintillator electromagnetic calorimeter. It consists of two parts (see Table 1).

i) A cylindrical calorimeter, 6 m long with an inner diameter of 2.72 m, covers the region $25^\circ < \theta < 155^\circ$. It consists of 48 semi-cylindrical half shells, called "gondolas", 24 on each side of the beam axis (fig. 2b). The width of each gondola is 22.5 cm (fig. 6a). The device is a sampling type calorimeter, made of alternating layers of scintillator (1.5 mm) and lead (1.2 mm) and organized in four compartments in depth to sample the longitudinal shower shape [21].

The scintillation light at 380 nm wavelength from all four segments is absorbed by wavelength shifters along the edges of the scintillator; it is re-emitted at 480 nm and transmitted to photomultipliers via light-guides. Each segment is seen by four photomultipliers located outside the magnet.

The light attenuation in the scintillators and wavelength shifters permits us to reconstruct the position of the deposited energy in space in cases where a single shower dominates. Comparing the top and bottom photomultipliers gives the azimuthal angle ϕ with a resolution $\sigma(\phi)(rad) = 0.24 \ E^{-1/2}(GeV)$. Similarly, comparing left and right photomultipliers along the beam direction determines the x-coordinate to a precision $\sigma(x) = 6.3$ cm $E^{-1/2}(GeV)$. These results were obtained using an electron test beam. The energy resolution was $\sigma(E)/E = 0.15 \ E^{-1/2}(GeV)$ (fig. 7).

The separation between electrons and pions was also studied in a test beam by observing the fraction of energy deposited in the hadron-calorimeter module placed behind the gondola as a function of beam energy and angle of incidence [40].

ii) The end faces of the CD are covered by end-cap electromagnetic calorimeters ("bouchons") in the regions $5^\circ < \theta < 25^\circ$ and $155^\circ < \theta < 175^\circ$ (b in fig. 2 and fig. 8). Each "bouchon" is split vertically into two halves, each half being divided azimuthally into 16 equal sectors (petals). The petal, a sandwich of lead (4 mm) and scintillator (6 mm), is segmented into four parts in depth (see fig. 8).

As in the gondolas, wavelength shifters transmit the light to the photomultipliers [22]. The attenuation length of the scintillator has been chosen to match the variation of $\sin\theta$ over the radius of the calorimeters, so as to directly measure in first approximation $E_T = E\sin\theta$, rather than the true energy deposition E. This allows the amount of transverse energy deposited to be read out directly

for triggering purposes.

After the first two segments, at a depth of 11 radiation lengths, a position detector is located to measure the shower position. It consists of two planes of orthogonal proportional tubes of 2x2 cm^2 cross-section. It locates the centre of gravity of electromagnetic showers to an accuracy of about ±2 mm in space, and gives a rough measurement of the deposited energy.

The hadron calorimeter (d in fig. 2) surrounds the electromagnetic calorimeter and covers the angular range 5°<θ<175°. It is formed of two types of modules: in the central region there are 16 C-shaped modules (d in figs 2 and fig. 6b), 8 on each side of the beam; and in the end-cap regions 12 I-shaped modules close the detector, 6 on either end. The C's also serve as the return yoke of the magnet. The hadron calorimeter (Table 1) is of the iron-scintillator sandwich type: 1 cm scintillator plates alternated with 5 cm iron plates. Each C is subdivided into 12 sections in azimuth and two segments in depth: a front stack with 7 scintillator plates and a rear stack with 8 scintillator plates with a total iron thickness of 80 cm. As in the electromagnetic calorimeter, the light is transferred via wavelength shifter bars and light-guides to the photomultipliers, two per stack. Each I (d in fig. 3) is subdivided into 6 stacks, each stack into two segments in depth. The 16 stacks nearest to the beam are further subdivided into four. The number of scintillators is in this case 12 for the front segments and 11 for the rear segments, all separated by 5 cm iron plates. The total thickness of iron (120 cm) is therefore greater than for the C's because of the larger average energy in the forward region.

A test module has been studied in a test beam. The energy resolution, together with the electromagnetic calorimeter placed in front, was found to be σ(E)/E=0.8 E$^{-1/2}$(GeV).

Additional calorimetry, both electromagnetic and hadronic, and track detection extend to the forward regions of the experiment, down to 0.2° (see f and g in fig. 2, and Table 1).

Outside the central part of the apparatus, there is a calorimetrized compensator magnet ("CALCOM") on each side (f in fig. 2). The Calcom has both an electromagnetic and a hadronic portion. The electromagnetic calorimeter is subdivided into four segments in depth, each one made out of lead plates (3 mm) and scintillator plates (3 mm). After the first segment, a position detector (made of proportional chambers) registers the electromagnetic showers. The return yoke of the compensating magnet is part of the hadronic calorimeter. Its 4 cm iron plates alternate with 8 mm scintillator plates. The whole calorimeter is segmented

in 6 parts in depth with a position detector behind the first one.

Finally two "very forward" detectors [22] are located at ±12m from the interaction point (g in fig. 2). Each of these calorimeters has an electromagnetic and hadronic part. The electromagnetic part is subdivided into four segments in depth and into four sectors in ϕ with 90° opening angles around the beam pipe. The hadronic part is also subdivided into four sectors in ϕ and five segments along the beam direction. Also in these calorimeters, the scintillation light is transferred via wavelength shifters and light guides to the photomultipliers [22].

C) Muon identification: External drift chambers

Fig. 9 shows the general layout of the muon detectors. Muons are filtered in the return yoke of the magnet (the hadron calorimeter) supplemented by additional iron shielding (j, h in fig. 9), and identified in two sets of detectors, made of planes of drift chambers (e, e' in fig. 9) and limited streamer tubes (i, i' in fig. 9).

The muon detectors cover about 70% of the solid angle over the pseudorapidity range $|\eta| \leq 2.3$. In the central region, muons traverse the electromagnetic calorimeter (gondolas), then 80 cm of iron of the hadron calorimeter and 60 cm (40 cm in the bottom) of magnetized iron (h in fig. 9). In the end-cap region they traverse the bouchons, then 120 cm of iron of the hadron calorimeter and 60 cm of additional shielding (j in fig. 9).

The chambers are made of extruded aluminum tubes with drift cells of 150 mm x 45 mm. Each chamber is made of two orthogonal projections with two planes per projection. Adjacent planes have staggered drift cells to solve the "left-right" ambiguity of the drift time measurement. With the exception of those on the bottom, the chambers [23] are arranged in modules of about 4 x 6 m². Each muon module consists of two chambers separated by a lever arm of 60 cm (fig. 10). Due to limited space, the muon modules on the bottom consist of one chamber made of four layers of parallel drift tubes.

With an average electric field of 1.2 kV/cm and using the same gas mixture as the central detector (40% argon - 60% ethane), the drift velocity is 5.3 cm/μs. The space resolution, averaged over the crossing angle, is better than 0.5 mm per plane. The coordinate along the wire can be obtained with a resolution of 0.3 m using the time differences of the pulses arriving at the two ends of the wire.

D) Iron absorber instrumented with limited streamer tubes

For the 1984 and 1985 run periods, the muon detection system has been upgraded with layers of limited streamer tubes [24]. In the side walls of the central region (h in fig. 9), three layers of tubes (i in fig. 9) are interspaced with 20 cm blocks of magnetized iron (fig. 11a). The magnetic field is 1.25 T, perpendicular to the main dipole field. In the end-cap region two layers of tubes (i' in fig. 9) are placed between the hadron calorimeter and the forward iron shielding (j in fig. 9). On the bottom one layer is added before the drift chambers. Each layer consists of two orthogonal planes of streamer tubes (fig. 11b). The coordinate parallel to the wires is measured by digitizing the induced charge distribution on cathode strips orthogonal to the wires. The cathode strip pitch is 12 mm and the space resolution is about 1 mm. The resolution on the momentum measurement in the side walls is 30% at 8 GeV/c and reaches 100% at 25 GeV/c using only the hits in the limited streamer tubes and external muon chambers as tracking segments, i. e. without the CD information (see fig. 11a).

2.2 Electron trigger, identification and calibration

The electron hardware trigger [25] used throughout the data taking required the presence of an electromagnetic cluster (one or two adjacent electromagnetic cells) with transverse energy in excess of 10 GeV, at an angle of more than 5° with respect to the beam axis (i.e. $|\eta|<3$). Using on-line IBM 168E emulators, criteria on the electromagnetic shower depth profile and lepton isolation are applied to these clusters in the 10-15 GeV range, to reduce the background in recorded electron triggers. This last procedure was implemented after the 1983 run. The isolated single-electron trigger efficiency, including the 168E on-line selection, is shown in fig. 12a as a function of the electromagnetic transverse energy (E_T). For 15 GeV electrons the trigger efficiency is $(96\pm2)\%$.

Electrons are identified [10-12] by the presence of a high momentum charged track with a matching electromagnetic cluster, satisfying the following electron selection criteria:

*   matching in position and momentum between the electromagnetic cluster and the charged track. Fig. 13 shows that there is a good matching between energy and momentum measurement for electrons in the UA1 detector. The observed asymmetry is due to photon bremsstrahlung [50,51],

*   longitudinal shower profile compatible with electron energy deposition. Energetic

10

electrons deposit almost all their energy in the first three of the four segments in depth of the lead-scintillator shower calorimeter (total of $27X_0$ deep at normal incidence), and give only small leakage into the two hadronic compartments. The measured depositions are compared with test beam and Monte Carlo results. This provides a powerful test on the electron shower profile, therefore giving good rejection against $\pi^{\pm}$ and $\pi^{\pm}\pi^0$ overlaps,

* isolation around the electron. This is required to further reduce the dominant background coming from hadronic jets (either converted γ from π^0, or a high p_T charged track overlapping with a π^0). The isolation requirement is that there be less than a given maximum energy deposition in a cone $\Delta R = \sqrt{(\Delta\phi^2 + \Delta\eta^2)}$ around the electron axis. The test is made using both the calorimeter and the central detector. This requirement does not affect the selection efficiency very much because leptons from W and Z decays are expected to be isolated.

For electrons from W and Z decays the energy measurements from the calorimeter is better than the momentum measurement from the CD. Therefore the precision in the electromagnetic calorimetry is essential for the determination of Standard Model parameters. Uncertainties on the electron energy come from :

* intrinsic electromagnetic calorimeter resolution, affected by decreasing light collection as the scintillator ages. The resolution $\sigma(E)/E$ has deteriorated from $\approx 15\%/\sqrt{E}$ (1983) to $\approx 21\%/\sqrt{E}$ (1985) due to this effect.

* cell-to-cell calibration differences which are partly corrected by three methods: surveying the calorimeter with an intense ^{60}Co source, cosmic ray muon studies and studies with minimum-bias events.

* non-uniform response over the area of each calorimeter cell, due to short attenuation lengths for light collection. A surface mapping is done for each electromagnetic calorimeter module using a ^{60}Co source [40,41,42].

* pile-up contribution from the rest of the event. This is not negligible because of the limited granularity in ϕ of the calorimeter.

* uncertainty in the absolute energy scale and time dependence of the calorimeter response. An absolute calibration in an electron test beam has been made for a spare calorimeter element and transferred to the experiment using a reference ^{60}Co source. The long term time dependence of the response is also followed using the ^{60}Co source. The short term time variations are monitored through a laser plus optical fibre calibration system.

* uncertainty in the corrections from the cosmics, ^{60}Co, and laser calibrations.

The various contributions to the uncertainty in the electron energy measurement are summarized in Table 2. The resulting overall systematic uncertainty amounts to 3.2%.

2.3 Muon identification, measurement and calibration

A muon leaving the interaction region first passes through the central drift-chamber, then the electromagnetic calorimeter and the magnetized iron hadron calorimeter. Finally, after traversing at least 60 cm of additional iron in the central region ($\geq$1m in front regions) it enters the muon chambers. This gives about $9/\sin\theta$ (for $\theta > 25^0$) nuclear interaction lengths of material in total, where θ is the emission angle with respect to the beam axis [4,5,23]. The iron absorber wall in the central region is magnetized and instrumented with limited streamer tubes.

Muon candidates are selected by a hardware fast trigger requiring a track in the muon chambers pointing to the interaction region within a cone of $\pm$150 mrad. The single muon trigger covers a rapidity range varying from $|\eta|\leq$1.4 at high luminosity to $|\eta|<$ 2.3 at low luminosity. For this first level trigger just the pattern of tubes hit is used. This requirement, taking into account the mass of the absorber, is roughly equivalent to an approximate p_T cut on the muon of $p_T^\mu \geq$ 2 GeV/c (fig. 12b). Further event selection (2nd level trigger) is done on-line with 168E emulators, where the actual drift time information allows the pointing requirements to be sharpened to about $\pm$60 mrad. This reduces the trigger rate by a factor 3.7.

Muon identification is done by extrapolating high p_T tracks from the CD to the muon chambers. The geometric matching between the CD track and the outer muon track segment has been extensively studied with cosmic rays.

The muon momentum, is given by the track curvature in the CD. In a second method, the deflection in the magnetic return yoke, determined from the track position and track angle in the muon chambers and in the limited streamer tubes whenever available, is also used in fitting the momentum. This overall fit gives a momentum consistent with the CD measurement alone (fig. 14) and reduces the measurement error. Isolated muons are also characterized by a minimum ionisation energy deposition in the traversed calorimeter cells.

Background to the muon signal comes mainly from four sources:

  *   cosmic rays,

*   punch-through and leakage from hadronic showers (which has been measured and found to be negligible [23]),
*   stray particles leaking through gaps and
*   muons from decays in flight of pions and kaons.

2.4 Neutrino identification and measurement

In principle, the existence of non-interacting particles can be inferred from the momentum and energy measurement of all detected particles. In $p\bar{p}$ interactions, however, a large fraction of energy is carried off by particles with high momentum and low p_T, which escape detection by remaining in the beam pipe. For this reason only the transverse component of the energy imbalance can be measured. For an energy deposition in a calorimeter cell, E, we define an energy vector

$$\vec{E} = E \cdot \vec{u} \qquad (2.1)$$

where $\vec{u}$ is a unit vector pointing from the interaction point to the reconstructed position of the calorimeter hit. The vector sum of the $\vec{E}$ vectors for all calorimeter hits is formed. $\vec{E}_T$ is the transverse component of this vector. The transverse missing energy is then defined as $\vec{E}_T^{mis} = - \vec{E}_T$.

The emission of an energetic neutrino is signalled by a large value of the missing transverse energy $\vec{E}_T^{mis}$. The observation of events with large missing transverse energy was crucial in the discovery of $W \rightarrow e\nu$ decays [1]. The neutrino transverse momentum measurement is considered valid if:

*   the missing transverse energy $\vec{E}_T^{mis}$ does not point at a detector crack (ϕ within 15° from the vertical plane), and
*   no high p_T track points to a calorimeter crack (ϕ within 5° from the vertical plane).

In minimum bias events, the transverse components ΣE_x and ΣE_y of $\vec{E}_T^{mis}$ are gaussian distributed and give a resolution in E_T^{mis} of 0.7 $\sqrt{\Sigma E_T}$, where ΣE_T is the scalar sum of all total transverse energy depositions. The measurement of $\vec{E}_T^{mis}$ is a powerful tool in the search for new physical phenomena [15,16].

Muon detection and momentum measurement allows us to apply the transverse energy balance method even in the presence of a muon which escapes the calorimetric

13

measurement. In muon events, the transverse momentum of the neutrino is defined as:

$$E_T^{mis} \equiv \vec{p_T}^\nu = - \vec{p_T}^\mu - \vec{E_T}.$$ (2.2)

where $\vec{p_T}^\mu$ is the muon transverse momentum vector measured in the CD. The muon energy deposition in the calorimeters is subtracted from $\vec{E_T}$.

2.5 Tau trigger and identification.

An inclusive selection of missing transverse energy events provides not only the sample of $W \to e\nu$ decays, but also a significant number of additional events in which the missing transverse energy recoils against one or more high transverse energy jets [15,16]. Part of that sample comes from the decay

$$W \to \tau \nu_\tau$$ (2.3)

followed by the hadronic τ decay modes:

$$\tau \to \pi^{+(-)} + n\pi^0 + \nu_\tau \text{ and } \tau \to 3\pi^{+(-)} + n\pi^0 + \nu_\tau$$ (2.4)

The jets from the hadronic decay of the tau have low masses and low charged-track multiplicity. The experimental signature for $W \to \tau \nu_\tau$ events consists therefore of a highly collimated hadronic jet approximately back-to-back with a significant missing transverse energy from the ν_τ's.

In the 1984-1985 data-taking period the hardware trigger used for the selection of τ candidates required one of the following conditions to be satisfied:

* an electromagnetic transverse energy trigger with $E_T > 10$ GeV in two adjacent e.m. cells
* a jet trigger of $E_T > 25$ GeV in $|\eta| < 2.5$
* a jet trigger of $E_T > 15$ GeV, together with a transverse energy imbalance > 17 GeV between the two lateral halves of the apparatus.
  The transverse energy imbalance trigger was not used in the 1983 run.

2.6 Jet detection

Hadronic jets are identified by the standard UA1 jet-finding algorithm [26] with a transverse energy initiator of 1.5 GeV, and are retained if they have a transverse energy in excess of 7 GeV and the axis lies within the pseudorapidity interval $|\eta|<2.5$. A detailed Monte Carlo comparison has been made between reconstructed jets and the corresponding parent partons. The systematic uncertainty on the jet absolute energy scale is about 9%.

3. MONTE CARLO EVENT GENERATION AND SIMULATION

Monte Carlo programs have been extensively used to study the detector response, acceptance and trigger efficiencies for events (physics and background) produced in $p\bar{p}$ collisions. Events have been generated using the ISAJET program [27] tuned to agree with observed features of the data in the experiment. ISAJET provides a Drell-Yan model for IVB production with non-scaling structure functions. The IVB production is calculated using the lowest order Drell-Yan process (fig. 1a) and additional processes at the order α_s (fig. 1c,1d):

$$q + g \rightarrow W/Z + q \qquad (3.1)$$
$$q + \bar{q} \rightarrow W/Z + g.$$

These QCD bremsstrahlung processes may give rise to large transverse momenta for the intermediate vector bosons (p_T^{IVB}). These contributions can be reliably calculated for large p_T^{IVB} but diverge as $p_T^{IVB} \rightarrow 0$. Therefore a parametrization with an appropriate low p_T cutoff is introduced in order to reproduce the p_T^{IVB} behaviour predicted by Altarelli et al. [28]. The parametrization is normalized to get an integrated cross-section close to the measured one.

Three uncertainties affect the calculation of the IVB production:

* uncertainties in the appropriate quark and gluon momentum distributions;
* the choice of the four-momentum transfer scale, Q^2, and the Λ_{QCD} parameter, which affects the Altarelli-Parisi evolution [29] of the structure functions to the chosen Q^2 value;
* contributions associated with higher order diagrams, i.e the "K-factor".

15

Different sets of structure functions are available and have been used in the analysis, namely parametrizations by :

* Eichten et al. [30] with Λ_{QCD}=0.2 GeV(EHLQ1) and Λ_{QCD}=0.4 GeV (EHLQ2); normally, EHLQ1 is used in the ISAJET event generation;
* Duke and Owens[31] with Λ_{QCD}=0.2 GeV(DO1) and Λ_{QCD}=0.4 GeV (DO2);
* Glück et al.[32] with Λ_{QCD}=0.4 GeV (GHR);
* Diemoz et al.[33] with Λ_{QCD}=0.3 GeV (DFLM).

The Q^2 scale chosen is $Q^2=M_W^2$. Contributions from higher order processes have been estimated to be about 30% [28] and are thus much smaller than for Drell-Yan processes measured at SPS and ISR energies where K$\approx$2.5 [34].

Incoherent initial-state QCD bremsstrahlung giving rise to multi-jet events is generated by ISAJET. Quarks and gluons are assigned virtual masses of order p_T^W , which are dissipated in further radiation processes. The partons are evolved using the basic QCD branching processes q$\rightarrow$ qg, g$\rightarrow$ gg, g$\rightarrow$ q$\bar{q}$ [35]. This branching approximation correctly describes the leading-log scaling violations of the structure functions and satisfies the Altarelli-Parisi evolution of partons. The partons generated during evolution acquire successively lower virtual masses and the evolution stops at a cutoff of about 6 GeV. Below this value the hadronization is described in a non-perturbative independent fragmentation model [36].

The combination of the parton cascade and the fragmentation models reproduces many features of the measured jet fragmentation properties at the p$\bar{\text{p}}$ collider [37]. Extensive QCD studies in the context of heavy quark production and decay have been made in the search for heavy flavour (top) events [47,48].

The coupling of the W to fermions is described by a pure V-A current, while the Z has the appropriate mix of axial and vector couplings. If not stated otherwise, the Weinberg angle used in ISAJET corresponds to $\sin^2\theta_w$=0.214, and the vector bosons are assigned masses of 83.4 GeV/c^2 and 94.1 GeV/c^2. We kept these values right from the beginning of the analysis to be consistent in the various Monte Carlo simulations. The experimental results are not sensitive to these assumptions.

After a hard scattering process the remaining constituents, spectator partons of the proton (antiproton), give rise to "beam jets", which are handled by a mechanism similar to that for producing non-diffractive minimum bias events at collider energies. A correct

simulation of the spectator parton behaviour is required because the isolation of the charged and neutral leptons is used as an IVB selection criterion. Parameters which control the spectator activity in the Monte Carlo program have been adjusted to reproduce the observed global multiplicity, mean transverse momentum and transverse energy flow in high E_T events [38].

For event generation and simulation a "randomized W decay" technique ("semi" Monte Carlo) is also used. In an identified real W event the track and energy deposition of the charged lepton are removed, leaving the recoiling system and the spectator event. A random (V-A) decay of a W is then generated and superimposed on the event, subject to the constraints of energy and momentum conservation. In the same way, real W events can be replaced by "randomized Z decays", with the Z retaining the same momentum vector as that of the replaced W. These "mixed" events are generated with large statistics and provide a realistic description of the spectator system and initial state bremsstrahlung.

Backgrounds from processes involving the production of energetic leptons (heavy flavour production with semileptonic decay, or instrumental fluctuations in two-jet events) have been generated with the same method.

The EUROJET Monte Carlo [39] has been used to study contributions from top-quark production and decay, in particular for cross-sections, as it provides a better approximation of higher order QCD corrections.

In all cases the generated events were passed through a program to simulate fully the UA1 detector response. They were reconstructed, selected and analysed with the same programs as the data.

4. EVENT DETECTION, RECONSTRUCTION AND SELECTION; DATA SAMPLES

In this final analysis, three improvements have been made:

*   the CD and calorimeter calibrations have been improved,
*   the reconstruction and selection algorithms have been optimized, and
*   the background contributions have been re-evaluated.

As a consequence, selection criteria, event numbers and efficiencies differ marginally from previous publications. Further, different selection criteria have been used in the various analyses described below so that the quoted number of events varies from one section to another in this paper. Data from the years 1982 and 1983 were taken at √s=0.546 TeV, and the 1984 and 1985 data at √s=0.630 TeV. The integrated luminosity is known to about ±15%.

4.1 Electron decay modes

We present final results on the selection of W→ ev and Z→ ee candidates. Previous results were given in refs. [10,11,13].

i) W→ ev

To identify W→ ev decays in the UA1 detector, we require that an event contains an energetic isolated electron, with transverse energy greater than 15 GeV and that the missing transverse energy (neutrino emission) is also greater than 15 GeV. Further selection criteria, mainly validating the electron signature, have been applied to reduce the background (Table 3). The full procedure to select the W→ ev sample [11,13] is summarized in Table 4a. The efficiency of the selection criteria has been estimated from Monte Carlo events generated according to the Standard Model as described in Section 3. It is estimated to be (61±1.5)%. The uncertainty in the efficiency is due to the uncertainties in the structure functions and the Q^2 scale.

The selection efficiency depends on p_T^W. The threshold cut on the electron and neutrino transverse energies (E_T^e, E_T^v >15 GeV) and the isolation requirement for the electron lead to a loss of efficiency at high p_T^W. The correction factor including the effects of efficiency and resolution is shown in fig. 15. It is obtained from the ratio of generated to reconstructed and selected W→ ev Monte Carlo events. W events are weighted for overall efficiency according to this curve when they are used in any physics distribution.

Our selection procedure leads to a sample of 240 W→ ev events at √s=0.630 TeV for an integrated luminosity of 568 nb⁻¹ (Table 10). The 59 events at √s=0.546 TeV listed in Table 10 were obtained with slightly different selection and calibration criteria [10,13].

The W→ ev selection just discussed has been used with slight variations in some

specific parts of the analysis, as for cross-section and mass determinations. The details of these variations appear in refs. [40,41,42] and lead to similar W event samples. In particular, the selection of ref. [41], based on an event quality parameter which combines criteria similar to those in Tables 2 and 3a, is used in this paper to study the QCD-related aspects of W/Z production.

The two main background sources contributing to the W sample are: i) QCD jets, and ii) $W \to \tau \nu$ followed by $\tau \to e \nu \nu$ and $\tau \to \pi^{\pm}\pi^0 \nu$ decay modes (Table 9). The QCD background to W events comes partly from jets involving $\pi^{\pm}\pi^0$ superpositions which fake electrons, plus an apparent missing transverse energy in excess of 15 GeV caused by fluctuations in the calorimeter response. The estimate of this background is related to the resolution on the energy balance in the event and on the spatial and shower profile resolution of our electromagnetic calorimeter for $\pi^{\pm}\pi^0$ superpositions [1,3,11,13]. Note that the accuracy of the energy measurement in the end-cap calorimeter (bouchon) was more affected by ageing than the gondolas. The reduction in the background contribution to the W sample in the data of 1984-85, by comparison with that of 1982-83, is due partly to the change of the scintillator plates in the end-cap calorimeter and partly to the more stringent selection criteria used for the data of 1984-85. The background coming from τ decays has been estimated using our W selection procedure on Monte-Carlo generated events followed by a full detector simulation. The possible contribution from top-quark production and decay was studied as a function of the top quark mass M_t. The contribution is expected to be about 3% for a light top quark (≈ 44 GeV/c^2), and decreases with increasing top quark mass.

In figs. 16a,b we show the electron and neutrino transverse energy distributions for the selected events, with the expected background contributions. One can see that all background contributions populate the lowest part of the transverse energy spectra. The background-free part of the transverse mass spectrum is selected to obtain the W mass by requiring both the electron and neutrino transverse energies to be above 30 GeV.

ii) $Z^0 \to e^+e^-$

The requirements used to select $Z \to e^+e^-$ events are similar to those used in the $W \to e\nu$ analysis, but are less stringent because the signal is cleaner (Table 4b). Two electromagnetic clusters are required, with at least one of them satisfying the isolated electron criteria used in the $W \to e\nu$ selection. The second electromagnetic cluster (two adjacent cells in excess of 8 GeV) has to satisfy looser isolation and electromagnetic shape requirements. In addition the two-cluster invariant mass is required to be larger than

19

70 GeV.

We are left with a sample of 29 Z → e^+e^- candidates (Table 10) for the √s=0.630 TeV data. The 4 events at √s=0.546 TeV entered in Table 10 were obtained with slightly different selection and calibration criteria [10,13].

Let us now consider the background processes contributing to Z → e^+e^- events. After relaxing the mass cut, the invariant mass distribution for the extended sample of electron-positron candidates is shown in fig. 17. The experimental distribution below 60 GeV/c^2 is largely due to QCD jet fluctuations faking electrons, and to a few e^+e^- Drell-Yan pairs. Above 60 GeV/c^2 this contribution is negligible, so only W or Z related backgrounds appear to be relevant. The most important contribution comes from Z → $\tau^+\tau^-$, where both τ's decay to $e\nu_\tau\nu_e$, and from semileptonic decays of b and c quarks. Together they contribute ≈ 0.2 events to the mass region kept for Z analysis. Thus, the Z → e^+e^- sample may be considered to be essentially background free.

4.2 Muon decay modes

We present results on 67 W→ $\mu\nu$ and 21 Z → $\mu^+\mu^-$ events, beginning with a summary of the main selection requirements and principal features of the data [4,5,43,44,45]. The selection starts from an inclusive single muon event sample obtained by requiring very loose criteria:

* a central detector track with projected length of ≥40cm in the plane perpendicular to the magnetic field and having a minimum of 20 points,
* a fair quality muon track in the muon chamber, and
* matching between the extrapolated CD track and the muon chamber track.

This procedure selects about 40000 events with a muon candidate of p_T^μ ≥6 GeV/c. A detailed study of all known muon sources to this sample has been performed [46,47,48,49]. Once we subtract the background from π/K decays, the inclusive muon spectrum for p_T^μ ≤20 GeV/c is well understood in terms of semileptonic decays of heavy flavours, DY, Υ, J/ψ, while at larger p_T^μ the W and Z contributions dominate.

i) W→ μν

Following off-line reconstruction, the selection criteria are tightened by requiring a good quality matching track in the central detector with p_T>15 GeV/c. This track must be isolated in the central detector where the summed p_T of other tracks in a cone of $\Delta R \leq 0.4$ must be less than 1 GeV/c, as well as in the calorimeter where the summed E_T of calorimeter cells, excluding the expected muon deposition, must be ≤3 GeV. Details of the selection and the efficiencies are given in Table 5. Finally, the missing transverse energy in the events must be >15 GeV. After applying cuts to remove muons from π/K decays or cosmic rays, and validation of the muon quality on a high resolution graphics display, we are left with a sample of 67 W→ μν candidates: 10 events at √s=0.546 TeV and 57 events at √s = 0.630 TeV (Table 10).

In fig. 18 we compare the transverse momentum spectrum of the muons in these events with an ISAJET Monte-Carlo [27] simulation of W→ μν decays. The muon momentum resolution results in the disappearance of the Jacobian peak in the 2-body W decay, and gives rise to a long tail extending to large values of p_T^μ This is fully taken into account in the Monte-Carlo simulation and the expected and reconstructed p_T^μ spectra are in good agreement.

The main sources of background passing our W→ μν selection requirements are:

*   W→ τν decays with a subsequent τ→ μ$\nu\nu$ decay,
*   semi-leptonic decays of b and c-quarks,
*   muons from π or K decays.

The first two processes have been simulated using ISAJET [27]. Muons from tau-decay give a total of 3.1±0.5 events passing our selection criteria. This contribution is shown as the hatched area in fig. 18 and is included in the solid Monte-Carlo curve. π/K→ μ decays within a certain calculable range of decay angles are not identified by our software cuts or scan validation. We have evaluated the background from this source by using the decay simulation technique described in [47], and find a background of 0.4±0.2 events for the full sample. This background is neglected in the subsequent discussion. A summary of the W→ μν backgrounds is given in Table 9.

ii) $Z^0 \to \mu^+\mu^-$.

A dimuon hardware trigger, requiring at least two tracks in different muon detector modules, was active for most of the data-taking. These data were used in an initial rapid analysis. This trigger, however, was not explicitly required in making the final $Z \to \mu\mu$ selection because of its restricted acceptance. Instead, $Z \to \mu\mu$ event candidates are selected by demanding at least one muon track that satisfies the single muon trigger, with an associated track in the muon chamber pointing to the interaction vertex within 150 mrad (Table 6). After off-line reconstruction, a good quality track is required in the central detector with $p_T > 15$ GeV/c which must match the muon chamber hits. The second muon from the decay is identified by the requirement of a second track, which may have poorer quality. However, the energy deposition of this track must be consistent with that of a minimum ionising energy deposition in both the electromagnetic and hadronic calorimeters. A requirement that this track be seen in the muon chambers is applied if the central detector track points into the effective region of the muon chambers. Finally, a cut is made requiring a dimuon mass of $M_{\mu\mu} > 50$ GeV/c² in order to reject intermediate mass Drell-Yan events or rare $Z \to \tau\tau$ decays in which both τs subsequently decay into muons.

After muon quality validation of both tracks on a high resolution graphics display, a sample of 19 $Z \to \mu\mu$ candidates is obtained; 4 events at $\sqrt{s} = 0.546$ TeV and 15 events at $\sqrt{s} = 0.630$ TeV (Table 10). Two additional events, one at each energy, are selected by using looser cuts. One event fails the original track length requirement, the other fails the p_T cut by about 0.1 GeV/c. These two events do not satisfy the full selection requirements, and are not used to determine production cross-sections, but they are used in determining the Z mass. The sample contains two events with a detectable photon (photon transverse energies of $E_T = 10$ GeV and $E_T = 18$ GeV, at angles of 8° and 30°, respectively, to the nearest muon track); their 3-body invariant mass is consistent with the Z mass. We interpret these events as being due to hard photon bremsstrahlung processes [50,51].

Fig. 19 shows the invariant mass distribution of a dimuon sample including all the Z candidates described above. The $Z \to \mu^-\mu^+$ events are clearly separated from the lower mass $\mu^+\mu^-$ pairs coming from J/ψ, Υ and Drell-Yan production. The $Z^0 \to \mu^+\mu^-$ sample has a low background (Table 10).

4.3 Tau decay mode

The W→ $\tau\nu$ selection was part of the general missing transverse energy analysis [15,16]. The objective of this selection was to define an event sample for which the QCD jet background due to fluctuations in the detector response is small. Events contributing to this missing E_T sample are:

* leptonic W→ $\ell\nu$ decays,
* heavy quark decays, either from directly produced $Q\bar{Q}$ pairs or from W, Z→ $Q\bar{Q}$ decays with subsequent semileptonic decays Q→ q$\ell\nu$,
* Z→ $\tau\bar{\tau}$, and large p_T Z production followed by Z→ $\nu\bar{\nu}$, and finally
* two-jet events with large fluctuations in the measurement of the jet E_T.

Here Q indicates a heavy quark b, c or t, while q refers to a light quark u, d or s. Missing energy events are selected according to the criteria given in Table 7. This selection yields in total 56 events. The tau hypothesis is probed using a τ-likelihood function, L_τ, [16] combining 3 variables characterising the τ events:

* jet collimation expressed in terms of the fraction F of the jet energy measured within a cone of $\Delta R= 0.4$, relative to the total jet energy in a cone of $\Delta R=1.0$
* the angular separation (R) between the leading track as measured in the central detector and the jet axis measured from the calorimeters.
* the charged multiplicity (N_{ch}) of tracks with $p_T>1$ GeV/c within a cone of $\Delta R=0.4$ around the jet axis.

The expected distributions of the τ-likelihood function, L_τ, are displayed in fig. 20 for Monte Carlo samples of W→ $\tau\nu$ decays and of QCD dijets of similar E_T. The two distributions show a clear difference between τ-candidates and the broader QCD type jets. The final τ sample is defined as those events having $L_\tau>0$, which yields 32 events (Table 10). The missing E_T distribution of these events is shown in fig. 21. We do not expect a sharp Jacobian peak in the missing transverse E_T spectrum, because there are now two neutrinos in the process (a hard one from the primary W decay and a softer one from the τ decay). The background contribution from non -W→ $\tau\nu$ processes is 2.7 ± 0.6 events (Table 9). The signal is therefore 29.3±5.7 events, to be compared with 28.7±1.5 expected events, as calculated from theory taking into account the detection efficiency.

4.4 Search for W→ cs̄ and Z→cc̄, bb̄ decay modes

The colour degree of freedom ensures that the dominant decay modes of the W and Z are to quark-antiquark pairs; the exact ratio of the partial widths $\Gamma(q\bar{q})/\Gamma(tot)$ depends on the so far unknown mass of the top quark, but is above 2/3 for any top mass value. It is important to observe the decay of W/Z to quarks in order to confirm this aspect of the Standard Model. Despite their large branching fractions, the direct observation of W/Z decays to quark jets is difficult at present hadron collider experiments because of the large background of two-jet events from hard parton-parton scattering. The UA2 experiment has reported [52] an approximately three standard deviation signal in the W/Z mass region (65 to 105 GeV/c^2) in the invariant mass distribution of jet pairs. The signal to background ratio is approximately 1/20.

The dominant source of two-jet events at p_T=0.5·M_w is elastic scattering of gluons and light quarks, which is approximately two orders of magnitude more abundant than the expected W-decay signal. On the other hand, if one considers heavy quark (Q =b,c) channels, the cross-sections expected for c/b production by W/Z decay are comparable to those of the lowest order QCD processes for heavy quarks at the same p_T [53].

We have searched for the decays W→ cs̄, Z→ cc̄, bb̄ in which c/b jets are tagged by the presence of a high p_T muon in or close to the jet [54]. Recent UA1 studies indicate that once the contribution from π/K decays are subtracted, such muon-in-jet events are indeed predominantly due to semileptonic decays of c- and b-quarks [47,48]. These events are nearly free of gluon and light quark background, except for a small contribution in which the muons still come from π/K decays. The same studies have also confirmed QCD predictions that α_s^3 processes, such as gg→gg, with g→ cc̄, make a substantial contribution to strong cc̄ production [47]. Thus the signal to background ratio for W/Z decay jets is not expected to be as favourable as it appeared in [53], where only α_s^2 processes were considered. The study described here was made with events recorded with the inclusive muon trigger during the 1984 and 1985 runs. The work is based on a sample of 20000 events having a reconstructed muon with p_T^μ >6 GeV/c [47,48].

The decay of W/Z to a quark-antiquark pair should appear as a pair of jets. For intermediate bosons produced at low p_T the jets are coplanar with the beam axis. We require that one jet be accompanied by a muon, consistent with the semileptonic decay of a D or B meson. The final selection (Table 8) consists of events characterized by a muon accompanied by a small nearby jet and a large jet whose azimuth differs from that of the muon by over 90°. According to Monte-Carlo studies, a cut requiring a muon p_T of greater

than 8 GeV/c optimizes the ratio of signal to background. The total number of events satisfying these criteria is 1703. The total background from π/K decays is estimated to be $(37.9 \pm 1.5^{+8}_{-12})\%$, varying from nearly 80% at p_T^μ=6 GeV/c to less than 20% at p_T^μ >20 GeV/c. Details are given elsewhere [47,48].

From our measured values of $\sigma \cdot B(W \to e\nu)$ and $\sigma \cdot B(Z \to ee)$ and for $M_t \geq M_w$ (see Section 5), the Standard Model predicts 1070 events with $W \to c\bar{s}$ and 343 events with $Z \to c\bar{c}$ and $b\bar{b}$ for the integrated luminosity of 551 nb^{-1}. The ISAJET Monte Carlo program [27], followed by full detector simulation, has been used to calculate the effect of the selection criteria, and of the triggering and reconstruction efficiency. These numbers are reduced to 13.8 W and 23.5 Z events by requiring that the decay muon has p_T>8 GeV/c. A further reduction to 3.2 W and 5.6 Z events comes mainly from the triggering and reconstructing efficiency of the muon events (Table 8). The total expected signal amounts therefore to about 10 events.

Fig. 22 shows the effective invariant mass of the (jet-jet-μ-ν_T) system for the selected events, where ν_T indicates that we can only measure the transverse energy of the neutrino. We show, in addition, the corresponding Monte Carlo distributions of reconstructed $W \to c\bar{s}$, and $Z \to c\bar{c}$ and $b\bar{b}$ (note the logarithmic scale). The mass resolution is around 20%. The reconstructed W/Z masses are shifted downward from their input values by about 15% predominantly due to systematic underestimation of jet energies by the UA1 jet reconstruction algorithm [55]. From fig. 22 we conclude that the predicted signal from semileptonic heavy flavour W and Z decays alone contributes only a 2% effect in the respective mass interval.

It is therefore not possible to make any statements about the heavy flavour decays of the W and Z. The measured experimental distribution in fig. 22 can be explained entirely in terms of strong $c\bar{c}$ and $b\bar{b}$ production, and the π/K decay background. The histogram in fig. 23 represents the data after subtraction of the estimated π/K decay background, and the smooth curve is the ISAJET prediction for strong $c\bar{c}$ and $b\bar{b}$ production, normalized to the total number of events plotted. The absolute Monte Carlo prediction is only 9% higher than the experimental data, whereas the uncertainty in integrated luminosity alone gives a $\pm$15% error in the experimental cross-section. The agreement between ISAJET predictions and the data is not surprising, since the validity of these predictions for $c\bar{c}$ and $b\bar{b}$ production has been verified in studies of inclusive single muon and dimuon events in this experiment [45,46,47,48].

The ISAJET Monte Carlo program calculates c/b cross-sections for the lowest order

QCD processes and for the next higher order processes in which an initial- or final-state gluon evolves to $Q\overline{Q}$ ("flavour excitation" and "gluon splitting", respectively) [27]. In the region of the W/Z masses a cross-section is predicted which exceeds the lowest order cross-section (α_s^2) alone by a factor of five. It is evident then that higher order strong processes overwhelm the expected W/Z signal.

5. W, Z CROSS-SECTIONS and RELATED TESTS

5.1 Cross-sections

The cross-section times branching ratio for the inclusive W, Z production, $p\overline{p} \rightarrow$ W/Z + anything, followed by a W/Z leptonic decay, is obtained from the relation

$$\sigma \cdot B = (N_m - N_{bkg})/(\varepsilon \cdot L) \tag{5.1}$$

where N_m is the observed number of events, N_{bkg} the number of background events, L the integrated luminosity, and ε the overall efficiency (which includes effects of geometrical acceptance, trigger, selection, identification and reconstruction losses and kinematical cuts).

From the numbers quoted in Table 10 we derive the cross-sections at the two centre-of-mass energies. Our final results are given in Table 11, together with results from the UA2 collaboration [56] and theoretical expectations [28]. The first error quoted is statistical. The second error (systematics) is evaluated by adding in quadrature the ±15% uncertainty on the integrated luminosity of the experiment and the systematic uncertainty on the efficiency. The experimental errors are dominated by systematic uncertainties in the case of the W→ eν (15%), and by statistics in the case of Z → e$^+$e$^-$. We give results for a top mass of 44 GeV/c^2, which is the 95% C.L. lower limit from the UA1 analysis [48], and also for a top of M_t=80 GeV/c^2. The dependence on the top mass comes from whether or not a background top flavour contribution must be subtracted from the isolated electron/muon W samples. For $M_t \geq 44$ GeV/c^2, we expect a background contribution of less than 3% to the W samples, and a negligible contribution to the Z samples. With increasing top mass, the contribution decreases, and for a heavy top ($M_t \geq 80$ GeV/c^2) it no longer contributes significantly to our samples (≤ 0.6 events expected per leptonic mode).

Figs. 24a,b show the energy dependence of $\sigma \cdot B$ in the various IVB decay modes for the case of a massive top quark. Here, for simplicity, the theoretical expectations of refs. [28,33] have been rescaled to $M_t \geq 80$ GeV/c^2 to avoid any top mass dependence. Our final

cross-section values are consistent with the values of the UA2 collaboration [56] and with the theoretical predictions. We now discuss these predictions briefly.

In the framework of the QCD-improved Drell-Yan parton model for quark-antiquark annihilation, the W/Z production cross-sections have been calculated to all orders in QCD [28]. The higher orders increase the naive parton model prediction by about 30%. The theoretical predictions for $\sigma(W \to \ell\nu)$ and $\sigma(Z \to \ell\ell)$ are, however, affected by several uncertainties:

* an uncertainty of about ±30% due to various possible choices of structure functions, and of the Q^2 scale to be used for $\alpha_s(Q^2)$ in higher order terms [28];

* the uncertainty in the branching ratios $B(W \to \ell\nu)$ and $B(Z \to \ell\ell)$ due to the as yet unknown top quark mass. The variation amounts to ≤21% for $W \to \ell\nu$ and to ≤1.5% for $Z \to \ell\ell$, as M_t increases from M_t=40 GeV to M_W [41,92];

* a possible systematic increase of the expected W,Z production cross-sections by about 20% is suggested by the recent BCDMS data [41,57,92]. These data suggest that the u and d quark structure function parametrizations (GHR, DO1, DO2) used in [28] may underestimate quark densities at $|x| \approx 0.15$ by 10% [41].

We studied thus the sensitivity of our results to the top mass, and to the choice of structure functions (figs. 25a,b). The original theoretical predictions of ref. [28] on $\sigma_W B(W \to \ell\nu)$ and $\sigma_Z B(Z \to \ell\ell)$ for M_t=40 GeV/c^2 have been modified in figs. 25a,b, first to take into account the variation of the branching ratios as M_t increases from 40 to 80 GeV/c^2 (curve labelled 1), and second they have been rescaled upwards by 20% to account for the increase in the structure functions at $x \approx 0.15$ suggested by the most recent BCDMS data (curve labelled 2). The corresponding errors are indicated. The hatched band shows the measured UA1 cross-sections, including the effect of a possible top contribution.

In the ratios of cross-sections (Table 12) most contributions to experimental and theoretical uncertainties cancel. The systematic errors in the luminosities are also strongly correlated between the two CMS energies and therefore also tend to cancel. The ratio of the W,Z cross-sections is in good agreement with the UA2 results, and with theoretical expectations. The theoretical cross-section ratios are also more precise than the predicted cross-sections themselves because uncertainties due to structure functions and higher order QCD corrections largely cancel.

5.2 Test of the colour degree of freedom

Despite the uncertainties mentioned above in the theoretical W,Z production cross-sections, the agreement between data and theory (figs. 24, 25) is nonetheless a beautiful confirmation of the colour degree of freedom of quarks. Without colour the expected $W \to \ell\nu$ and $Z \to \ell\ell$ rates would be larger by a factor of about 6, in total disagreement with our data. Colour is responsible for a suppression factor of 3 in the total production cross-sections, and of a further suppression factor of ≈ 2 in the decay branching ratios. For example, for $W \to \ell\nu$

$$B(W \to \ell\nu) = \Gamma(W \to \ell\nu)/\Gamma(W \to \text{all}) \approx 1/(N_L + N_C \cdot N_Q) \qquad (5.2)$$

where $N_L = 3$ is the number of lepton doublets, $N_Q = 2$ or 3 is the number of quark doublets kinematically allowed in W decay (neglecting phase space suppression), and N_C is the number of colours. The suppression due to colour in the $Z \to \ell\ell$ branching ratio is also ≈ 2, although the expression for the branching ratio is more complicated.

Note that the test of colour is here significant, as the higher order QCD corrections to W and Z production (the "K-factor") amount to only about 30%, as compared to ~150% for Drell-Yan pair production at ISR energies. Consequently, the precision on the W cross-section measurements is sufficient to enable us to count the quark colours: at 90% confidence level we can exclude $N_C \leq 2$ colours (which would increase the predicted $\sigma \cdot B$ by a factor 1.9-2.0 depending on M_t), and also $N_C \geq 4$ colours (which would decrease the predicted $\sigma \cdot B$ by a factor 1.7).

5.3 Electron - muon - tau universality

The ratios of the $\sigma \cdot B$ partial production cross-sections for the various W and Z decay modes provide a test of lepton universality of the weak charged and neutral couplings at $Q^2 = M_{W,Z}^2$. Defining the weak charged coupling constants g_i, and the weak neutral coupling constants k_j, we have:

$$\sigma_w \cdot B(W \to \ell_1\nu_1)/\sigma_w \cdot B(W \to \ell_2\nu_2) = (g_1/g_2)^2 \qquad (5.3)$$

and

$$\sigma_z \cdot B(Z \to \ell_1\ell_1)/\sigma_z \cdot B(Z \to \ell_2\ell_2) = (k_1/k_2)^2. \qquad (5.4)$$

To increase statistics, we combine the samples at $\sqrt{s} = 0.546$ TeV and $\sqrt{s} = 0.630$ TeV. The cross-sections are weighted according to their corresponding luminosities in forming this

28

average. The systematic error due to the uncertainty in the measurement of the luminosity cancels in the ratio of cross-sections. The results are

$$g_\mu/g_e = 1.00 \pm 0.07 \pm 0.04$$
$$g_\tau/g_e = 1.01 \pm 0.10 \pm 0.06 \tag{5.5}$$
$$k_\mu/k_e = 1.02 \pm 0.15 \pm 0.04$$

where the first error is statistical and the second systematic. These results [17] confirm lepton universality at a better than 15% level, except for $Z \to \tau \tau$ for which the statistics are not yet sufficient. From the non-observation of $e\mu$ pairs with a mass consistent with the Z mass, we deduce that

$$B(Z \to e\mu)/B(Z \to ee) \leq 0.07 \qquad (90\% \text{ C.L.})$$

5.4 Cross-sections ratio $R = (\sigma_w \cdot B_w)/(\sigma_z \cdot B_z)$

The ratio of W to Z partial production cross-sections

$$R = \sigma(W \to \ell\nu)/\sigma(Z \to \ell^+ \ell^-) \equiv \sigma_w \cdot B(W \to \ell\nu)/\sigma_z \cdot B(Z \to \ell^+ \ell^-)$$
$$= R_\sigma \, (B_w/B_z) \tag{5.6}$$

is used in the determination of the number of light neutrino species N_ν [58,17,92]. To obtain the most precise value we combine the measurements for R in all decay modes and at both CMS energies in an overall fit. In doing this we assume lepton universality of the weak couplings, as tested in the previous section. The precision in the experimental determination of R is currently limited by the available Z statistics. The four UA1 results (assuming no top contribution), from the electron and muon channels of Table 10, give the result:

$$R = 9.1^{+1.7}_{-1.2} \tag{5.7}$$

where the error reflects mostly the limited Z statistics. In the case of a "light" top quark (M_t=44 GeV/c^2) this value of R should be decreased by 3% to account for the additional background in the W samples. The UA1 value of R is consistent with the corresponding result $R=7.2^{+1.7}_{-1.2}$ of UA2 [56]. A detailed analysis of R and its implications for the number of light neutrino families, N_ν, has been presented [17]. The combined measured values of R from the UA1 and UA2 experiments exclude $N_\nu \geq 5.7$ at 90% C.L. The present measurements of R do not put an upper limit on the top mass as discussed in ref. [92].

6. W,Z PRODUCTION PROPERTIES

The vector bosons W and Z are produced in lowest order by the Drell-Yan mechanism of quark-antiquark annihilation (fig. 1a). The longitudinal IVB momenta directly reflect the parton distributions as probed at the W/Z mass. A lowest order Drell-Yan production mechanism predicts no transverse momentum for the weak bosons, apart from small effects due to primordial partonic transverse momenta (<1 GeV). In QCD, however, a significant transverse momentum is expected to come from hard gluon bremsstrahlung from the annihilating quarks. Additional Feynman diagrams contributing to weak boson production are shown in figs. 1b,c,d. The diagrams fig. 1c and 1d correspond to the emission of a hard gluon and a hard quark, respectively. These processes dominate the cross-section at large p_T^{IVB} values. At high p_T^{IVB} the relative contribution of the Compton term (fig. 1d) amounts to 10-20% at our CMS energy.

The gluons (quarks), if radiated at large enough angle to the beam direction, may have sufficiently high transverse energy to give rise to detectable jets balancing the transverse momentum of the IVB. This QCD mechanism is expected to give rise to a long tail in the IVB transverse momentum distribution. The study of the IVB's transverse momentum distribution and the properties of the associated hadronic jets provide therefore a quantitative test of QCD [28,41].

6.1 Longitudinal W,Z and quark momentum distributions

The longitudinal momentum distribution of the IVB's is expected to reflect the structure functions of the incoming annihilating partons. The W fractional longitudinal momentum, $x_w \equiv 2p_L^W/\sqrt{s}$, is equal to the difference between the fractional momenta $(x_q, x_{\bar{q}})$ of the two annihilating partons. It can be determined by the sum of the longitudinal momenta p_L^ν and p_L^ℓ of the decay leptons. Thus the Feynman x of the W is:

$$x_w \equiv x_{\bar{q}}^- - x_q = \{p_L^\nu + p_L^\ell\}/(\sqrt{s}/2) \tag{6.1}$$

Although we do not measure the longitudinal momentum of the neutrino directly, it can be calculated by imposing the W mass on the lepton-neutrino system:

$$M_w^2 = (E_\ell + E_\nu)^2 - (\vec{p}_\ell + \vec{p}_\nu)^2.$$

The two solutions for the neutrino longitudinal momentum, p_L^ν, leave us with a two-

fold ambiguity on the W longitudinal momentum in about 50% of the events. In the remaining cases we have a unique value for x_w, as either one of the two solutions is unphysical ($|x_w|>1$), or both solutions give the same value of x_w. By considering the constraint of energy conservation in the overall interaction, we choose the p_L^ν solution with the minimal total energy imbalance in the event, including the energy flow measurement in the forward and very forward calorimeters [41]. This selection procedure to determine x_w has been tested and validated by Monte Carlo simulations.

For Z events on the other hand, both lepton momenta are measured, and there is no ambiguity in x_z. Because of the small number of Z events, data from both CMS energies and for both leptonic modes have been combined, after appropriate corrections for acceptance and resolution. The large momentum uncertainty of high momentum muons from Z decay can lead to significant overestimates of p_L^Z. We have therefore used only the $Z \rightarrow \mu^+\mu^-$ events, where the momentum balance constraint with fixed M_z can be imposed (section 7.2ii).

The distributions for $|x_w|$ and $|x_z|$ are shown in figs. 26a, b and c. From fig. 26a we see that the x_w distribution is not varying rapidly over our CMS energy range. The distributions after corrections for detector and selection biases, are in good agreement with the theoretical expectations using structure functions of Duke et al. [31] and Eichten et al. [30] with $\Lambda_{QCD}=0.2$ GeV. A detailed investigation [41] shows however that at our energy and with the present statistics we are not sensitive to differences among the various sets of structure functions.

Since the W^+ is produced by u-$\bar{d}$ fusion (and the W^- by $\bar{u}$-d), the x_w distribution is expected to be asymmetric, so far as the u and d momentum distributions differ. We therefore consider the quantity $Q \cdot x_w$ where Q is the sign of the W charge, and x_w is positive along the antiproton direction. Events with $Q \cdot x_w<0$ correspond then to W production where the fractional momentum of the u ($\bar{u}$) quark is larger than that of the d ($\bar{d}$) quark, and the converse is true for the $Q \cdot x_w>0$ region. The experimental $Q \cdot x_w$ distribution is shown in fig. 27a, background subtracted (bin by bin) and corrected for acceptance, resolution and biases arising from the x_w extraction procedure. We take into account only the 190 events with a well determined charge (error momentum $\cdot \Delta p$ less than p/2). The data do exhibit an asymmetry in agreement with expectations, indicating that the u quark distribution is indeed harder than that of the d quark, and this at $Q^2=M_w^2$. The expected distribution for EHQL1 structure functions is also shown (χ^2/d.o.f.=1.2).

To check the sensitivity to this property of the structure functions, we assumed identical structure functions for u and d quarks, and repeated the complete procedure of data

31

corrections as the acceptance corrections are different under these assumptions (see fig. 28). The resulting experimental and "expected" distributions are shown in fig. 27b, and the fit (χ^2/d.o.f.=3.3) is clearly poorer than in the previous case. The correction factors applied in the two cases (fig. 28) are obtained, as for all other corrected data, from the ratio of generated to reconstructed and selected W$\rightarrow$ eν Monte Carlo events. Notice that the shapes of the correction factors are asymmetric with respect to Q· x_w=0. This is due to the combination of three effects:

* the V-A coupling of the W producing asymmetric decays,
* the d ($\bar{d}$) quarks being softer than u ($\bar{u}$) quarks in the proton (antiproton), this implies an average boost of the produced W in the direction of the incident u ($\bar{u}$) quark,
* our track quality cuts eliminating preferentially events with $\theta_{lab}\approx$ 90° due to our magnetic dipole field.

From the energy conservation relation $x_q\cdot x_{\bar{q}} = M_{IVB}^2/s$ and from the known W charge we can now determine separately the x_u and x_d quark distributions contributing to W production. The shapes of the u and d quark fractional longitudinal momentum distributions, as sampled by W production, are shown in fig. 29. They are in agreement with QCD expectations, for example EHLQ1 as shown in fig. 29. With present statistics we are, however, not yet sensitive to the detailed variations in shape among the various parametrisations. The mean values are: $<x_u>$=0.17±0.01 and $<x_d>$=0.13±0.01.

6.2 The W, Z transverse momentum distributions

As already discussed, higher order QCD contributions (figs. 1b,c) lead to non-zero transverse momenta of the IVBs and to the associated emission of high transverse momentum hadrons.

The W transverse momentum p_T^W is obtained by adding the measured electron (muon) and neutrino transverse-momentum vectors. As explained in Section 2.4, the neutrino transverse momentum is experimentally determined by the global transverse energy balance in the calorimeters.

The W and Z transverse momentum distributions are shown in figs. 30a and b. There are 357 W$\rightarrow$ $\ell\nu$ events, with an estimated background of 30±5 events, and 51 Z$^0\rightarrow\ell^+\ell^-$ events with negligible background in these figures. The p_T^W distribution peaks at a value of

32

~4 GeV/c, which primarily reflects the experimental resolution on the missing transverse energy in W events. The shaded parts of the histograms in figs. 30 a,b correspond to W,Z events in which recognisable jets (of E_T>7 GeV) are produced. The expectation of associated jet production at large p_T^W is therefore clearly shown by the data. The overall shape of the measured W and Z transverse momentum distributions, after correction for acceptance, selection and resolution effects, is in good agreement with the QCD calculations of Altarelli et al. [28]. We now discuss this comparison in more detail.

Fig. 31 shows the differential cross-section $(1/N)(1/p_T^W)$ dN/dp_T^W as a function of p_T^W on a logarithmic scale. This emphasises the behaviour of W production at large transverse momenta, where the perturbative QCD regime is expected to prevail. The distribution has been corrected for detection and selection inefficiencies and for effects of detector resolution. The correction factors for each bin, taking into account all effects, have been determined to a precision of 10-15%. The resolution on p_T^W is ~ 15% for large values of p_T^W, and the systematic error on the absolute energy scale is about 9%.

In fig. 31 the experimental data are compared with theoretical predictions. The solid curve (up to 25 GeV/c) has been calculated using a soft gluon summation technique [28], with DO1 structure functions, and $\alpha_s=\alpha_s(M_w^2)$. The theoretical uncertainties [28] and the experimental correction techniques used in the intermediate to low p_T^W region are discussed in more detail below and in ref. [41]. The shaded band in the high p_T region results from a perturbative QCD calculation to order α_s, normalized by the lowest order W cross-section [28]. The theoretical uncertainty indicated by the width of the band is the result of the combined uncertainties from the choice of the Q^2-scale used for α_s and the choice of the parton distribution functions. Above 60 GeV/c this calculation has been extrapolated using a tuned version of the ISAJET Monte Carlo program. A detailed discussion of the high p_T^W region can be found in ref. [14].

For p_T^W <25 GeV, it is more difficult to correct experimentally [41] and more sophisticated soft gluon resummation QCD techniques are needed to calculate the p_T^W distribution [28]. In fig. 32 we show the data, after bin by bin background subtraction, compared with QCD calculations of Altarelli et al. [28], which have been modified to take into account our experimental selection and reconstruction biases [41]. These calculations provide a good description of the data in this p_T range. The sensitivity of these QCD calculations to Λ_{QCD} is illustrated by the two theoretical predictions shown in fig. 32. The different choice of Λ_{QCD} and of structure functions [28], significantly affects the shape of the p_T^W distribution for p_T^W <15 GeV/c, while above ~25 GeV/c it affects only the magnitude of the cross-section, as

is visible from figs. 31 and 32. The data in fig. 32 slightly favour the choice Λ_{QCD}=0.2 GeV.

A QCD calculation [59] shows that the average transverse momentum of lepton pairs produced in Drell-Yan processes increases with $\sqrt{s}$ according to:

$$<p_T^2> = \alpha_s(Log\ Q^2) \cdot s \cdot f(\tau, Log\ Q^2) + c \qquad (6.2)$$

where $\tau = M^2/s = x_1 x_2$ and f is a function of τ and $Log\ Q^2$. This relation indicates that $<p_T>$ grows like $\sqrt{s}$ at fixed τ, in so far as the Q^2 dependence of α_s and f is small (logarithmic). In fig. 33 the $\sqrt{s}$ dependence of the average transverse momentum of lepton pairs produced in Drell-Yan processes is shown. In the region $\sqrt{s} \leq 62$ GeV, the data on muon pairs [60,61] are at $\sqrt{\tau} \approx 0.22$, while $<p_T^W>$ and $<p_T^Z>$ from UA1 and UA2 at $\sqrt{s} = 0.546$ and 0.630 TeV correspond to $\sqrt{\tau} \approx 0.15$. The electron and muon data from the UA1 Z^0 samples have been combined. The expected linear relation between $<p_T>$ and $\sqrt{s}$ is well born out by the data, but does not hold over the entire $\sqrt{s}$-range. Below ISR energies the effects of scaling violations and of sub-asymptotic contributions from soft gluons distort the expected linear rise significantly. Nonetheless, at higher $\sqrt{s}$ the data are consistent with QCD predictions.

We compare in fig. 34 the inclusive transverse momentum cross sections for jets, single photons, low-mass Drell-Yan $\mu^+\mu^-$ pairs and W production as measured by UA1. In this figure the low-mass ($M_{\mu\mu}$<2.5 GeV) high-$p_T^{\mu\mu}$ production spectrum has been appropriately scaled for comparison to direct photons, to account for the mass of the off-shell virtual photon, as discussed in ref. [65].

There is an overall systematic uncertainty of about ±23% for the direct photon cross-sections [62,63] and of about ±70% for jet cross-sections [64]. The solid lines are the QCD predictions from Aurenche et al. for direct photons [65], from Stirling et al. [66] for jet cross-sections and of Altarelli et al. [28] for W/Z production. At large enough transverse momenta, $p_T^{W,\gamma}$ larger than about 50 GeV, where the effects of finite W,Z mass are reduced relative to photon production, the W and γ absolute production cross-sections become comparable. This is a direct manifestation of electroweak unification, the ratio of W and γ couplings to quarks being $sin\theta_w$.

6.3 Jet properties in W, Z events

As previously noted, QCD contributions to IVB production lead to final states in which one or more gluon or quark jets are produced in association with the IVB at a rate depending on the value of α_s. The leptonic decays of the IVBs offer the simplest case in which only initial-state QCD bremsstrahlung contributes.

Experimentally, jets are defined by the standard UA1 jet algorithm [26]. The jet search is restricted to the rapidity range $|\eta| \leq 2.5$ with an initiator of 1.5 GeV. To identify jets with transverse energies as low as $E_T = 7$ GeV, jet validation by charged tracks is necessary. This validation requires association of the calorimetric jet to a charged track of at least $p_T \geq 0.5$ GeV/c in a cone of $\Delta R \leq 0.4$ around the axis of the jet. Using the ISAJET Monte Carlo with full apparatus simulation, the efficiency of this validation has been estimated at $74 \pm 3\%$.

In fig. 30 the 116 W and 19 Z events containing a jet with $E_T > 7$ Gev are indicated by the shaded area. The data at $\sqrt{s} = 0.546$ TeV and 0.630 TeV have been combined. As already noted, the presence of jets is strongly correlated with high transverse momenta of the IVBs, almost all events with $p_T^W \geq 10$ GeV/c being accompanied by detectable jets.

Fig. 35 shows the corrected jet multiplicity distribution. 37% of the W and 43% of the Z events have at least one jet with $E_T \geq 7$ GeV/c. The jet multiplicity distribution is well described by QCD expectations as given by the ISAJET Monte Carlo. With the E_T cuts and the two jet resolution achieved in the UA1 detector, the observation of a second jet is effectively independent of the first one [67].

Standard UA1 jet corrections have been applied to jet energies and momenta defined by the algorithm. As the jets essentially balance the IVB in the transverse plane, their E_T spectrum shown in fig. 36 reflects the p_T^W spectrum.

At our $p\bar{p}$ collision energy, jets largely come from initial-state bremsstrahlung. For gluonic jets (diagrams in fig. 1c) the angular distribution is expected to follow a bremsstrahlung type distribution $\sim 1/(1 - \cos\theta_j^*)$. The angle θ_j^* is measured with respect to the average incoming parton direction in the W-jet centre-of-mass system. The angular distribution is expected to be peaked in the beam direction. Experimentally we measure the angle of emission with respect to the beamline, as the radiating parton cannot be identified. Therefore we present results in terms of the modulus $|\cos\theta_j^*|$. The measured spectrum is indeed well described by a $1/(1 - |\cos\theta_j^*|)$ distribution (fig. 37). The W sample is here limited to single jet events for which the detector acceptance is reasonably uniform (ie.

$|\cos\theta_j^*|\leq 0.95$), and for which all angles in this range are kinematically allowed (ie. $M(W+jet)\geq 100$ GeV/c^2). The analysis is limited to the $W\rightarrow e\nu$ events, as the uncertainty on the longitudinal momentum of $W\rightarrow\mu\nu$ decays is too large.

6.4 Test of the gluon spin in W+jet events

A method to test the spin of the gluon in high p_T W (or Z) production with gluon bremsstrahlung (fig. 1c) has been suggested [68,69], making use of the axial-vector coupling of the intermediate vector bosons to the quarks. Since the axial part of the current is not generally conserved, the polarization of the W produced in association with a single gluon is sensitive to the gluon spin. A vector gluon radiated by an incoming quark (or antiquark) preserves the helicity of the quark whereas a scalar gluon flips the helicity and leads to a different polarization of the W.

The polarization state of the W can be measured through the angular distribution of the decay leptons. The summed angular distribution of the electron and neutrino is in general [69,41]:

$$dN(e+\nu)/d|\cos\theta^*| = 2 \cdot \{3/8\}\cdot\{1+ A_o/2\} \cdot\{1 + \cos^2\theta^* \cdot(2-3A_o)/(2 + A_o)\}$$
$$dN(e+\nu)/d\varphi^* = 2 \cdot \{1/2\pi\} \cdot \{1 + \cos^2\varphi^* \cdot A_2/4\} \qquad (6.3)$$

where φ^* is the azimuthal angle and θ^* the polar angle of the electron or neutrino, expressed in a W rest frame. A_o and A_2 are combinations of W helicity amplitudes, which in general are functions of the p_T of the W [68]. In the Gottfried-Jackson W rest frame (fig. 38) $A_0-A_2=0$ for a vector gluon and $A_0-A_2=2$ for a scalar gluon [68]. In our intermediate p_T^W region $10\leq p_T^W \leq 30$ GeV/c this then leads to very different $\cos\theta$ distributions in the two cases [68]:

$$dN/d|\cos\theta^*| \sim (1 + \cos^2\theta^*) \quad \text{for a vector gluon} \qquad (6.4)$$
$$\sim (1 - \cos^2\theta^*) \quad \text{for a scalar gluon}$$

Thus for a vector gluon the decay leptons are preferentially emitted along the beam direction, as expected also for the low p_T^W Drell-Yan process, whereas for a scalar gluon the decay electrons have a more central angular distribution.

The gluon spin analysis was performed for the $W\rightarrow e\nu$ sample. We used the

transverse momentum of the W's as a measure for the hard gluon emission process. A cut $p_T^W > 7$ GeV/c leaves us with a sample of 121 W's, of which nearly all have observable jets reconstructed by the UA1 jet algorithm. Since we are interested in W events with single gluon emission, we retain only events with no other recognizable jet exceeding 5 GeV (111 events). Although this cut is not sufficient to exclude multigluon emission processes with low E_T gluons, it is not critical for two reasons: i) in the case of scalar gluons, multigluon emission should be strongly suppressed anyhow [70], and ii) in the case of vector gluons, multigluon emission does not change the W polarization state as already mentioned.

The background contribution to this data sample with $p_T^W \geq 7$ GeV/c is negligible [41]. The experimental decay angular distributions are corrected for acceptance, effects of detector resolution as well as of the ambiguity on p_L^ν. From Monte-Carlo simulations we derived two sets of correction factors: one for the vector gluon hypothesis and one for the scalar gluon hypothesis.

The experimental $\cos\theta^*$ distributions, with the fitted functions 6.4 (solid lines), are shown in fig. 39. The data are separately corrected for the two different gluon spin hypotheses. We obtain $A_0 = -0.19 \pm 0.32$ (fig. 39a) for the vector gluon hypothesis (χ^2/d.o.f. = 0.75), and $A_0 = 0.70 \pm 0.35$ (fig.39b) for the scalar gluon hypothesis (χ^2/d.o.f.= 3.75). The dashed lines in fig. 39 show the expected distributions for vector and scalar gluon cases (6.4) respectively. The experimental φ^* distribution is flat in each case. A fit of the parameter A_2 to this distribution gives $A_2 = 0.08 \pm 0.60$.

From these numbers we derive:

* for the vector gluon hypothesis
  $A_0 - A_2 = -0.27 \pm 0.68$ (expected = 0.0)
* for the scalar gluon hypothesis
  $A_0 - A_2 = +0.62 \pm 0.69$ (expected = 2.0)

Hence a scalar gluon is excluded at a 2σ level from the measurement of A_0-A_2, independently of p_T^W. However, since our W's are in a limited region $7\,\mathrm{GeV/c} \leq p_T^W \leq 30$ GeV/c, where A_0 is not expected to vary much ($-1. \leq A_0 \leq -0.8$ [68] for the scalar gluon), the measurement of A_0 alone excludes the scalar gluon hypothesis at a 4σ level.

This measurement thus provides, in addition to the gluon spin determination from three-jet events in e^+e^- annihilations at PETRA [71] and from the two-jet event angular

distribution in UA1 [72], an additional independent confirmation of the internal consistency of QCD through the spin 1 assignment for the gluon [73].

6.5   The underlying event in W production

In this section we describe the characteristics of the rest of the event that accompanies IVB production, and compare them with minimum bias events [74]. The underlying event in W production is obtained by excluding the leptonic W-decay products. The underlying event therefore includes fragments of the beam (spectator partons) and of any radiated hard partons (recoil jets) [75].

The calorimeter responds to both charged and neutral particles. The average response of the calorimeter to low energy debris in minimum-bias events depends, however, on the $\pi/K/p$ particle composition, and on the transverse momentum distributions of both charged and neutral particles in the event. This results in a model dependent correction factor in the reconstruction of the total energy. This is well understood for charged particles, which are studied with the central detector, but is less certain for neutral particles. To reduce this uncertainty, we have limited our study to the properties of charged particles measured in the UA1 central detector (CD).

We use a sample of 147000 minimum bias events at $\sqrt{s}=0.63$ TeV. In the data used here we limit ourselves to tracks with $|\eta|<2.5$ and $p_T>0.15$ GeV/c. Each track has been weighted by an acceptance factor, which depends upon its charge, p_T, η and azimuthal angle. Acceptance losses have been estimated by assuming flat distributions in pseudorapidity and in the azimuthal angle around the beam axis. The IVB sample used for this study consists of the W events which decay to electrons described above, corrected for the acceptance in p_T^W (fig. 15).

The inclusive invariant transverse momentum spectra for charged tracks are shown in fig. 40. The distributions have been corrected for random measurement errors and for systematic effects. The p_T distribution is harder for the underlying event in W production than for the minimum-bias sample, due to W production at large p_T.

This global behaviour can be studied in more detail as a function of p_T^W. We look at the following quantities:

* $<p_T>$, the mean transverse momentum of charged tracks above 0.15 GeV/c;

* $(\Sigma\, p_T)$, the scalar sum of transverse momenta of all charged tracks with $p_T > 0.15$ GeV/c; this is a measure of the mean total transverse energy in the event;
* $<N_{ch}>$, the mean number of charged tracks with $p_T \geq 0.15$ GeV/c.

In fig. 41 we show these quantities as a function of p_T^W, for $W \rightarrow e\nu$ events, and compare them to the values observed in minimum-bias events. The resultant mean values are summarized in Table 13. In the underlying event the average charge multiplicity, transverse momentum and total transverse energy increase with increasing p_T^W. These quantities have a larger average value than in minimum bias data. From fig. 41 we conclude that the activity in the rest of a W event when $p_T^W \rightarrow 0$ is similar to that seen in minimum bias events.

7. W, Z⁰ MASSES AND DECAY PROPERTIES

7.1 W masses and widths

For the W, the invariant mass of the $\ell\nu$-system cannot be reconstructed directly from the 2-body decay products, since the longitudinal component of the neutrino momentum is not measured. The distribution of the transverse mass, $M_T^{\ell\nu}$, is used instead to evaluate the W mass. The transverse mass is defined as :

$$M_T^{\ell\nu} = [2 \cdot p_T^{\ell} \cdot p_T^{\nu} \cdot (1 - \cos \Delta\phi)]^{1/2} \qquad (7.1)$$

where p_T^{ℓ} and p_T^{ν} are the charged lepton $\{e, \mu, \tau\}$ and neutrino transverse momenta, and $\Delta\phi$ is the relative azimuthal angle between the leptons. This variable is chosen, rather than p_T^{ℓ} or p_T^{ν}, as it renders the analysis less sensitive to the W transverse momentum and associated QCD corrections. The exact shape of the M_T distribution depends on M_W, Γ_W, the W spin state, the longitudinal and transverse components of the W momentum at production, the experimental W selection biases and the transverse energy resolution of the lepton and neutrino [41,42,44]. A Monte Carlo simulation of W production, including all known acceptance, selection, and resolution effects and appropriate background contributions is used to generate M_T distributions. These are fitted to the data to determine the parameters M_W and Γ_W [42,43,44].

i) W→ eν channel

In the electron case, we replace the momenta in (7.1) by the directly measured quantities E_T^e and E_T^ν. The experimental M_T distribution of the total W→ eν sample is shown in fig. 42, together with the background contributions from W→ τν and from QCD two-jet events. To reduce the background, which is concentrated at low electron and neutrino E_T, we select a sample with $E_T^e > 30$ GeV and $E_T^\nu > 30$ GeV (fig. 43). Sets of Monte Carlo events have been generated with different W mass values and with a fixed W width (2.8 GeV/c^2), close to the expected value. The result of a maximum likelihood fit on the 149 W→ eν events gives (Table 14):

$$M_{W\to e\nu} = 82.7 \pm 1.0 \pm 2.7 \text{ GeV/c}^2 \qquad (7.2)$$

We again quote first the statistical error and second the systematic error. This value is in good agreement with results from our previous papers [13] and the result of the UA2 collaboration [77]. The systematic error is due to the uncertainty in the electron energy (Table 2) and to a further 2% uncertainty in the neutrino energy. The latter is obtained from event simulation, and contains the uncertainty due to simulation, estimated by performing the same maximum likelihood fit to a Monte Carlo W event sample [42].

To get a limit on the W total width, additional sets of Monte Carlo events have been generated with different values of the width at the fitted W mass. Fitting the experimental distribution M_T, the most probable value given by the fit is:

$$\Gamma_{W\to e\nu} = 2.8^{+1.4}_{-1.5} \pm 1.3 \text{ GeV/c}^2 \qquad (7.3)$$

The 90% C.L. limit is $\Gamma_W \le 5.4$ GeV/c^2 (Table 14).

ii) W→ μν channel

To measure the W→ μν mass, we limit ourselves to a subsample of 46 W→ μν events, which have a well measured momentum in the central detector. For each event an overall momentum fit has been performed, combining the information from the CD track, the hits in the limited streamer chambers and the hits in the muon chambers, and allowing for multiple scattering in the calorimeter and iron absorber wall [43]. We have used this momentum measurement to redetermine the parameters of each event. For W mass

determination we have performed a fit to the inverse transverse mass distribution $1/M_T$ (fig. 44). We choose the $1/M_T$ rather than the M_T distribution because $1/p$ is proportional to the sagitta of the muon track. The measurement uncertainty of this quantity has a gaussian distribution which simplifies error handling. The maximum likelihood fit to the data is insensitive to the W width, because of poor momentum resolution. Thus we used as an additional input parameter a value of Γ_W equal to 2.8 GeV/c^2.

The background contribution from $W \to \tau \nu$ with $\tau \to \mu \nu \nu$ is taken into account. We have performed the same fit on a Monte-Carlo sample of $W \to \mu \nu$ decays, which were fully simulated in the detector. The background contribution includes the appropriate fraction of simulated $W \to \tau \nu$ decays mixed in with the Monte-Carlo $W \to \mu \nu$ events. We take into account the systematic effects revealed by the mass fitting of the Monte Carlo events [43]. In our final estimate the total systematic uncertainty contains the errors coming from this procedure, the uncertainty in the W production properties and the limitations of the simulation of the detector. From this we obtain:

$$M_{W \to \mu \nu} = 81.8\ ^{+6.0}_{-5.3} \pm 2.6\ \text{GeV/c}^2 \qquad (7.4)$$

which is in good agreement with the electron channel result.

iii) $W \to \tau \nu$ channel

The 32 $W \to \tau \nu$ candidates selected are characterised by a pencil-like jet and significant missing energy [15,16]. All events except one have a single narrow jet with $E_T > 12$ GeV. M_T is evaluated from (7.1) using E_T^{mis} and $E_T(\text{jet})$ for p_T^{ν} and p_T^{ℓ} respectively. Fig. 45 shows the M_T distribution for these events, together with the expected distribution for a W mass of 82.7 GeV/c^2. A fit to this distribution gives

$$M_{W \to \tau \nu} = 89 \pm 3 \pm 6\ \text{GeV/c}^2 \qquad (7.5)$$

The systematic error is due to the uncertainty in the absolute hadronic energy scale.

7.2 Z^0 masses and widths

To determine the Z mass we have made a maximum likelihood fit of a Breit-Wigner

shape smeared by the experimental resolution to the experimental dilepton mass distribution.

i) $Z^0 \rightarrow e^+e^-$

Out of the total sample, only 24 events have been used for the mass fit (fig. 46). In each event the electromagnetic clusters and the associated central detector tracks are well measured and $M(e^+e^-) > 70$ GeV/c^2. The background is negligible. As in the case of the W, sets of Monte Carlo events have been generated at different mass values and with a fixed width of 2.8 GeV/c^2 [42]. In the case of the Z, however, the result of the mass fit does not depend strongly on the resolution of the calorimeter introduced in the simulation. The results of the fit to M_Z and Γ_Z (Table 14) are:

$$M_{Z \rightarrow e^+e^-} = 93.1 \pm 1.0 \pm 3.1 \text{ GeV}/c^2. \tag{7.6}$$

The systematic error is again due to the uncertainty in the energy measurement for electrons (Table 2). For comparison, sets of Monte Carlo events were also generated with different widths and with the central mass fixed at the fitted mass. The best estimate of the Z width from the fit is $\Gamma_Z = 2.7 \, ^{+1.2}_{-1.0} \pm 1.3$ GeV/c^2. The upper limit at 90% C.L. on Γ_Z is 5.2 GeV/c^2 (Table 14).

ii) $Z^0 \rightarrow \mu^+\mu^-$

To measure the Z mass from $\mu^+\mu^-$ decays, we start from the sample of 21 events described in Section 3.2. We limit the sample to well measured events by removing: i) the two radiative Z decay candidates, since the mechanism of the decay introduces different systematic errors, and ii) another event whose relatively low dimuon mass (<60 GeV/c^2) suggests that it may have been systematically mismeasured. For the remaining 18 events an overall momentum fit has been performed on each track and the event parameters have been re-determined [43,44]. This gives the dimuon mass distribution in fig. 47a, to which a maximum likelihood fit of a Breit-Wigner shape smeared by the muon momentum resolution is applied. As our data are insensitive to the Z width, we have chosen the value $\Gamma_Z = 2.8$ GeV/c^2. Using this method, the result of the fit (Table 14) is:

$$M_{Z \rightarrow \mu\mu} = 94.1 \, ^{+8.4}_{-6.6} \pm 2.8 \text{ GeV}/c^2 \tag{7.7}$$

where the systematic error reflects the uncertainty of the Monte-Carlo simulation for the CD.

The Z→ μμ mass determination is improved using the method of transverse momentum balance [15]. In this method it is assumed that each event has no real missing transverse energy. The muon momenta are then estimated performing a chi-squared minimisation taking into account the measured momenta and the calorimetric energy flow. In addition a constraint is applied that the sum of all three-vectors should be zero in the transverse plane. It is not however possible to use this method if high momentum particles are lost through cracks in the calorimeter as the energy flow measurement is then unreliable (5 events). We are therefore left with 14 events [43,44]. For these we refit the muon pair momenta to determine M_Z. Correlations between the two muon tracks result in a small bias towards low mass values, for which we have attempted to correct by using event-by-event Monte-Carlo corrections to the resulting masses. These corrections were not applied in our previous paper [5].

The resulting mass peak is narrower than the unbalanced one (fig. 47a) and is shown in fig. 47b, with the fitted mass distribution superimposed. We obtain the improved value:

$$M_{Z→μμ} = 90.7 \, ^{+5.2}_{-4.8} \pm 3.2 \text{ GeV/c}^2. \tag{7.8}$$

The new result has better statistical precision than the unbalanced one (7.7), but the systematic error is slightly larger as a result of the uncertainty in the correlation corrections. It is in good agreement with our electron result (7.6) and the UA2 result of $91.5\pm1.2\pm1.7$ GeV/c^2 [77].

7.3 W,Z Decay angular distributions at low p_T^{IVB}

i) $W^{\pm}$ decay

For W's produced in Drell-Yan valence quark annihilation processes we expect the angular distribution of the decay leptons to exhibit a pronounced charge and angular asymmetry due to the pure V-A coupling of the charged currents. At low p_T the W's are produced fully polarized along the beam direction. At the CERN collider energies the production from sea-sea quark annihilation can be neglected and the decay angular distribution in the CMS of the W is simply:

$$dN/d(\cos\theta^*) = (1+\cos\theta^*)^2. \tag{7.9}$$

(θ^* is the angle between the electron and the proton direction, or the positron and the antiproton direction in the W rest frame).

The W decay angular distribution, for p_T^W <15 GeV/c, is shown in fig. 48 as a function of $Q \cdot \cos\theta^*$, where Q is the W charge. The distribution is corrected for background, acceptance, resolution and the bias introduced in choosing p_L^ν, which is necessary for defining the Lorentz transformation between the laboratory and W rest frame [41]. Only those events with a well determined lepton charge (error momentum $\cdot \Delta p$ less than p/2), are considered. There is agreement with the $(1+\cos\theta^*)^2$ behaviour expected for pure V-A coupling. The slight excess of events near -1 is compatible with a small sea-sea contribution, which is expected to be about 2-4% at our CMS energy (depending on the choice of the structure functions) and is indicated by the shaded band in fig. 48 [41].

The mean value of the decay angular distribution is directly correlated with the spin J of the W [78]:

$$\langle Q \cdot \cos\theta^* \rangle = (\langle\lambda\rangle\langle\mu\rangle)/(J(J+1)) \qquad \text{for } J>0 \qquad (7.10)$$
$$= 0 \qquad \text{for } J=0$$

where μ and λ are the global helicities of the production system (u, d) and the decay system (eν), respectively. The measured value of $\langle Q \cdot \cos\theta^* \rangle$ is 0.43±0.07. A value of 0.5 is expected for a W of spin 1 where initial and final fermion states are fully polarised ($\langle\lambda\rangle=\langle\mu\rangle=\pm1$) and there is no sea-sea contribution. A value of 0.46±0.02 is expected taking into account a sea-sea contribution as indicated in fig. 48.

An additional uncertainty in the value of $\langle Q \cdot \cos\theta^* \rangle$ arises when the W's are produced with non-zero transverse momentum (assuming vector gluons of course), which perturbs the W alignment with the beam axis. In the region of small p_T^W ($\leq$15 GeV/c), where most of the events are found, the production mechanism is not precisely known, due to the unreliability of first order QCD calculations in this kinematic region. Depending on the way the small, but finite transverse momentum of the W is generated (incoherent soft gluon emission, or first order perturbation process), we estimate by a Monte Carlo procedure that the expected range of variation $\langle Q \cdot \cos\theta^* \rangle$ is from 0.42 to 0.48 [43].

We can also define an asymmetry parameter:

$$A_W = (N^+-N^-)/(N^++N^-) \qquad (7.11)$$

where $N^{+(-)}$ is the number of events in the positive (negative) half of the $\cos\theta^*$ plot. We obtain $A_W = 0.77 \pm 0.04$, in agreement with the predicted value of 0.75 for pure V-A coupling, and 0.71 ± 0.02 including the small sea-sea contribution.

ii) Z^0 decay

Because the Z coupling to charged leptons is almost purely axial vector, the expected decay angular asymmetry is small. The angular distribution can be parametrized as

$$dN/d\cos\theta^* \sim (1+2\cdot k\cdot\cos\theta^* + \cos^2\theta^*), \qquad (7.12)$$

where k depends on the vector and axial-vector parts of the couplings of the fermions to the Z, and is thus sensitive to $\sin^2\theta_w$. The distribution should be completely symmetric (k=0) in the case that $\sin^2\theta_w = 0.25$ (pure axial vector coupling). The measured angular distribution for $Z \rightarrow \ell^+ \ell^-$, corrected for acceptance and resolution effects, is shown in fig. 49 [44]. The events used are taken from the sample used for the $|x_z|$ distribution with the additional requirement that the charges of the two leptons are well determined. This leaves 21 $Z \rightarrow ee$ and 12 $Z \rightarrow \mu\mu$ events. We obtain $k = 0.06 \pm 0.24$. Using the EHQL1 parametrisations for the u and d quark structure functions, the measurement of k, which is related to $\sin^2\theta_w$ as shown in fig. 50, yields a value $\sin^2\theta_w$ of $0.24 \, ^{+0.05}_{-0.04}$.

Notice that the Z decay angular distribution provides a determination of $\sin^2\theta_w$ which is totally independent of the W and Z masses, in contrast to the result obtained in the next section. At present this method based on the Z decay angular distribution is limited by statistics, but ultimately it will be limited only by the knowledge of the relative $u\bar{u}$ and $d\bar{d}$ contributions to Z production (structure functions).

8. STANDARD MODEL PARAMETERS

The deep inelastic neutrino scattering experiments allowed prediction of the W and Z masses, through the measurement of the Standard Model parameters . The subsequently measured collider values are in remarkable agreement with this prediction. In return, the measured W and Z masses determine directly the parameters of the Standard Model.

45

According to the Sirlin renormalization scheme [80] extended to a non-minimal electroweak theory, the W and Z masses are related to the Standard Model parameters in the following way:

$$\sin^2\theta_w = 1 - \{M_w^2/(\rho M_z^2)\} \tag{8.1}$$

In the electroweak theory θ_w is the angle used to define the mixing of neutral fields and ρ is the weight of neutral currents in the effective Hamiltonian. In the minimal scheme, where there is a single Higgs doublet, $\rho=1$.

Taking into account radiative corrections Δr, the basic expression of $\sin^2\theta_w$ as a function of M_w^2 is:

$$\sin^2\theta_w = (A^2/M_w^2)(1/1-\Delta r) \text{ defined here as } \sin^2\tilde{\theta}_w \tag{8.2}$$

$$\text{with } A = \sqrt{\pi\alpha/\sqrt{2}G_F} = (37.2810 \pm 0.0003) \text{ GeV/c}^2$$

α and G_F are the values of the electromagnetic and the weak (or Fermi) coupling constants [79]. G_F is determined by the measurement of the muon lifetime. The radiative correction factor $(1-\Delta r)^{-1}$ corresponds to the evolution of α^2 from low energy up to M_w^2.

The mixing parameter $\sin^2\theta_w$ can be determined in two ways by hadron collider experiments:

i) From the measured W and Z masses, using expression (8.1) and assuming $\rho=1$, one obtains $\sin^2\hat{\theta}_w$,

ii) From the measured W mass and the calculated radiative correction Δr, using expression (8.2) one obtains $\sin^2\tilde{\theta}_w$, without assumption on ρ.

The radiative correction depends slightly on unknown particle masses, top (M_t) and Higgs (M_H). Assumming $M_t=45$ GeV/c^2 and $M_H=100$ GeV/c^2, one gets $\Delta r=0.072 \pm 0.002$ [82].

From our measurements of the W and Z masses in the electron channel, and this value of Δr one gets:

$$\sin^2\widehat{\theta}_w = 0.211 \pm 0.025 \tag{8.3}$$

$$\sin^2\widetilde{\theta}_w = 0.219 \pm 0.005 \pm 0.014. \tag{8.4}$$

With the present statistics and precision of the UA1 experiment, $\sin^2\widetilde{\theta}_w$ is clearly limited by the systematic error of the $W^{\pm}$ mass, whereas for $\sin^2\widehat{\theta}_w$, the systematic errors largely cancel in the mass ratio, and statistics is at present the limiting factor. Both values of $\sin^2\theta_w$ agree well with the world average value determined from lepton-nucleon scattering experiments at the M_w scale [83, 84]:

$$\sin^2\theta_w = 0.233 \pm 0.003 \pm 0.005 \tag{8.5}$$

With the W and Z masses it is possible to test the minimal hypothesis for the ρ parameter. Using our measured value $\sin^2\widetilde{\theta}_w$ in (8,1) one obtains :

$$\rho = M_w^2/(M_z^2 \cdot \cos^2\widetilde{\theta}_w) = 1.010 \pm 0.028 \pm 0.020 \tag{8.6}$$

This value agrees with the expectation $\rho=1$ of the minimal hypothesis.

The radiative correction Δr can be estimated from expression (8.2), with two determination of $\sin^2\theta_w$, giving a further test of the consistency of the results.

1) From $\sin^2\widehat{\theta}_w$ (assuming $\rho=1$) and the W mass one obtains Δr_1 :

$$\Delta r_1 = 1-A^2/(M_w^2 \sin^2\widehat{\theta}_w) = 0.037 \pm 0.100 \pm 0.067. \tag{8.7}$$

2) From the measurement of $\sin^2\theta_w$ in νN scattering and the W mass one obtains Δr_2 (without assumption on ρ) :

$$\Delta r_2 = 1-A^2/(M_w^2 \sin^2\theta_w) = 0.128 \pm 0.023 \pm 0.060. \tag{8.8}$$

Using (8,2) and (8,1) with the assumption $\rho=1$, a joint fit of M_w, M_z and $\sin^2\theta_w$ (from νN) gives Δr_3:

$$\Delta r_3 = 0.107 \pm 0.017 \pm 0.060 \tag{8.9}$$

The determination of radiative corrections in high statistics experiments would be of special interest as they carry indirect information on two unknown quantities: the masses of

47

the top quark and of the Higgs particle [82,84,85,86]. The variation of Δr with the Higgs mass in the range 10 GeV to 1 TeV is rather weak. An increase of M_H by a factor of 10 would increase Δr by about 10% for any M_t. The dependence of Δr on the masses of fermions coupled to W, Z is however more pronounced. In a model assuming 3 generations, a large mass splitting of any weak isospin doublet of fermions would decrease Δr. This applies to the (t, b) doublet in particular. Positive values of Δr, which are favoured by the data, imply an upper limit on the top quark mass of about 220 GeV/c^2.

A more general test of the Standard Model can be made by studying the correlation between M_W and $M_Z - M_W$. The mass difference measured in the electron channel by UA1 is:

$$M_Z - M_W = 10.4 \pm 1.4 \pm 0.8 \text{ GeV/}c^2. \tag{8.10}$$

The UA1 and UA2 measurements are shown in fig. 51 in the $M_Z - M_W$ versus M_Z plane. They are compared with the Minimal Standard Model expectations:

1) Based on the value of $\sin^2\theta_W$ from deep inelastic scattering experiments and M_Z (dashed region):

$$M_Z - M_W = M_Z \cdot (1 - \cos\theta_W) \tag{8.11}$$

2) Expressed in terms of A, M_Z and Δr, (a) for $\Delta r = 0.07$ and (b) for $\Delta r = 0$:

$$M_Z - M_W = M_Z - [(M_Z^2/2) + \{(M_Z^4/4) - (A^2 M_Z^2)/(1-\Delta r)\}^{1/2}]^{1/2}. \tag{8.12}$$

As can be seen from the error ellipses, the correlation between the mass difference and M_Z is not yet sensitive to the radiative correction Δr.

A summary of the measurements of the parameters of the Standard Model is given in Table 15. This table includes data from the electron and muon decay channels of the IVB's. Although suffering from much larger errors, the W and Z mass values, as found in the muonic decays, have also been used to determine $\sin^2\theta_W$ and ρ. They provide a second, entirely independent measurement, which agrees well with the results from the electron channel.

9. LIMITS ON NEW PARTICLES

The results on IVB production show impressive agreement with current Standard Model expectations. In this chapter we discuss results on searches for exotic processes in our IVB data samples.

9.1 Search for W', Z' bosons

Additional vector bosons arise naturally in many possible extensions of the minimal Standard Model of electroweak interactions [87]. Massive bosons, decaying into lepton pairs, will produce more energetic decay products, with a consequent improvement in energy resolution and detection efficiency in the electron channel. The detection and selection efficiency in the W' case increases from 61% for M_W=80 GeV/c^2 to 72% for $M_{W'}$=250 GeV/c^2. The same is true in the Z' case.

We simulated W' (Z') production and decay using standard couplings [88] and two sets of structure functions [31,33]. We also take into account the mass dependent selection efficiency for W', Z'. The calculated $\{\sigma{\cdot}B\}_{IVB'}$ was renormalized to our measured cross-sections at M_W and M_Z respectively for $\sqrt{s}$=0.630 TeV. We use the W$\rightarrow$ eν data and increase the statistics at $\sqrt{s}$=0.630 TeV by adding the events from $\sqrt{s}$=0.546 TeV with appropriate weights. The events from W$\rightarrow$ $\mu\nu$, $\tau\nu$ and Z$\rightarrow$ $\mu\mu$ are not included in the analysis, due to the poorer resolution in their transverse mass or mass distribution. The normalized W' and Z' cross-sections are found to be almost independent of the Q^2=$M_{IVB'}^2$ scale in the mass region of interest. The mass dependence of $(\sigma_{W'}{\cdot}B_{W'})$ and $(\sigma_{Z'}{\cdot}B_{Z'})$ is shown in fig. 52 for two sets of structure functions (DO1 and DFLM).

No W$\rightarrow$ eν or Z$\rightarrow$ ee candidates have been observed with electron-neutrino transverse mass M_T or electron-positron invariant mass M in excess of the expected distribution for standard model IVB decays (fig. 43). These null results can then be used to set limits on the production and decay of more massive W(Z)-like objects decaying into lepton pairs. With our present experimental sensitivity in the electron decay channels we get the following upper limits (90% C.L.):

$$(\sigma{\cdot}B)_{W'}<4.6 \text{ pb} \quad \text{and} \quad (\sigma{\cdot}B)_{Z'}<4.7 \text{ pb.} \tag{9.1}$$

Using the set of DFLM structure functions [33], indicated by the solid curve in fig. 52, these values are converted to lower mass limits for the W',Z' of

$$M_{W'} \geq 220 \text{ GeV}/c^2 \qquad\qquad M_{Z'} \geq 173 \text{ GeV}/c^2 \qquad\qquad (9.2)$$

at 90% C.L. These results are consistent with earlier results from this experiment [13], and with UA2 [89].

Additional vector bosons W' and Z' may exist, but with couplings different from the Standard Model ones. Normalizing the cross-section times branching ratio $(\sigma' \cdot B')_{IVB'}$ to those of the Standard Model vector bosons in terms of $R_c = (\sigma' \cdot B')_{IVB'}/(\sigma \cdot B)_{S.M.coupling}$, we obtain limits on $M_{W'}$ and $M_{Z'}$ as a function of R_c (fig. 53).

9.2 Search for a fourth generation heavy lepton

The possibility of a fourth generation of quarks and leptons is allowed by the Standard Model. The present limits on the number of neutrinos species [17,92] do not yet exclude this possibility. We denote the fourth generation leptons by (L, v_L). The W and Z could decay into these leptons, i.e.

$$W^{\pm} \to L^- \bar{v}_L \quad \text{or} \quad L^+ v_L \ ,$$
$$Z^0 \to L^- L^+ \quad \text{or} \quad v_L \bar{v}_L \ ,$$

if the masses of the new leptons allow such decays. Direct searches for a fourth generation charged lepton in e^+e^- experiments have placed a lower mass limit of 27.6 GeV/c^2 at 95% confidence level [93].

The semi-hadronic decays of the L, which have a total branching ratio of about 70%, provide a distinctive signature for the $W \to L\, v_L$ process: a large missing transverse energy in association with one or two high p_T jets. The background from $W \to \tau\, v_\tau$ with $\tau \to$ hadrons + v_τ decays, although larger than the L signal, does not pose a problem since most of the $W \to \tau\, v_\tau$ events are removed by the $L_\tau > 0$ cut (see section 4.3) and the residual background in the $L_\tau < 0$ region can be reliably estimated.

In our analysis we consider the following decays [16,94]:

$$W^{\pm} \to L^+ v_L \ / \ L^- \bar{v}_L \ ,$$
with $L^+ \to u\,\bar{d}$ or $c\,\bar{s} + \bar{v}_L$ and $L^- \to d\,\bar{u}$ or $s\,\bar{c} + v_L$.

It is assumed that the weak couplings of the new generation (L, ν_L) to the W is of universal strength, and that ν_L is massless. The $L^\pm$ decays into $t \bar{b} \bar{\nu}_L / b \bar{t} \nu_L$ are not considered because the mass of the top quark is not known and is expected to be large ($M_t > 44$ GeV/c^2) [48], thus their rates would be small due to the limited phase space available. For this analysis, a modified version [94] of the ISAJET Monte Carlo [27] is used to study the properties and to calculate the expected rate of the heavy lepton events. The decay of the W into a heavy lepton is done similarly to the $W \rightarrow \tau \nu_\tau$ decay. The production of wrong helicity L's as a function of the L mass is however included.

For masses of the L larger than 20 GeV/c^2, heavy lepton Monte Carlo events predominantely have $L_\tau < 0$ and $E_T^{jet} < 40$ GeV for the highest E_T jet in the event. Out of the 56 events in the missing transverse energy data sample [16], 24 have $L_\tau < 0$ and are classified as non $W \rightarrow \tau \nu$ events. Among these there are 22 mono-jet and 2 di-jet events. The distributions of E_T^{miss} and E_T^{jet} for these 24 events are shown in Figure 54. The curves show the Monte Carlo predictions for the expected contributions due to standard physics processes (W /Z and heavy flavor) and the jet-fluctuation background to the non $W \rightarrow \tau \nu$ sample. Figure 54(c) shows the E_T^{jet} distribution for the 24 events after the known backgrounds have been substracted. This distribution is compared to the expected contributions from heavy lepton events with $L_\tau < 0$. The E_T^{jet} distribution for a heavy lepton of 35 GeV/c^2 mass (solid curve) is clearly inconsistent with the background-subtracted data. However, we are not sensitive to a signal from a heavy lepton of 55 GeV/c^2 mass.(dashed curve).

From the sample of 24 events, 17 have $E_T^{jet} < 40$ GeV for the highest E_T jet in the event. Only these events are used to derive a limit on the L mass (M_L). The expected rate of heavy lepton events, for example for $M_L = 45$ GeV/c^2, is 7.6 ± 0.8 events. On the other hand, the Monte Carlo predicts a total of (17.8 ±3.7 ±1.0) events from the standard physics processes and the jet-fluctuation background. The contribution from $Z \rightarrow \nu_L \bar{\nu}_L$, where the Z is produced at large p_T and is accompanied by a recoil jet, must now be included in the total background (1.86 ±0.75 events). Using the above total background, the rate of heavy lepton events as a function of the L mass, and taking into account the statistical and systematic errors, the lower bound on the mass of the heavy sequential charged lepton is found to be $M_L > 41$ GeV/c^2 at 90% CL or $M_L > 35$ GeV/c^2 at 95% CL.[94]. In deriving this limit, we have not included the contribution of top quark processes (p $\bar{p} \rightarrow t \bar{t}$, $W \rightarrow t \bar{b}$, and $Z \rightarrow t \bar{t}$) in the total background to the non-$W \rightarrow \tau \nu$ sample. If included, it would increase the heavy lepton mass limit to $M_L > 48$ GeV/c^2 (90% CL) for $M_t = 40$ GeV/c^2.

9.3 Search for supersymmetric particles

i) $W \rightarrow \tilde{e} \, \tilde{\nu} \rightarrow e\nu \, \tilde{\gamma} \, \tilde{\gamma}$

The $W \rightarrow e\nu$ data sample is well suited to a search for the supersymmetric decay [90] of a W into a s-electron and s-neutrino, followed by the decay of the s-electron into an electron and a photino.

This process will result in events with isolated electrons and a significant missing energy. The electron and missing transverse energy will however be softer than for the conventional two body ($e\nu$) decays of the W. We therefore expect an excess of events at lower transverse mass M_T compared with the standard $W \rightarrow e\nu$ decay.

Assuming a massless photino, the branching ratios for given masses of the s-electron, $\tilde{e}$, and s-neutrino, $\tilde{\nu}$, can be calculated. Furthermore, in this process the decay angular distribution is symmetric in the W rest frame. In the lab-frame, however, we expect a slight enhancement in the $Q \cdot \cos\theta < 0$ hemisphere (opposite to the V-A asymmetry) as a result of the harder u-quark structure function. However, as already discussed in Section 7.3 we find that our energy and angular distribution are well described by (V-A) expectations for $W \rightarrow e\nu$, once the known $W \rightarrow \tau\nu$ and QCD backgrounds have been subtracted. We have used this agreement, along with the predicted branching ratio for $W \rightarrow \tilde{e} \, \tilde{\nu}$, to set limits on the left-handed s-electron and s-neutrino masses[45].

We have also used Monte Carlo simulations to estimate our theoretical sensitivity, and we find that this leads to a limit which is a few GeV lower than the experimental one. We therefore choose to use the conservative limit derived from the Monte Carlo. The 90% C.L. exclusion region in the selectron and sneutrino mass plane is shown in fig. 55. The limit for $M = M_{\tilde{e}} = M_{\tilde{\nu}}$, is $M \geq 32$ GeV/c^2 (90% C.L.). This limit is obtained with the full statistics available and a detailed Monte Carlo study of the SUSY processes.

ii) $Z \rightarrow \tilde{e} \, \tilde{e} \rightarrow ee \, \tilde{\gamma} \, \tilde{\gamma}$

This decay is characterized by a lower mass (e^+e^-) pair with significant missing energy. To be reasonably sensitive to this SUSY process, we have used a data selection similar to the standard $Z \rightarrow ee$ candidate selection (Section 3). The e^+e^- mass cut, however, has been removed. In addition we required that the electron pair should have opposite signs and that both tracks have $p_T > 2$ GeV/c. We find a limit of $M_{\tilde{e}} > 14$ GeV/c^2 (90% C.L.) assuming $M_{\tilde{\gamma}} = 0$ and that the left- and right-handed selectrons are degenerate. This limit is rather weak, owing to one particular event in the data. The unusual properties of this event ($M_{ee} = 52 \pm 2$ GeV/c^2, $E_T^{mis} = 20$ GeV) are due to an electron which is close to the vertical plane

in the electromagnetic calorimeter. The lower limit on $M_{\tilde{e}}$ which we would obtain by excluding this event would increase to 28 GeV/c^2. In the present data the sensitivity of the muonic decay channels is negligible in the Z case and marginal in the W case.

9.4   Search for heavy objects decaying into IVB's + jet

The rate and properties of jets associated to IVB's have been shown to be in agreement with QCD expectations from initial state bremsstrahlung. Nevertheless, we investigated the possibility that the W is the decay product of a heavier object decaying into a W and a jet. This is predicted in theories which consider the existence of massive coloured particles, which may decay into a W and a gluon [91].

We selected for this analysis a subsample of (W+1jet) events. In our $W \rightarrow e\nu$ sample there are 81 W-events associated with only one jet having transverse energy in excess of 7 GeV. We examined the invariant mass of the (W+jet)-system for these events (fig. 56). The longitudinal momentum of the W, needed for the calculations of the invariant mass, is obtained by the minimal p_L^W method (Section 6.1). The data have been corrected for the p_T^W dependent efficiency of the $W \rightarrow e\nu$ selection. Background contributions arise from $W \rightarrow \tau\nu$ decays. populating the low M(W+jet) region, and from QCD jet fluctuations with a fairly flat distribution in the W+jet mass.(in total 7.2±1.1 events) The curve is normalized to the sum of the total expected production cross-section [44] utilizing the jet rates predicted by ISAJET and the additional contributions from background sources.

There is good agreement between the measured spectrum and the prediction. The absence of any high mass state enables us to place a limit on the production of an object X decaying into a W plus a quark or gluon jet. In particular, for an object X with $M_X > 220$ GeV/c^2, the 90% C.L. upper limit relative to the W production cross-section is

$$\sigma(X \rightarrow W+\text{jet})/\sigma(W) < 0.019. \tag{9.5}$$

In this estimate we neglected changes in the acceptance due to differences in the momentum distribution of the W's or its polarization. Variations in the angular distribution of the lepton (isotropic, $\sin^2\theta$ or $\cos^2\theta$) would however change the efficiency by $<(20\text{-}30)\%$. Properties of W events with two jets have been discussed in the context of IVB production at large transverse momenta [14].

10. CONCLUSIONS

The discovery of the intermediate vector bosons at the CERN proton-antiproton collider is a major validation of the Standard Model.

We have measured the production and decay properties of the W and Z bosons at the centre of mass energies 546 GeV and 630 GeV. The W, Z cross-sections, their longitudinal and transverse momentum distributions and the characteristics of the rest of the event, including the associated production of high p_T jets, are in agreement with the QCD improved Drell Yan model expectations.

The W, Z masses determined in the electron, muon and tau decay channels agree with each other. The Standard Model parameters derived from the W and Z masses in the electron channel are in remarkable agreement with those obtained in the deep inelastic neutrino interactions.

There is no evidence in the current data for any exotic process leading to heavier intermediate vector bosons, heavy leptons or supersymmetric particles.

Acknowledgments

REFERENCES and FOOTNOTES

[1]   G. Arnison et al., Phys. Lett. **122B** (1983) 103.

[2]   G. Arnison et al., Phys. Lett. **126B** (1983) 398.

[3]   G. Arnison et al., Phys. Lett. **129B** (1983) 273.

[4]   G. Arnison et al., Phys. Lett. **134B** (1984) 469.

[5]   G. Arnison et al., Phys. Lett. **147B** (1984) 241.

[6]   A. Sirlin, Phys. Rev. **D22** (1980) 971;

W. J. Marciano and A. Sirlin, Phys. Rev. **D22** (1980) 2695;

C. H. Llewellyn Smith and J. A. Wheater, Phys. Lett. **105B** (1981) 486.

[7]   S. Drell and T. M. Yan, Phys. Rev. **25** (1970) 316; Ann. Phys. **66** (1971) 578.

[8]   S. Weinberg, Phys. Lett. **19** (1967) 1264; A. Salam, Proceedings of the 8th Nobel Symposium, Aspenaesgarden (1968) 367.

[9]   M. Banner et al., Phys. Lett. **122B** (1983) 476;

P. Bagnaia et al., Phys. Lett. **129B** (1983) 130;

P. Bagnaia et al., Z. Phys. **C24** (1984)1.

[10]   G. Arnison et al., Phys.Lett **166B** (1986) 484.

[11]   G. Arnison et al., Europhys. Lett. **1** (1986) 327.

[12]   G. Arnison et al., Phys. Lett. **135B** (1984) 250.

[13]   G. Arnison et al., Lettere al Nuovo Cimento **44** (1985)1.

[14]   C. Albajar et al., Phys. Lett. **193B** (1987) 389.

[15]   C. Albajar et al., Phys. Lett. **185B** (1987) 233.

[16]   G. Arnison et al., Phys. Lett. **139B** (1984) 115;

C. Albajar et al., Phys. Lett. **185B** (1987) 241;

C. Albajar et al., Phys. Lett. **198B** (1987) 261;

[17]   C. Albajar et al., Phys. Lett. **198B** (1987) 271.

[18]   A. Astbury et al. UA1 Proposal, CERN/SPSC **78/06** (1978).

[19]   M. Barranco-Luque et al., Nucl. Instr. & Methods **176** (1980) 175;

M. Calvetti et al., Proc. Int. Conf. on Instr. for Colliding Beam Physics, SLAC, SLAC-250 (1982) 16;

J. Timmer, Proc. 3rd Moriond Workshop on p$\bar{p}$ Physics, La Plagne (1983) 593;

M. Calvetti et al., IEEE Trans. Nucl. Sci. NS-30 (1983) 71.

[20]   M. Calvetti et al., Nucl. Instr. & Methods **176** (1980) 255;

B. Hallgren, H. Verweij, IEEE Trans. Nucl. Sci. NS-27 (1980) 333.

[21]   C. Cochet et al., Nucl. Instr. & Methods **A243** (1986) 45.

[22] B. Aubert et al., Nucl. Instr. & Methods **176** (1980) 195;

M. J. Corden et al., Nucl. Instr. & Methods **A238** (1985) 273;

C. Bacci et al., Nucl. Instr. & Methods **200** (1982) 195.

[23] K. Eggert et al., Nucl. Instr. & Methods **176** (1980) 217;

K. Eggert et al., Nucl. Instr. & Methods **176** (1980) 223;

R. Leuchs, Diplomarbeit, III Physikalisches Institut RWTH Aachen (1982).

[24] G. Bauer et al., Nucl. Instr. & Methods **A253** (1987) 179;

A. Bettini et al., Nucl. Instr. & Methods **A253** (1987) 189;

G. Bauer et al., Nucl. Instr. & Methods **A260** (1987) 101.

[25] A. Astbury et al., Nucl. Instr. & Methods **A238** (1985) 288.

[26] G. Arnison et al., Phys. Lett. **123B** (1983) 115;

G. Arnison et al., Phys. Lett. **132B** (1983) 21 .

[27] F. E. Paige and S. D. Protopopescu, ISAJET program, BNL-**29777** (1981), BNL-**38034** (1986).

[28] G. Altarelli et al., Nucl. Phys. **B157** (1979) 461;

G. Altarelli et al., Nucl. Phys. **B246** (1984) 12;

G. Altarelli et al., Z. Phys. **C27** (1985) 617.

[29] G. Altarelli and G. Parisi, Nucl. Phys. **B126** (1977) 298.

[30] E. Eichten at al., Rev. Mod. Phys. **56** (1984) 579;

E. Eichten et al., Rev. Mod. Phys. **58** (1986) 1065.

[31] D. W. Duke and J. F.Owens, Phys. Rev. **D30** (1984) 49.

[32] M. Glück, E. Hoffmann and E. Reya, Z. Phys. **C13** (1982) 119.

[33] M. Diemoz, F. Ferroni, E. Longo, and G. Martinelli, Z. Phys **C39** (1988) 31.

[34] D. Antreasyan et al., Phys. Rev. Lett. **45** (1980) 863; Phys. Rev. Lett. **47** (1981) 12; Phys. Rev. Lett. **48** (1982) 302.

[35] G. C. Fox et S. Wolfram, Nucl. Phys. **B168** (1980) 285;

T. Sjöstrand, Phys. Lett. **157B** (1985) 312;

T. D. Gottschalk, CALT-**68-1241** (1985).

[36] R. D. Field and R. P. Feynman, Nucl. Phys **B136** (1978) 1.

[37] G. Arnison et al., Nucl. Phys. **B276** (1986) 253;

P. Ghez and G. Ingelman, Z. Phys. **C33** (1987)465.

[38] C. Albajar et al., CERN-EP/**88-29**, submitted to Nucl. Phys. B;

J. Rushbrook (UA5 coll.) Proceedings of the XVI Int. Symp. on Multiparticle Dynamics, Kiryat Anavim, Israel (1985) 289.

[39] A. Ali et al., Nucl. Phys. **B292** (1987);

B. Van Eijk, Ph.D. Thesis, University of Amsterdam (1987).

[40] E. Locci, Ph.D. Thesis (1984), University Paris-Sud, CEA-N-**2399**.

[41] C. Stubenrauch, Ph.D. Thesis (1987), University Paris-Sud, CEA-N-2532.

[42] C. Perault, Ph.D. Thesis (1987), Laboratory LAPP-Annecy.

[43] E. Tscheslog, Ph.D. Thesis (1988), University of Aachen.

[44] R. Leuchs, Ph.D. Thesis (1988), University of Kiel.

[45] S. J. Haywood, Ph.D. Thesis (1988), University of Birmingham.

[46] C. Albajar et al., Phys. Lett. **186B** (1987) 237;
      C. Albajar et al., Phys. Lett. **186B** (1987) 247.

[47] C. Albajar et al., Z. Phys. **C37** (1988) 489.

[48] C. Albajar et al., Z. Phys. **C37** (1988) 505.

[49] C. Albajar et al., Phys. Lett. **200B** (1988) 380.

[50] F. Behrends et al., Nucl. Phys. **B202** (1982) 63;
      F. Behrends et al., Nucl. Phys. **B206** (1982) 61.

[51] J. Fleischer, F. Jegerlehner, Z. Phys. **C26** (1985) 629.

[52] R. Ansari et al., Phys. Lett. **186B** (1987) 452.

[53] R. Horgan and M. Jacob, Nucl. Phys. **179B** (1981) 441.

[54] J. Ransdell, Phys. Rev. **D38** (1988) 1616; Ph.D. Thesis, University of California, Riverside, CA (1987).

[55] G. Arnison et al., Phys. Lett. **136B** (1984) 294.

[56] J. Appel et al., Z. Phys. **C30** (1986) 1;
      R. Ansari et al., Phys. Lett, **B186** (1987) 440, and erratum;
      R. Ansari et al., Phys. Lett. **143B** (1987) 158.

[57] R. Voss, Proceedings of the 1987 International Symposium on Lepton and Photon Interactions at High Energies, Hamburg, July (1987).

[58] N. G. Deshpande et al., Phys. Rev. Lett. **54** (1985) 1757;
      F. Halzen et K. Mursula, Phys. Rev. Lett. **51** (1983) 857;
      K. Hikasa, Phys. Rev. **D29** (1984) 1939;
      N. Cabibbo, Proc. 3rd Topical Workshop on Proton-Antiproton Collider Physics, Rome 1983, CERN Yellow Report **83-04** (1983) 567.

[59] G. Altarelli et al., Phys. Lett. **151B** (1985) 457.

[60] A. S. Ito et al., Phys. Rev. **D23** (1981) 604.

[61] A. L. S. Angelis et al., Phys. Lett. **147B** (1984) 472;
      D. Antreasean et al., Phys. Rev. Lett. **45** (1980) 863; Phys. Rev. Lett. **47** (1981) 12; Phys. Rev. Lett. **48** (1982) 302.

[62] C. Albajar et al., Phys. Lett. **209B** (1988) 385.

[63] C. Albajar et al., Phys. Lett. **209B** (1988) 397.
      B. Mours, Ph D Thesis 1987, Laboratory LAPP, Annecy.

[64] G. Arnison et al., Phys. Lett. **172B** (1986) 461.

[65]   P. Aurenche et al., Nucl. Phys. **B297** (1988) 661;
       P. Aurenche et al., Phys. Lett. **140B** (1984) 87.

[66]   W. J. Stirling, Proceedings of the 6th Topical Workshop on pp Collider Physics,
       Aachen 1987.

[67]   S. D. Ellis, R. Kleiss et al., Phys. Lett. **154B** (1985) 435;
       S. Geer and W. J. Stirling, Phys. Lett. **152B** (1985) 373.

[68]   N. Arteaga-Romero et al., Phys. Rev. Lett. **52** (1984) 3.

[69]   M. Chaichian et al., Phys. Rev. **D25** (1982) 1.

[70]   D. Bailin and A. Love, Nucl. Phys. **B75** (1974) 159;
       S. Coleman and D. Gross, Phys. Rev. Lett. **31** (1973) 851;
       A. Zee, Phys. Rev. **D7** (1973) 3630.

[71]   R. Brandelik et al., Phys. Lett. **97B** (1980) 453.

[72]   G. Arnison et al., Phys. Lett. **136B** (1984) 294.

[73]   J. Ellis and I. Karliner, Nucl. Phys. **B148** (1979) 141.

[74]   G. Arnison et al., Phys. Lett. **123B** (1983) 108.

[75]   A. D. Martin et al., Z. Phys. **C14** (1982) 351.

[76]   G. Arnison et al., Phys. Lett **118B** (1982) 167.

[77]   R. Ansari et al., Phys. Lett. **186B** (1987) 440.

[78]   M. Jacob, Lett. al Nuovo Cimento **9** (1958) 826.

[79]   Particle Data Group, Phys. Lett. **170B** (1986) 1.

[80]   A. Sirlin, Phys. Rev. **D22** (1980) 971;
       W. J. Marciano, Phys. Rev. **D20** (1979) 274

[81]   W. J. Marciano and A. Sirlin, Phys. Rev. **D29** (1984) 945;
       W. J. Marciano and A. Sirlin, Phys. Rev. **D22** (1980) 2695.

[82]   F. Jegerlehner, Z. Phys. **C32** (1986) 195.

[83]   H. Abramowicz et al., Phys. Rev. Lett. **57** (1986) 298;
       J. V. Allaby et al., Phys. Lett. 177B (1986) 446.

[84]   U. Amaldi et al., Phys. Rev. **D36** (1987) 1385;
       J. V. Allaby et al., Z. Phys. **C36** (1987) 611.

[85]   G. Costa et al., Nucl. Phys. **B286** (1987) 325.

[86]   G. Gounaris et al., Preprint (1987) CERN-TH.4940/87, submitted to Z. Phys.

[87]   P. Langacker et al., Phys. Rev. **D30** (1984) 1470;
       U. Bauer et al., MPI-PAE/PTh 29/85 (1985);
       E. Cohen et al., Phys. Lett.**165B** (1985) 76;
       F. del Aguila et al., Nuc. Phys **B287** (1987) 419;
       D. London et al., Phys.Rev. **D34** (1986) 1530.

[88] We thank G. Martinelli for providing us with the relevant program for the calculations of the cross-sections and the DFLM structure functions.

[89] R. Ansari et al., Phys. Lett. **195B** (1987) 613.

[90] R. Barbieri et al., Phys. Lett. **127B** (1983) 458;
      R. M. Barnett et al., Phys. Rev. Lett. **51** (1983) 176;
      H. Baier et al., Phys. Lett **153B** (1985) 265.

[91] E. L. Berger and M.Jacob, Phys. Lett. **147B** (1984) 197;
      G. J. Gounaris and A. Nicolaidis, Phys. Lett. **148B** (1984) 239;
      A. de Rujula et al., Phys. Lett. **140B** (1984) 253.

[92] P. Colas, D. Denegri, C. Stubenrauch, Z. Phys. **C40** (1988) 527

[93] T. Kamae, Results from e^+e^- collisions, XXIV International Conference on High Energy Physics, Munich, August 4-10 1988.

[94] M.M. Mohammadi, Ph.D. Thesis (1987), University of Wisconsin-Madison

TABLE 1

Calorimetry

Calorimeter		Angular coverage θ (°)	Thickness No.rad. lengths	Thickness No.abs. lengths	Cell size Δθ (°)	Cell size Δφ (°)	Sampling step	Segmentation in depth	Resolution
Barrel	e.m.: gondolas	25-155	$26/\sin\theta$	$1.1/\sin\theta$	5	180	1.2 mm Pb 1.5 mm scint.	$3.3/6.6/9.9/6.6\ X_o$	$0.15/\sqrt{E}$
	hadr.: C's		-	$5.0/\sin\theta$	15	18	50 mm Fe 10 mm scint.	$2.5/2.5\ \lambda$	$0.8/\sqrt{E}$
End-cap	e.m. bouchons	5-25	$27/\cos\theta$	$1.1/\cos\theta$	20	11	4 mm Pb 6 mm scint.	$4/7/9/7\ X_o$	$0.12/\sqrt{E_T}$
	hadr.: I's	155-175	-	$7.1/\cos\theta$	5	10	50 mm Fe 10 mm scint.	$3.5/3.5\ \lambda$	$0.8/\sqrt{E}$
Calcom	e.m.	0.7-5	30	1.2	4	45	3 mm Pb 3 mm scint.	$4\times 7.5\ X_o$	$0.15/\sqrt{E}$
	hadr.	175-179.3	-	10.3	-	-	40 mm Fe 8 mm scint.	$6\times1.7\ \lambda$	$0.8/\sqrt{E}$
Very forward	e.m.	0.2-0.7	24.5	1.0	0.5	90	3 mm Pb 6 mm scint.	$5.7/5.3/5.8/7.7\ X_o$	$0.15/\sqrt{E}$
	hadr.	179.3-179.8	-	5.7	0.5	90	40 mm Fe 10 mm scint.	$5\times1.15\lambda$	$0.8/\sqrt{E}$

Table 2: **Electromagnetic calorimeter energy resolution and systematic uncertainties in the electron energy determination**

Resolution:

Intrinsic calorimeter resolution $\sigma(E)/E = k/\sqrt{E}$ (k = 0.15 in 1983, 0.21 in 1985)

Systematic Uncertainty:	$\delta E/E$ in %	δE in GeV
Cell-to-cell calibration uncertainties	± 3.0	
Pile-up effect from calorimeter granularity		± 0.5
Absolute energy scale calibration uncertainty	± 3.0	
Time dependence uncertainty of the energy scale	± 1.0	
Uncertainty from the cosmic, ^{60}Co and laser calibration	± 1.0	

Table 3: A summary of the selection requirements for isolated electrons in IVB events in √s=0.63TeV data (1984-1985)

Isolated electron selection:

Requirements:	Details:	Efficiency [%]:
i) Electromagnetic cluster	One or two adjacent electromagnetic calorimeter cells with E_T>15 GeV in pseudorapidity $|\eta|$<2.5.	85
ii) Cluster validation	Excluding the electron candidate, the sum of the transverse cells is <3 GeV/c. The centroid of the energy depositions in the four longitudinal samplings of the cells associated with the cluster are consistent with a single isolated electron.	95
iii) Associated track requirement	Candidate consistent with the presence of a charge track associated with the cluster with transverse momentum >15 GeV.	97
iv) Loose isolation (in a cone with ΔR=0.4)	Excluding the electron candidate, the sum of the transverse momenta of all the other tracks in the cone is <10% of the cluster transverse energy E_T. The cluster transverse energy E_T is >90% of the total E_T in the calorimeter cells (e.m. and hadronic) inside the cone.	96
v) Tight isolation (in a cone with ΔR=0.7)	Excluding the electron candidate, the sum of the transverse momenta of all other tracks in the cone is <3 GeV/c. Excluding the cluster cells, the total extra E_T in the calorimeter cells in the cone is <3.2 GeV.	96
vi) Electromagnetic shape	The hadronic energy associated with the cluster is E_{had}<0.6 GeV (1.5GeV) for clusters with pseudorapidity $|\eta|$<1.5 ($|\eta|$>1.5). The quality parameter is χ^2_R<50 [13]	94

| **efficiency for isolated electrons** | | **67 ± 2** |

Table 4: **A summary of the 1984-85 selection requirements for a) W $\rightarrow$ eν and b) Z $\rightarrow$ e$^+$e$^-$ events in the $\sqrt{s}$=0.63 TeV data (1984-85)**

a) W$^\pm$ $\rightarrow$ e$^\pm\nu$ selection:

Requirement:	Details:	Efficiency[%]:
online		
i) 1st + 2nd level trigger		96
offline		
ii) Isolated electron selection	Summarized in table 3	67
iii) Neutrino emission	Missing transverse energy >15GeV after validation	96
W$\rightarrow$ eν selection efficiency		**61 ±1.5**
iv) validation	visual inspection of events on an interactive display; rejection of obvious mis-selected events	

b) Z^0 $\rightarrow$ e$^+$e$^-$ selection:

Requirement:	Details:	Efficiency [%]:
online		
i)		100
offline		
ii) Isolated electron selection per electron	Summarized in table 3	67
iii) Second e.m. cluster	One or two adjacent e.m. calorimeter cells with E_T>8GeV.	
iv) Second cluster validation	As for first cluster; see table 4a.	
v) Second cluster isolation (in a cone ΔR=0.4)	Excluding the electron candidate, the sum of the transverse momenta of all the other tracks in the cone is <20% of the cluster E_T. The cluster E_T is >80% of the total cluster E_T in the calorimeter cells inside the cone.	
vi) Second cluster e.m. shape	The hadronic energy associated with the cluster E_{had} is either <1 GeV or <3% of the cluster energy.	
vii) Second cluster associated track	Event consistent with the presence of a charged track with transverse momentum >7 GeV/c associated with the cluster.	
viii) Mass cut	The invariant mass of the e$^+$e$^-$ pair >70 GeV/c^2	
Z $\rightarrow$ (e$^+$ e$^-$) selection (1984-85)		**69 ± 2**
ix) validation	visual inspection/scan of events on interactive display; rejection of obvious mis-selected events;	

Table 5: Summary of the selection requirements and efficiencies for the $W^{\pm} \to \mu^{\pm}\nu$ events from the 1984-85 data at $\sqrt{s}$ = 0.63 TeV. The selection starts from the sample of 1μ inclusive muons after filtering and loose selection.

$W^{\pm} \to \mu^{\pm}\nu$ selection:

Requirements:	Details:	Efficiency [%]:
online		
i) single muon trigger		39.1
	geometry averaged on activated trigger area: 51.5%	
	muon track efficiency: 92.4%	
	1st level trigger efficiency: 82.0%	
ii) 2nd level trigger		93.9
	1984: 168E code VENI: 87.1% [43]	
	1985: 168E code MUTIME: 100% [43]	
offline		
iii) CD track quality	selection on central drift chamber quantities:	64.
	number of track points ≥30; projected track length ≥40cm;	
	cut on quality (χ^2); cosmic rejection; kink rejection;	
iv) momentum cut	p_T(muon)≥15 GeV/c;	95.
v) improved CD track quality	quality cuts with optim. calibration constants and refit;	93.0
vi) μ association to CD track	matching of CD track with muon chamber track in	95.0
	direction and displacement of the two track segments;	
vii) isolation of muon /neutrino:	excluding the muon candidate, the sum of the transverse	87.0
	momenta of all other charged tracks in the cone ΔR=0.4	
	around the muon is ≤ 1 GeV. The transverse energy of the	
	calorimeter in the same cone is ≤ 3GeV. No calorimeter jet	
	with E_T>10GeV in a cone ΔR =0.7 around the muon.	
	Neither calorimeter jet (E_T>10 GeV) nor CD-jet	
	(p_T≥7.5 GeV/c^2) in the transverse plane in $\Delta\phi$≥150°	
	relative to the muon.	
viii) neutrino	$E_T(\nu)$>15GeV	95.
ix) total energy selection	selection according to total scalar energy ΣE≤480 GeV in the	96.3
	event, to reject multiple interactions in a single beamcrossing;	

$W \to \mu\ \nu$ detection efficiency (1984-85)	15.4 ±1.1

x) validation	visual inspection/scan of events on interactive display; rejection of cosmics, and obvious mis-selected events;

Table 6: Summary of the selection requirements and efficiencies for the $Z^0 \rightarrow \mu^+\mu^-$ events from the 1985 data at $\sqrt{s}=0.63$ TeV. The selection starts from the sample of 1μ inclusive muons after filtering and loose selection.

$Z \rightarrow \mu^+\mu^-$ selection:

Requirements:	Details:	Efficiency [%]:
online		
i) trigger	a) hardware dimuon trigger:	26.8
	both muon tracks hit the effective muon chambers	
	geometric acceptance: 46.7%	
	muon track efficiency for 2 tracks: 85.4%	
	1st level trigger efficiency for 2 tracks: 67.2%	
	or b) one muon hardware trigger:	37.4
	one muon hits the chamber, the second does not	
	geometric acceptance: 49.3%	
	muon track efficiency: 92.4%	
	1st level trigger efficiency: 82.0%	
ii) 2nd level trigger	a) for dimuon triggered events	100.
	or b) for single muon triggered events	100.
	1985: MUTIME	
offline		
a) Both muons in the effective muon chamber area:		
iii) CD track quality	one track requires same cuts as in the W selection;	79.5
	number of track points ≥ 30; projected track length ≥ 40cm;	
	cut on quality (χ^2); cosmic ray rejection; kink rejection;	
	second track lower quality requirements for the CD track;	
	minimum ionizing deposition in the calorimeter;	
	invariant mass >50 GeV/c^2	
iv) p_T cut	one muon: $p_T > 15$ GeV/c; second muon: $p_T > 10$GeV/c	89.1
or b) One muon in the effective area, second muon not:		
v) CD track quality	one track requires same cuts as in the W selection;	63.8
	number of track points ≥ 30; projected track length ≥ 40cm;	
	cut on quality (χ^2); cosmic rejection; kink rejection;	
	second track less quality requirements for the CD track;	
	minimum ionizing deposition in the calorimeter;	
	invariant mass >50 GeV/c^2	
vi) p_T cut	First muon: $p_T > 15$ GeV/c, second muon $p_T > 10$ GeV/c	94.7

$Z \rightarrow \mu^+\mu^-$ selection efficiency (1985)	**41.5±3.3**

vii) validation	visual inspection of events on interactive display; rejection of cosmics and obvious mis-selected events;	

Table 7: **Summary of the selection requirements and efficiencies for the $W^{\pm} \to \tau^{\pm}\nu$ events in the (1984 -85) data**

$W^{\pm} \to \tau^{\pm}\nu$ selection:

Requirements:	Details:	Efficiency [%]:
branching ratio $\tau \to$ hadrons		64.
online:		
i) trigger		45.
	a) electromagnetic transverse energy $E_T>10$ GeV in two adjacent electromagnetic calorimeter elements or b) jet trigger with $E_T>25$ GeV in $|\eta|<2.5$ or c) jet trigger $E_T>15$GeV and transverse energy imbalance trigger >17GeV	
offline:		
ii) missing transverse energy selection		30.
	a) missing transverse energy $E_T>15$ GeV and at least 4 times larger than the resolution $0.7 * \sqrt{\Sigma E_T}$	
	b) one or more jets with $E_T>12$ GeV and $|\eta|<2.5$	
	c) one or more tracks in the CD with $p_T>1$GeV in a cone $\Delta R<0.4$ around the calorimeter jet axis	
	d) isolation of missing transverse energy: rejection of events with observed jets ($E_T>8$GeV, $|\eta|<2.5$) within $\pm30^o$ of the missing energy direction	
	e) veto on coplanar jet activity: rejection of events with calorimeter jets ($E_T>8$GeV, $|\eta|<2.5$) or a cental detector jet($p_T>5$GeV) pointing to within 150-210 degree in the direction of the highest E_T jet.	
	f) veto of events which contain an electron ($E_T>10$GeV) and muons ($p_T>3$GeV)	
iii) τ- selection	$L_\tau>0$	78.
	using τ decay characteristics:	
$W \to \tau\nu$ ($\tau \to$ hadrons) efficiency		**6.8 ± 0.4**
iv) validation	visual inspection/scan of events on interactive display; rejection of cosmics and obvious mis-selected events;	

Table 8: Summary of selection requirements and efficiencies for W → c$\bar{\text{s}}$, Z → c$\bar{\text{c}}$ and Z → b$\bar{\text{b}}$ event candidates in the 1984-85 data taken at √s =0.630 TeV. The selection starts from the sample of 1μ inclusive muons after filtering and tight selection.

Requirements:	Details:	Efficiency [%]:		
online				
i) single muon trigger		43		
	geometry averaged on activated trigger area: 60 % muon chamber track efficiency: 92.4 % 1st level trigger efficiency: 82.0 % 2nd level trigger efficiency: 93.9 %			
offline				
i) muon track reconstruction	number of CD track points ≥20; track length in bending plane ≥40cm; cut on track quality; cosmic ray rejection; kink rejection; leakage rejection; 4σ matching between trajectories of muon chambers and CD track in position and direction;	54		
		W→c$\bar{s}$	**Z→c$\bar{c}$**	**Z→b$\bar{b}$**
ii) muonic decay of c or b quark	both quarks from Z can decay muonically; b-quarks can have 2nd generation muonic decays;	9.1	18.0	45.0
iii) muon	$p_T^{\mu} >8$ GeV/c	12.3	14.0	20.5
iv) jet opposite muon	A jet with E_T>10 GeV and |η|<2 recoiling from the muon direction with |ΔΦ(μ - jet)| >90°; Jet must be greater than ±20° from the vertical in the transverse plane to avoid cracks in the calorimetry;	88.4	88.0	86.3
v) jet accompanying muon	A jet within the cone $\Delta R = \sqrt{(\Delta\Phi^2 + \Delta\eta^2)}$ ≤1 around the muon in pseudorapidity -azimuth space. Jet defined by UA1 jet algorithm with the requirement E_T> 2.5 GeV. Jet must have |η|<2 and be more than ±20° from the vertical.	91.9	92.6	92.5
	efficiency for detection b/c decays of inter-mediate vector bosons via muonic decay	**0.2**	**0.5**	**1.7**

Table 9: Number of background events from different sources contributing to the IVB samples used for the calculations of the cross-sections. No top quark contribution included.

Decay mode	Type of Background	$\sqrt{s} = 0.546$ TeV	$\sqrt{s} = 0.630$ TeV
a) $W \to e\nu$:			
	QCD	3.40 ± 1.8	4.7 ± 1.3
	$W \to \tau\nu, \quad \tau \to e\nu\nu$	3.36 ± 0.4	14.6 ± 1.1
		6.8 ± 2.0	19.3 ± 1.7
b) $Z \to ee$:			
	$Z \to \tau\tau, \quad \tau \to e\nu\nu$	< 0.1	0.1 ± 0.02
	$Z \to b\bar{b}, c\bar{c}$	< 0.1	0.1 ± 0.01
	$b, c \to e$		
		< 0.1	0.2 ± 0.02
c) $W \to \mu\nu$:			
	$W \to \tau\nu, \ \tau \to \mu\nu\nu$	0.45 ± 0.07	2.6 ± 0.4
	$b, c \to \mu$	0.15 ± 0.07	0.3 ± 0.13
	$\pi, K \to \mu\nu$	$0.1 \ \pm 0.05$	0.4 ± 0.2
		0.7 ± 0.10	3.3 ± 0.5
d) $Z \to \mu\mu$:			
	$\pi, K \to \mu\nu$	0.03	0.14 ± 0.01
	$Z \to \tau\tau, \ \tau \to \mu\nu\nu$	0.03	0.15 ± 0.04
	DY	0.01	0.05 ± 0.02
		0.07 ± 0.03	0.35 ± 0.16
e) $W \to \tau\nu$:			
	$W \to e\nu, \mu\nu, \tau\nu$		
	$(\tau \to e\nu, \mu\nu)$		1.6 ± 0.4
	$Z^0 (\to \nu\nu) + \text{jet}$		0.3 ± 0.3
	$Z^0 \to \tau\tau$		0.4 ± 0.2
	$W/Z \to$ heavy flavours		< 0.1
	jet fluctuations		0.4 ± 0.07
			2.7 ± 0.6

Table 10: UA1 event samples, efficiencies, backgrounds, and integrated luminosities for the various W and Z^0 samples. In total 398 W and 52 Z events were detected.

$\sqrt{s}$ (TeV)	Channel	Events	Background Events [a]	Efficiency	Luminosity (nb^{-1})
0.546	$W \to e\nu$	59	6.8 ± 2.0	0.69 ± 0.03	136 ± 20
	$W \to \mu\nu$ [b]	10	0.70 ± 0.10	0.16 ± 0.02	108 ± 16
	$Z^0 \to e^+e^-$	4	< 0.1	0.69 ± 0.03	136 ± 20
	$Z^0 \to \mu^+\mu^-$ [b]	4	0.07 ± 0.03	0.37 ± 0.05	108 ± 16
0.630	$W \to e\nu$	240	19.3 ± 1.7	0.61 ± 0.02	568 ± 85
	$W \to \mu\nu$	57	3.3 ± 0.5	0.15 ± 0.01	551 ± 83
	$Z^0 \to e^+e^-$	29	0.20 ± 0.02	0.69 ± 0.02	568 ± 85
	$Z^0 \to \mu^+\mu^-$	15	0.35 ± 0.16	0.40 ± 0.02	555 ± 83
0.546 + 0.630	$W \to \tau\nu$ [b]	32	2.7 ± 0.6	$0.068 \pm 0.004 \pm 0.007$ [c]	686 ± 103

a) Note : no contributions from top quark production and semileptonic decay have been included in these background estimates.

b) Numbers for this channel have been updated since our earlier publications.

c) This additional systematic error is due to the uncertainty on energy scale and τ selection.

Table 11: Cross-sections times branching ratios (σ·B); a comparison of UA1 results, UA2 results [56], and theoretical expectations [28].

Source	$\sqrt{s}$ (TeV)	Channel	σ·B (nb) *) $M_t = 44$ GeV/c²	$M_t = 80$ GeV/c²
UA1	0.546	$W \to e\nu$	$0.53 \pm 0.08 \pm 0.09$	$0.55 \pm 0.08 \pm 0.09$
UA1		$W \to \mu\nu$	$0.54 \pm 0.17 \pm 0.12$	$0.56 \pm 0.18 \pm 0.12$
UA2		$W \to e\nu$	–	$0.61 \pm 0.10 \pm 0.07$
Theory +)		$W \to \ell\nu$	$0.38^{+0.12}_{-0.06}$	$0.46^{+0.15}_{-0.07}$
UA1	0.630	$W \to e\nu$	$0.61 \pm 0.04 \pm 0.09$	$0.63 \pm 0.05 \pm 0.10$
UA1		$W \to \mu\nu$	$0.61 \pm 0.08 \pm 0.11$	$0.63 \pm 0.08 \pm 0.11$
UA2		$W \to e\nu$	–	$0.57 \pm 0.04 \pm 0.07$
Theory +)		$W \to \ell\nu$	$0.48^{+0.13}_{-0.07}$	$0.48^{+0.13}_{-0.07}$
UA1	0.546+0. 630 **)	$W \to \tau\nu$	$0.63 \pm 0.13 \pm 0.12$	$0.63 \pm 0.13 \pm 0.12$
UA1	0.546	$Z^0 \to e^+e^-$	$0.042^{+0.033}_{-0.020} \pm 0.006$	$0.042^{+0.033}_{-0.020} \pm 0.006$
UA1		$Z^0 \to \mu^+\mu^-$	$0.098^{+0.078}_{-0.046} \pm 0.020$	$0.098^{+0.078}_{-0.046} \pm 0.020$
UA2		$Z^0 \to e^+e^-$	$0.116 \pm 0.039 \pm 0.011$	$0.116 \pm 0.039 \pm 0.011$
Theory +)		$Z^0 \to \ell^+\ell^-$	$0.043^{+0.013}_{-0.007}$	$0.044^{+0.014}_{-0.008}$
UA1	0.630	$Z^0 \to e^+e^-$	$0.074 \pm 0.014 \pm 0.011$	$0.074 \pm 0.014 \pm 0.011$
UA1		$Z^0 \to \mu^+\mu^-$	$0.066 \pm 0.017 \pm 0.011$	$0.066 \pm 0.017 \pm 0.011$
UA2		$Z^0 \to e^+e^-$	$0.073 \pm 0.014 \pm 0.007$	$0.073 \pm 0.014 \pm 0.007$
Theory +)		$Z^0 \to \ell^+\ell^-$	$0.053^{+0.016}_{-0.010}$	$0.054^{+0.017}_{-0.011}$

+) ℓ = e or μ. Theoretical cross - sections for σ_w and σ_z at $\sqrt{s}$=0.54 TeV and 0.63 Tev are taken from [28]. The leptonic branching ratios assumed are B_w = 0.089, B_z = 0.033 for M_t = 44 GeV/c² (N_V = 3), and B_w = 0.11, B_z = 0.034 for M_t= 80 GeV/c².

*) The first error on the measured cross - sections is statistical, and the second error systematic.

**) The σ·B for this channel is the luminosity weighted average of the two energies. The result is slightly different from the one quoted in reference [15] due to an improved evaluation of the integrated luminosity at $\sqrt{s}$ = 0.630 TeV. The luminosities are 118 nb⁻¹ (568 nb⁻¹) at $\sqrt{s}$ = 0.546 (0.630) TeV.

Table 12:   Summary of IVB (σB) ratios at two CMS energies

σB (630) / σB (546)

IVB channel	UA1 no top contribution	UA2 [56]	Theory
W→ eν	1.14 ± 0.18 ± 0.06	0.93 ± 0.17	
W→ μν	1.14 ± 0.40 ± 0.18	--	1.26 ± 0.02[28], 1.30 [33]
Z → e e	1.80 ± 1.40 ± 0.40	0.60 ± 0.30	
Z → μ μ	0.70 ± 0.60 ± 0.20	--	1.23 [28], 1.31 [33]

Table 13: Average charged multiplicity $<N_{ch}>$, mean transverse momentum $<p_T>$ and sum of the transverse momenta (Σp_T) for rest of W events and minimum bias events *.

Characteristic	W events	Minimum bias events
mean charged multiplicity $<N_{ch}>$	20.4± 0.8± 1.2	14.3± 0.1± 0.9
mean transverse momentum $<p_T>$ of charged particles in GeV/c	0.66±0.01±0.01	0.52±0.01
scalar sum of transverse momenta of charged particles (Σp_T) in GeV/c	13.9± 0.6± 0.8	7.68±0.04±0.46

*) All values are given for particles with $p_T > 0.15$ Gev/c and $|\eta| < 2.5$.
The first error is statistical, the second is systematic.

Table 14 : Measured Masses and Widths of W's and Z's

Channel	Masses and Widths in GeV/c^2
Electron decay	
M_W	$82.7 \pm 1.0 \pm 2.7$
Γ_W (90% C.L.)	< 5.4
M_Z	$93.1 \pm 1.0 \pm 3.0$
Γ_Z (90% C.L.)	< 5.2
M_W - M_Z	$10.4 \pm 1.4 \pm 0.8$
Muon Decay	
M_W	$81.8 ^{+6.0}_{-5.3} \pm 2.6$
M_Z	$90.7 ^{+5.2}_{-4.8} \pm 3.2$
M_W - M_Z	$8.9 ^{+7.4}_{-7.7} \pm 1.9$
Tau Decay	
M_W	$89.0 \pm 3.0 \pm 6.0$

The first error is statistical, the second is systematic.

Table 15 : Measurements of Standard Model Parameters

	IVB Electron Decay	IVB Muon Decay	
$\sin^2\hat{\theta}_w$	0.211 ± 0.025	–	From νN experiments $0.233 \pm 0.003 \pm 0.005^{*}$
$\sin^2\tilde{\theta}_w$	$0.219 \pm 0.005 \pm 0.014$	$0.223 \, ^{+\,0.033}_{-\,0.029} \pm 0.014$	
ρ	$1.010 \pm 0.028 \pm 0.020$	$1.05 \pm 0.16 \pm 0.05$	$\rho = 1$, in Minimal Standard Model
Δr_1	$0.037 \pm 0.100 \pm 0.067$	–	Calculated Δr [82] 0.072 ± 0.002
Δr_2	$0.128 \pm 0.023 \pm 0.060$	–	

The first error is statistical, the second is systematic.

* Error coming from theoretical uncertainties

FIGURE CAPTIONS

Fig. 1   The Feynman diagrams for the hadronic production of vector bosons V in QCD at leading and next to leading order: a) Drell-Yan (0th order), b) QCD virtual correction, c) QCD annihilation process with gluon radiation, d) QCD Compton process.

Fig. 2   A side view of the UA1 experiment at the time of the W and Z discovery 1982-1983.

    a   - The central detector

    b   - The electromagnetic calorimeter (gondola, bouchon)

    c   - The coil

    d   - The hadronic calorimeter (and the iron field return) (C's, I's)

    e   - The external muon chambers

    f   - The forward calorimeters (Calcom)

    g   - The very forward calorimeters

    h   - Instrumented magnetized iron side wall (added in 1984)

Fig. 3   A general view of the UA1 experiment (the forward and very forward calorimeters are not drawn). The two halves of the apparatus have been opened to show the CD. Labels are as in fig. 2.

Fig. 4   Cut-away diagram of the central detector showing the orientations of the wire planes in the central and forward chambers.

Fig. 5   CD electronics block diagram (case of two tracks).

The left and right side signals from the preamplifiers are summed (for the ionization F and the drift time t measurement) and combined for the charge division Z. The resulting signals are sampled and digitized every 32 ns, while a 3-bit time interpolator (INT) gives the drift time with a precision of 4 ns. The digital information is directly written in a double 128x16 bit memory, so that the data are stored before the next beam crossing.

Fig. 6   a) A schematic drawing of two opposite gondolas.

b) A central region module of the hadron calorimeter.

Fig. 7   Percentage energy resolution $\sigma(E)/E$ in the gondolas.

Fig. 8   The structure of endcap "Bouchon" calorimeters.

Fig. 9   A top view of the UA1 detector. The implementation of the side wall (h), the forward shielding (j) and the limited streamer tubes (i,i') was done in 1984/85.

       a   - The central detector

       b,b'   - The electromagnetic calorimeter (b=gondola; b'=bouchon)

       c   - The coil

       d,d'   -The hadronic calorimeter (and the iron return)(d= C's, d'=I's)

       e,e'   - The external muon chambers (e=side; e'=forward)

       f   - The forward calorimeters (Calcom)

       g   - The very forward calorimeters

       h   - Instrumented magnetized side iron wall

       i,i'   - Limited streamer tubes (i= side; i'= forward)

       j   - Front absorber iron

       k   - Rails for moving the platform of the experiment to the garage position

Fig. 10   Schematic view of the muon drift chambers. Two units of four planes are stacked whereas the tubes in adjacent planes are staggered in order to resolve the left-right ambiguity. The trigger logic is also indicated.

Fig. 11   a) View of the side walls showing the limited streamer tubes and the drift chamber planes. The momentum is measured using the deflection in the magnetized iron.
b) Expanded view of a limited streamer tube chamber showing the two orthogonal planes of tubes and of pick-up strips.

Fig. 12   The efficiencies for the electron trigger in a) and for the muon trigger in b). The hardware trigger efficiency is given by the solid line. The dashed-dotted line shows the overall efficiency after an additional on-line software selection.

Fig. 13   Comparison of momentum measurement in the central track detector and the energy measurement in the electromagnetic calorimeter for electrons from a $W \to e\nu$ sample; (1/p-1/E) is divided by the corresponding experimental errors. Superposed is the result from a detector simulation allowing for bremsstrahlung from the electron.

Fig. 14   Precision of the overall muon momentum measurement. The stretch distribution of muon momentum measurements with (p_o) and without (p_{CD}) muon chamber information (direction and angles of the track).

Fig. 15   Correction factor to be applied to the measured p_T^W distribution, combining the effects of resolution (dominant at low p_T^W) and of acceptance for the electron decay channel.

Fig. 16   Distribution of a) electron transverse energy, and b) neutrino transverse energy for $W \rightarrow e\nu$. The background contributions from QCD two-jet events and $W \rightarrow \tau\nu$ events are shown.

Fig. 17   The invariant mass distribution for e^+e^- pairs with relaxed Z selection cuts.

Fig. 18   Transverse muon momentum distribution in $W \rightarrow \mu\nu$ events. 6 events are outside the range of the scale of the plot. The hatched area shows the background contribution from $W \rightarrow \tau\nu$ decay modes. Only data from $\sqrt{s}=0.63$ TeV are included. The solid curve is the Monte Carlo prediction.

Fig.19   UA1 sample for isolated unlike sign dimuons with $p_T>3$GeV/c for both tracks including the Z candidates. The events below the mass of 50 GeV/c^2 have been taken from dimuon events obtained by different cuts than in the Z search. Events in the mass range $1<M_{\mu\mu}< 6$GeV/c^2 are from low mass dimuons [63], the ones $6<M_{\mu\mu}<50$ GeV/c^2 are from high mass dimuons [46].

Fig. 20   Distribution of τ-log-likelihood function for the data (solid histogram), the $\tau \rightarrow$ (hadrons $+\nu$) Monte Carlo events (solid line) and the UA1 jet data (dashed curve), normalized to the 56 events; τ-candidates are defined as $L_\tau>0$.

Fig. 21   Distribution of missing transverse energy of W's in the $W \rightarrow \tau\nu$ decay mode ($\tau \rightarrow$ hadrons + neutrino).The background contribution (mainly from events with W decays into electrons or muons) is indicated by the hatched area.

Fig. 22   Experimental distribution of the (jet-jet-μ-ν_T) mass without background subtraction. The curves are the Monte Carlo predictions with full simulation of the UA1 detector measurement errors for the processes $W \rightarrow c \bar{s}$ (dashed), $Z \rightarrow c \bar{c}$, $b \bar{b}$ (dashed-dotted) and the sum of these two (solid line).

Fig. 23 Experimental distribution of the (jet-jet-μ-ν_T) mass (histogram), after p/K background subtraction. The solid curve is the full ISAJET Monte Carlo prediction (including 2→3 processes) from c $\bar{c}$ and b $\bar{b}$ production, normalized to the total number of events. The dashed curve shows the contribution of lowest order (2→2) processes.

Fig. 24 Partial cross-sections versus CMS energy, a) for W→$\ell\nu$ production, and b) for Z→$\ell\ell$ production. The theoretical predictions and their error bands on the total W and Z production cross-sections are taken from ref. [28], and the leptonic branching ratios for W→$\ell\nu$ and Z→$\ell\ell$ have been calculated for the assumption that there is no kinematically allowed W→t $\bar{b}$ and Z→t $\bar{t}$ decay (M_t>M_W-M_b).

Fig. 25 Measurements and theoretical predictions for a) W→$\ell\nu$ and b) Z→$\ell\ell$ partial cross-section as function of M_{top}. The line labelled 1 represent the predictions [28] used in fig 24a,b. The line labelled 2 includes a 20% increase due to the BCDMS result as discussed in the text. The uncertainties are indicated by the error bars. The hatched bands represent the measurements. The statistical and systematic errors have been combined in quadrature .

Fig. 26 Feynman |x| distribution for a) the W's from electron data (244 events at $\sqrt{s}$=0.630 TeV and 50 events at $\sqrt{s}$=0.546 TeV, DO1 structure function), b) the Z's from the combined electron and muon data [43 events, EHLQ1], and c) the W →$\mu\nu$ data (61 events, EHLQ1). The data are background subtracted and corrected for acceptance and resolution. In the W→eν case an additional correction due to bias from the x_W extraction procedure is included. Data and expectations are normalied to the total number of events.

Fig. 27 W → eν data ($\sqrt{s}$=0.63TeV; |p|≥2σ_p; 190 events) and expectations of the Q.x$_w$ distributions (Q is the W charge): a) with harder u- than d-quark distribution according to EHQL1, and b) same d-quark distribution as the one used for u-quarks in EHQL1. The data are background subtracted and corrected for acceptance, resolution and bias-effects from the x_w extraction procedure. Data and expectations are normalized to the total number of events.

Fig. 28 Correction factors (ratio of generated to reconstructed plus selected Monte Carlo events) for the the two cases discussed in fig.27: a) u-quark distribution harder than than d-quark distribution according to EHQL1, and b) same d-quark distribution as the one used for u quarks in EHQL1 (dashed curve).

Fig. 29 a) The d- quark and b) the u-quark structure functions sampled by W production. They are derived from the W→ev ($\sqrt{s}$=0.63 TeV) data with well defined charge of the lepton ie. |p|>2σ_p (190 events). The data are background subtracted and corrected for acceptance, resolution and biases coming from the x_w extraction procedure. Data and expectations using EHQL1 structure functions are normalized to the total number of events.

Fig. 30 Transverse momentum distribution of a) W events (muon and electron channels combined), and b) Z events (muon and electron channels combined). Data are background, acceptance and resolution corrected. The hatched sub-histogram shows the contribution from events in which at least one hadronic jet with transverse momentum ≥7GeV/c is observed. Quoted event numbers are uncorrected. The curve shows the QCD prediction of ref. [28] with DO1 structure functions. Note the change in scale in the abscissa for a).

Fig. 31 Transverse momentum distribution of W events (electron and muon channels combined). The data are corrected for resolution and acceptance. The curves show the QCD predictions from ref. [28] with extrapolations based on ISAJET (dashed line) for p_T^W >60 GeV/c.

Fig. 32 W transverse momentum distribution in the low and intermediate p_T^W range, and sensitivity to the scale parameter Λ_{QCD}. Data are background subtracted, while acceptance and resolution are folded into the theoretical predictions of [28].

Fig. 33 Mean transverse energy of lepton pairs versus CMS energy. The curve has been taken from ref. [59], the ISR and Fermilab data from ref. [60,61].

Fig. 34 Inclusive transverse momentum distributions for W's, jets [64], direct photons [62], and nearly on-shell photons from low mass dimuons [63] as measured in the UA1 experiment. The QCD predictions are from Stirling [66] scaled by 1.5 for jet cross-section and from Aurenche et al.[65] for direct photons. The line describing the W-cross-section is from Altarelli et al.[28].

Fig. 35 Distribution of the number of jets associated to the W → $\ell\nu$ (a) and Z → $\ell\ell$ (b) sample. Data are corrected for the p_T^W dependent selection bias of the W's. The

QCD curve includes resolution effects and jet efficiency. The integral of corrected data and the QCD curve are normalized to unity.

Fig. 36 Energy distribution of the jets in 357 events of the W→$\ell\nu$ sample; Data are corrected for acceptance (p_T^W) and jet energy. The QCD curve includes resolution effects.The prediction is normalized to the total number of observed events.

Fig. 37 Angular distribution of the jets in the W → ev sample. Only events with one jet above threshold are used. The mass of the (W+jet)-system has to exceed 100 GeV/c^2.

Fig. 38 The Gottfried-Jackson frame is defined in the following way: beginning with the 4-vectors of the leptons, the proton and the antiproton, one performs a Lorentz-transformation into the CMS of the lepton pair. Then one takes the CMS-momentum of the antiproton and defines its direction as the z-axis. The vector product of the proton momentum with the antiproton momentum gives the y-axis and the cross product of this vector with the z-vector gives the x-axis.

Fig. 39 The polar angular distribution in the Gottfried-Jackson frame for electrons from W decays with $p_T^W \geq 7$GeV/c for a) the vector gluon hypothesis and b) the scalar gluon hypothesis. Data are corrected for acceptance and resolution. The solid lines are the best fit to the data, the dashed line is the theoretical expectation for the chosen gluon spin assignment.

Fig. 40 Charged track transverse momentum distribution for W-spectator and mimimum-bias events. For reasons of clarity the data points in the minimum bias events case have been omitted below 2.5GeV/c. The curves show the results of fitting the distributions.

Fig. 41   a) Mean transverse momentum $<p_T>$, b) mean charged particle multiplicity $<N_{ch}>$, and c) sum of the transverse momenta Σp_T as a function of the W transverse momentum p_T^W ; the level in minimum-bias events is shown by the dashed line.

Fig. 42 The transverse mass distribution of the W's detected in the electron decay mode, corrected for acceptance and resolution.The shaded area shows the background contribution from W→$\tau\nu$ decays and QCD fluctuations.

Fig. 43   The enhanced transverse mass distribution of the W's in the electron decay mode (149 events).

Fig. 44   The experimental inverse transverse mass distribution $1/M_T$ of the W's in the muon decay mode. The dotted line shows the background contribution from $W \to \tau \nu$ decays with $\tau \to \mu \nu \nu$. The solid line represents the mass fit.

Fig. 45   Distribution of transverse mass of W's in the $W \to \tau \nu$ decay mode ($\tau \to$ hadrons + neutrino).The background contribution (mainly from non identified W's in the electron and muon decay mode) is indicated by the hatched area.

Fig. 46   The Z mass distribution from the events in the electron decay mode (24 events).

Fig. 47   The Z mass distribution from events in the muon decay mode , a) using only the momentum information (18 events, 3 events are above 160 GeV/c^2), and b) using momentum information and energy balance in the calorimeter (14 events).

Fig. 48   Decay angular distribution of W 's from the electron decay mode. The shaded band shows the expected contribution from annihilation processes involving wrong polarity sea-quarks only.

Fig. 49   Decay angular distribution of Z's (electron and muon decay modes combined, 33 events) for well measured events. The solid line corresponds to the fit which gives $\sin^2\theta_w = 0.24$.

Fig. 50   Relation between the measured k parameter in the Z decay angular distribution to the Weinberg angle $\sin^2\theta_W$ in the Standard Model.

Fig. 51   Confidence contours (68%) in the $(M_Z\text{-}M_W)$ versus M_Z plane taking into account the statistical error (dashed line) and with statistical and systematic errors combined in quadrature (solid line). The shaded region is allowed by the average of recent low-energy measurements of $\sin^2\theta_w$.The upper dashed dotted curve (a) is with radiative corrections, the lower one (b) without radiative corrections.

Fig. 52   Calculated cross-section times branching ratio for a) W' and b) Z' production and decay, assuming standard couplings to quarks and leptons. $(\sigma \cdot B)$ is normalized to the measured cross-sections at $\sqrt{s}=0.630$ TeV of the known IVB's in the electron

decay mode. The events from $\sqrt{s}=0.546$ TeV have been added by transforming them to an equivalent number of events at $\sqrt{s}=0.630$ TeV. The 90% C.L. upper limits on $(\sigma \cdot B)_{W'}$ and $(\sigma \cdot B)_{Z'}$ are shown.

Fig. 53   The W'(Z') lower mass limit (90% CL) shown as a function of the W'(Z') coupling strength. R_c is the coupling strength relative to the standard model coupling strength (R_c=1).

Fig.54   Distributions of (a) E_T^{miss}, (b) E_T^{jet} (for the highest E_T jet in the event), and (c) background-subtracted E_T^{jet} (points with error bars) for the 24 events of the non $W \rightarrow \tau \nu$ sample. In (a) and (b) the curves show the Monte Carlo predictions including all known standard model and instrumental background sources. In (c) the solid and dashed curves are the expected contributions to the non $W \rightarrow \tau \nu$ sample from a heavy lepton of 35 and 55 GeV/c^2 mass, respectively.

Fig. 55   The 90% confidence level lower limit exclusion region for the masses of the selectron and sneutrino estimated from the supersymmetric $W \rightarrow \tilde{e}\tilde{\nu}$ decay channel, assuming a subsequent decay $\tilde{e} \rightarrow e\tilde{\gamma}$

Fig. 56   The (W+1jet) mass distribution for events with one reconstructed jet with transverse momentum larger 7 GeV. The data are corrected for p_T^W acceptance. The curve shows the prediction from ISAJET including event selection, background contributions, detector simulation .

FIG.1

FIG.2

FIG.3

forward chamber

central chamber

$\vec{B}$

forward chamber
anode plane
cathode plane

1.30m

2m

2m

6m

2m

p

p

FIG.4

FIG.5

8 light guides
to PM's

Lead-scintillator
stack

R = 130 cm

22,5 cm

BBQ
bars

36 cm

to PM's

FIG. 6a

Air-Gap

Electromagnetic calorimeter

Iron-Gap

BBQ-Bars

MAGNET COIL

FIG. 6b

FIG.7

to PM

position detector

lead
scintillator
petal

FIG.8

FIG.9

Particle
track

Projected
track

600mm

2 level trigger:

uses drift-time
information

from
vertex

fast trigger:

uses pattern of
hit tubes

FIG.10

a) 60cm IRON WALL   MUON CHAMBERS

200mm   200mm   200mm   600mm

PLANES of LIMITED STREAMER TUBES

b)

FIG.11

a)

UA1 ELECTRONS

—— Hardware trigger
--- Hardware x 168E

EFFICIENCY ε

ELECTRON ENERGY E_T^{elm} (GeV)

b)

MUONS UA1

—— Hardware trigger
--- Hardware x 168E

Efficiency ε

Muon momentum p_T (GeV/c)

FIG.12

FIG.13

The figure shows a histogram titled "233 W→ev" plotting Number of Electrons versus $\frac{1/p-1/E}{\sigma}$ (Standard Deviations). The legend indicates Data (●) and Monte Carlo (—).

FIG.14

CORRECTION FACTOR

p_T^W (GeV/c)

W → eν

● EHLQ1
○ DO1

FIG. 15

FIG. 16a

FIG. 16 b

UA1
92 EVENTS

QCD – background

$Z^\circ \rightarrow e^+ e^-$

INVARIANT MASS $M(e^+ e^-)$ (GeV/c^2)

EVENTS PER 4 GeV/c^2

FIG.17

FIG.18

FIG.19

FIG.20

FIG.21
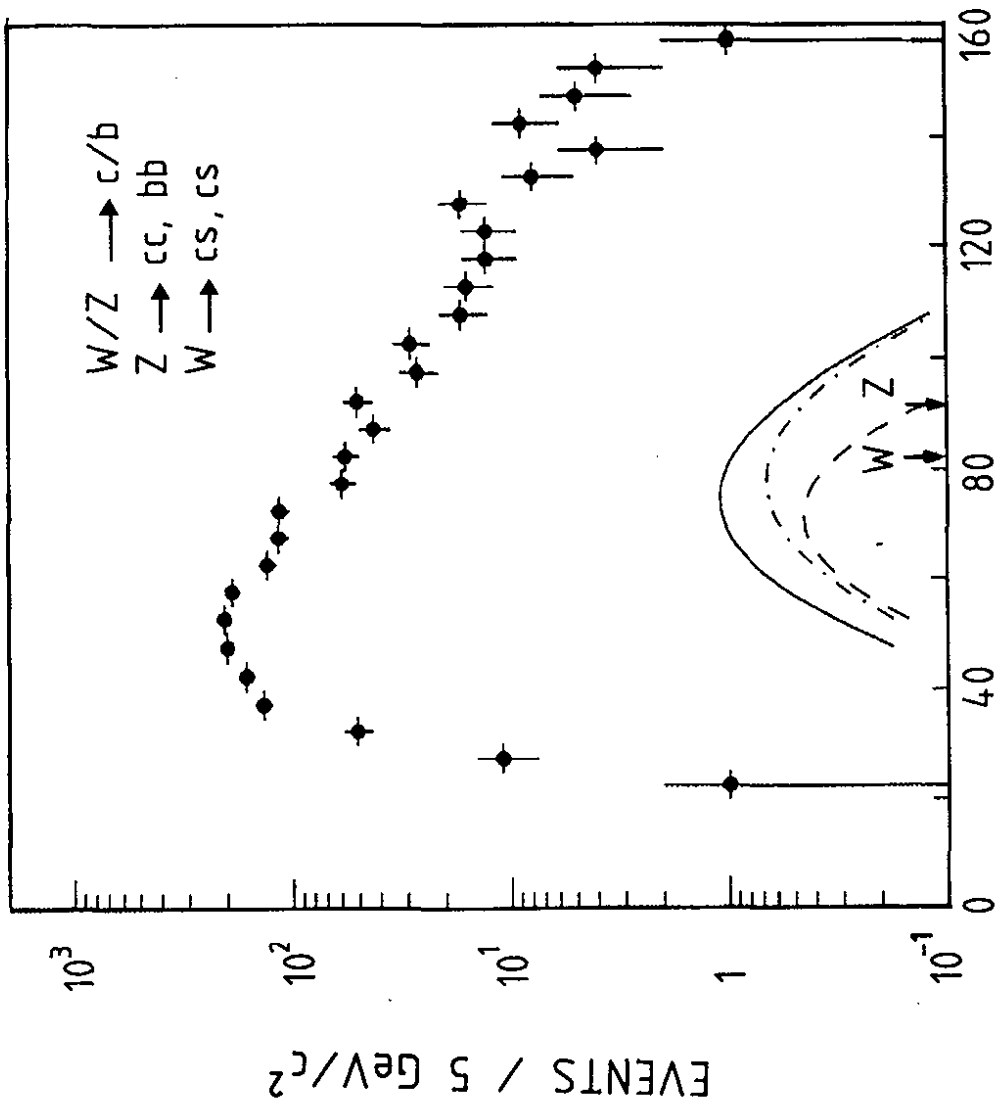
FIG.22

FIG. 23

FIG.24.a.

FIG.24.b.

UA1. √s = 0.630 TeV

W ⟶ lν
Data, with band of
(statistical + systematic) errors

Altarelli et al.
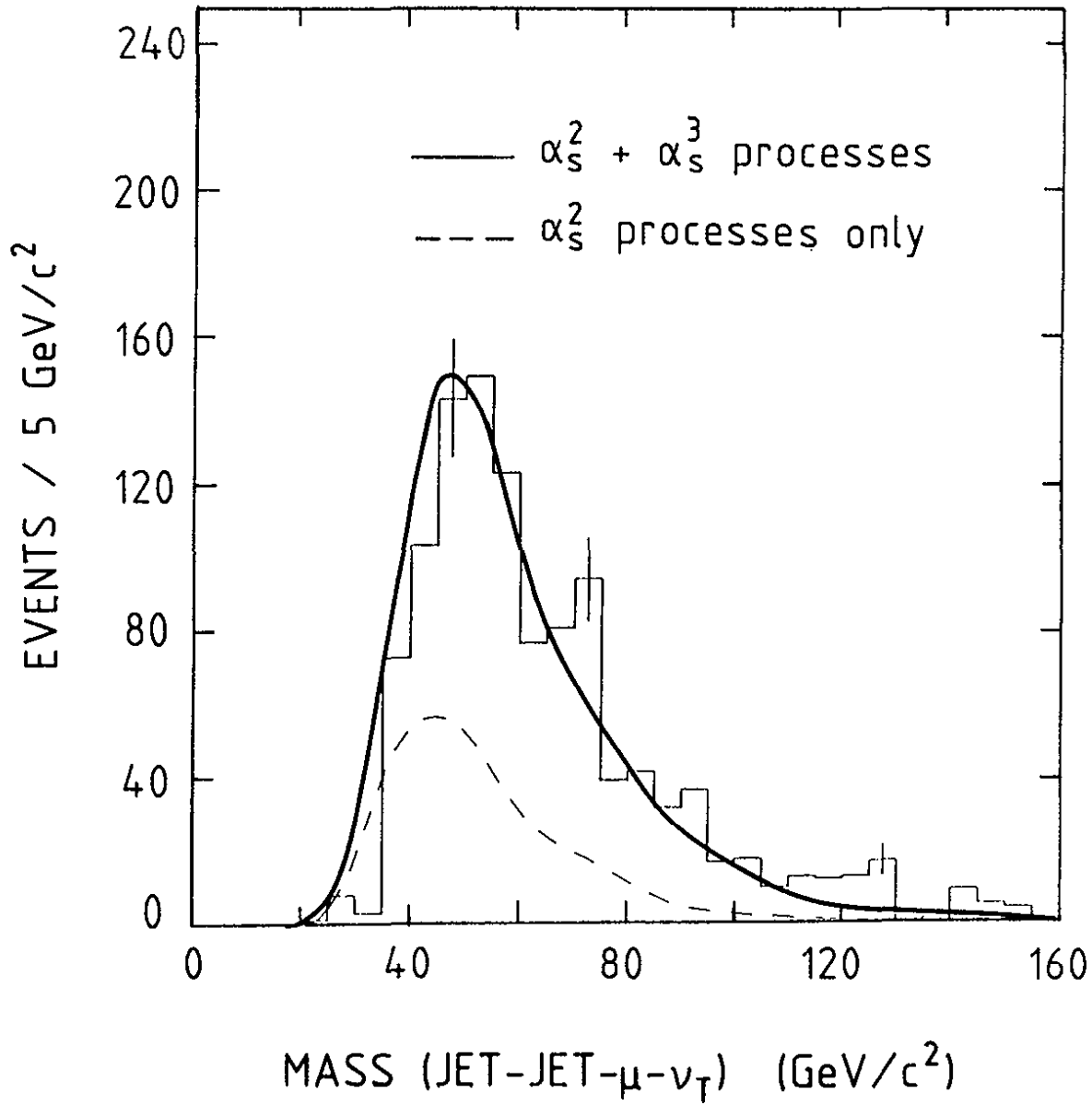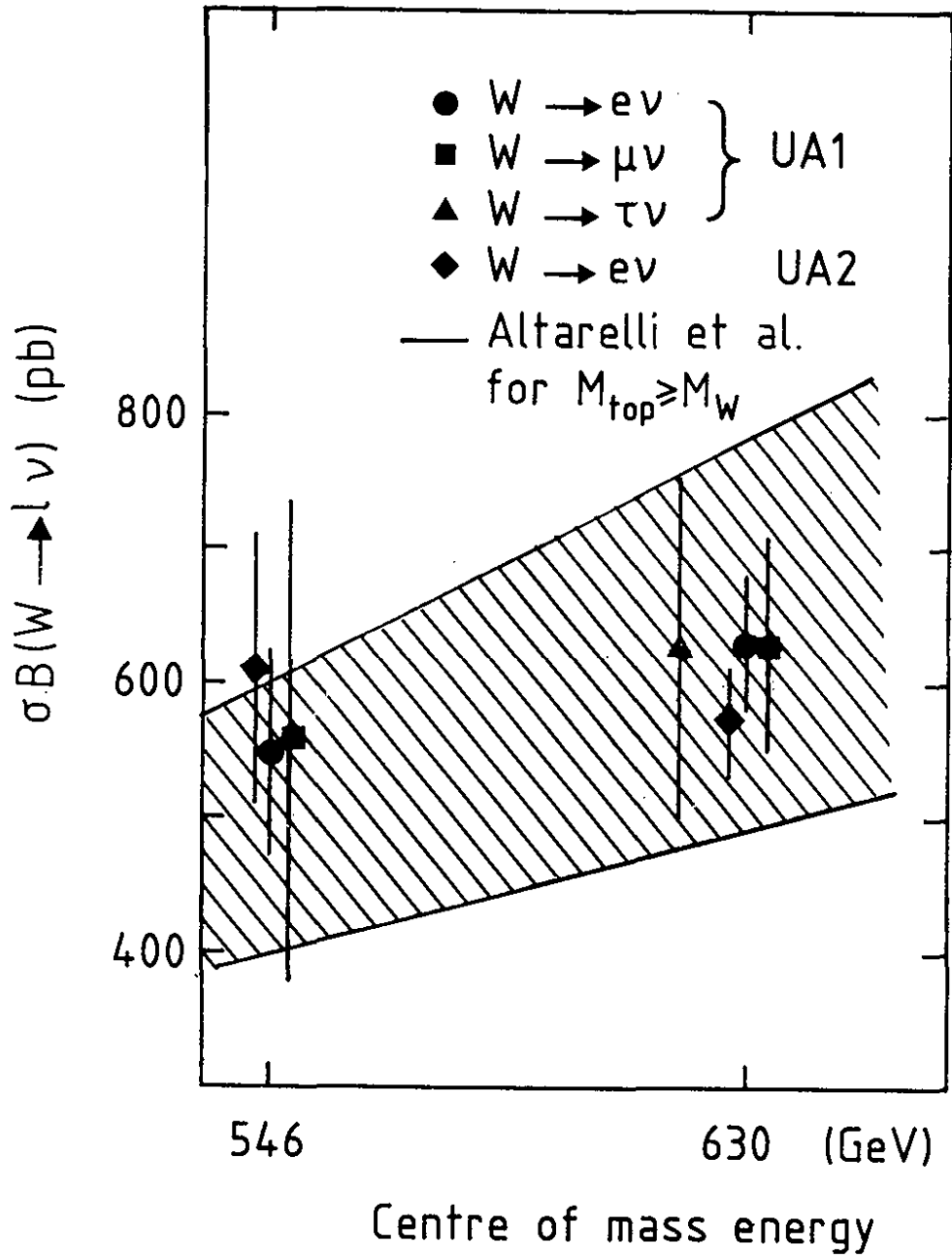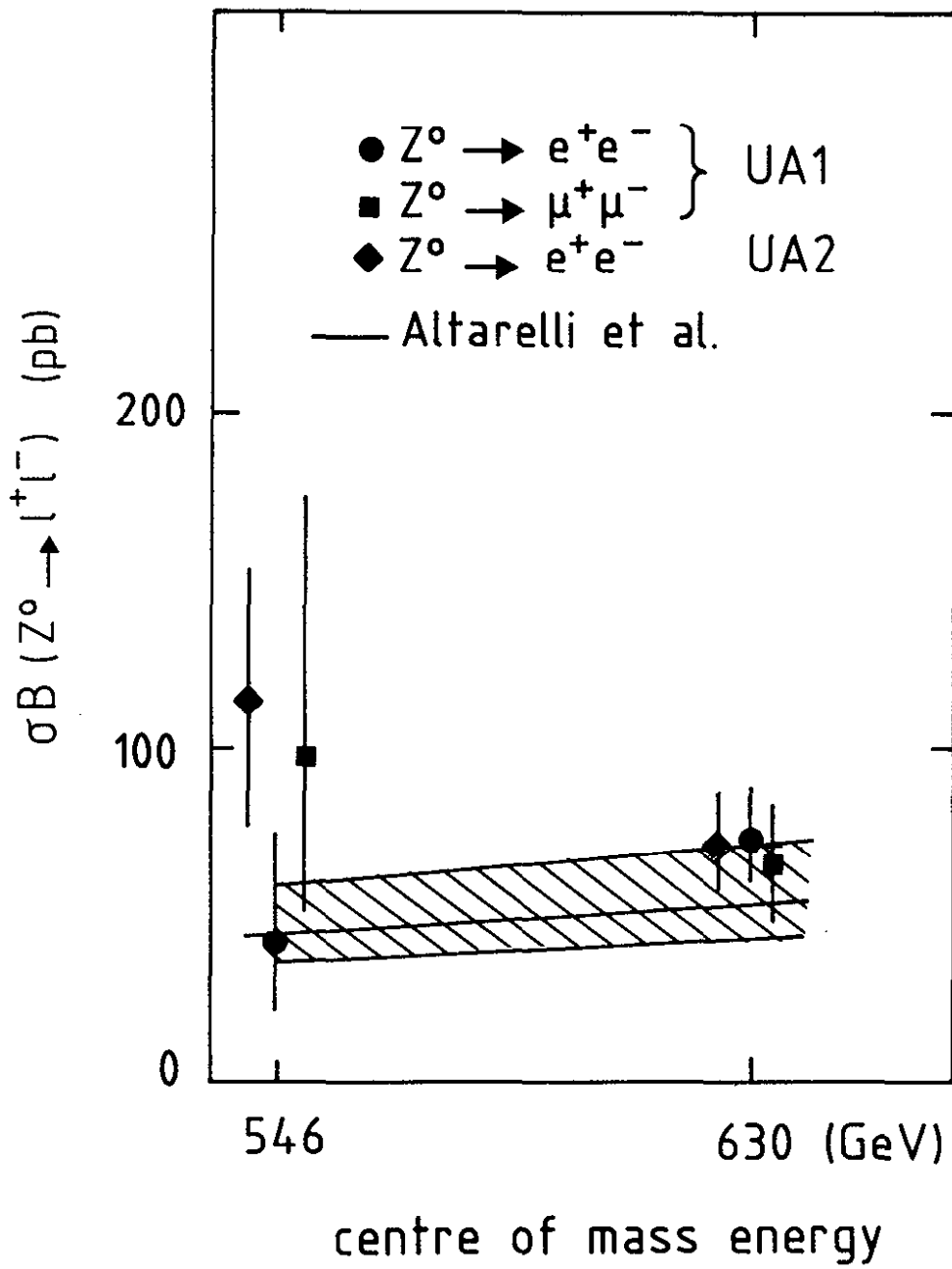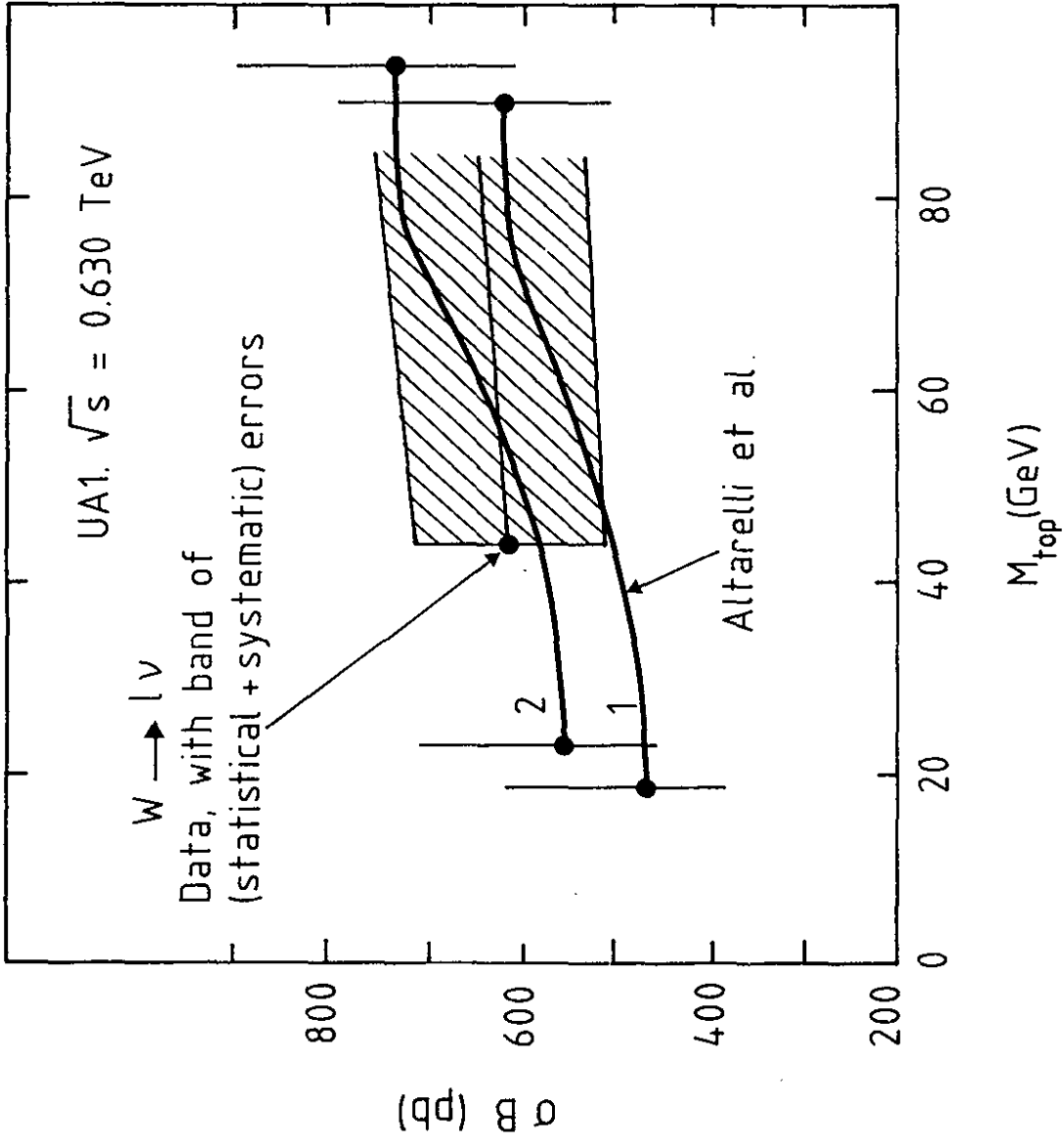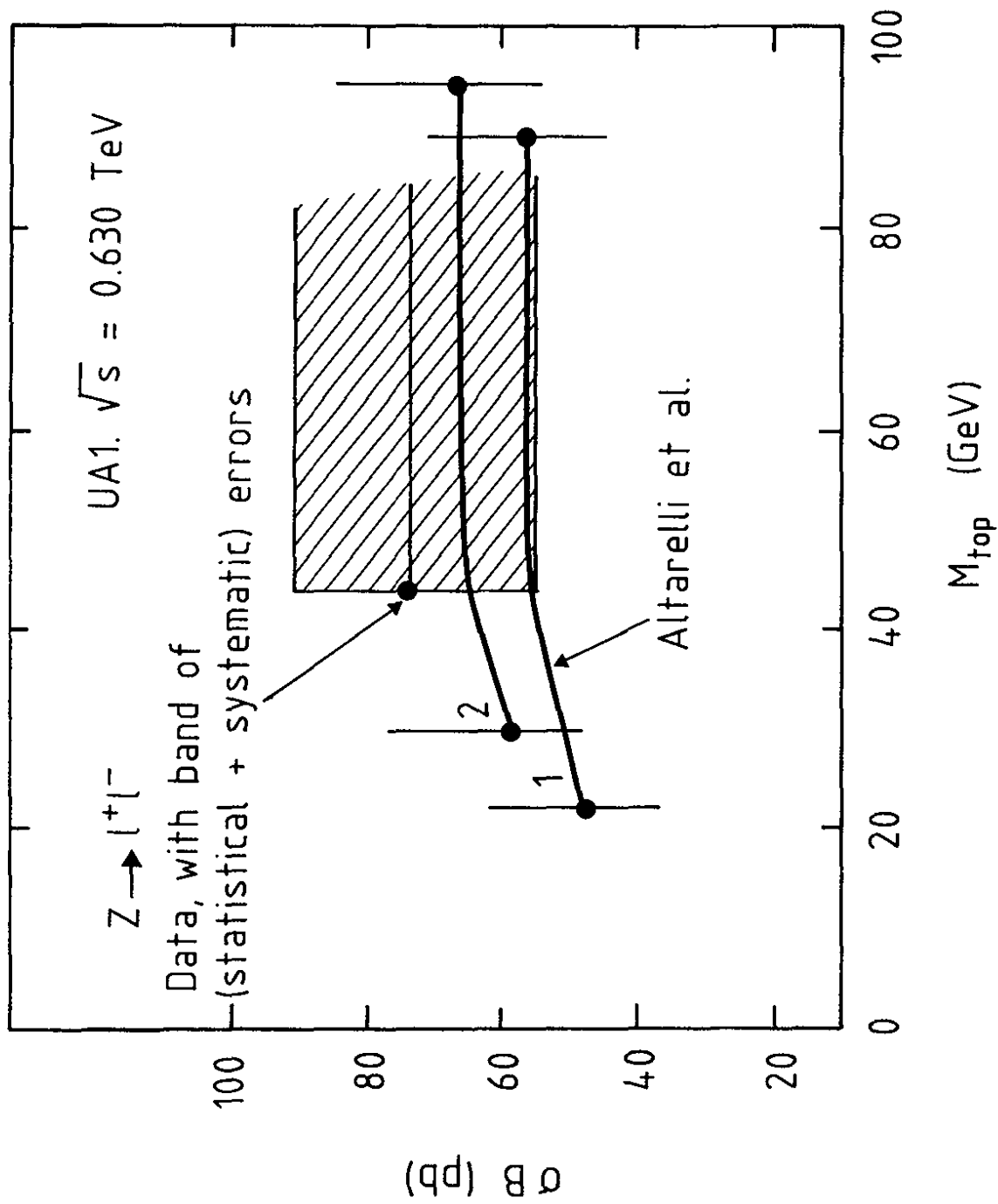
FIG. 25a

FIG. 25b
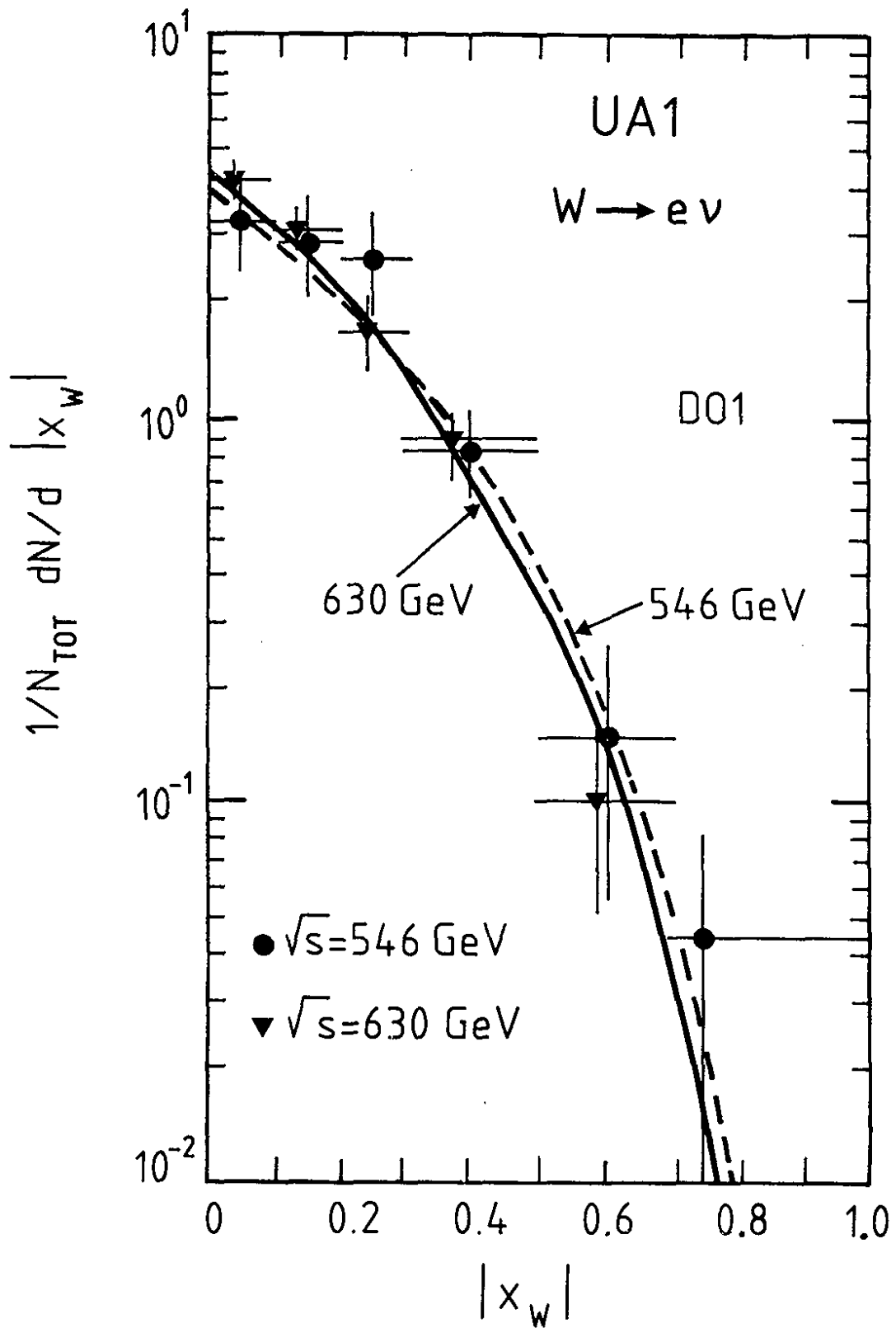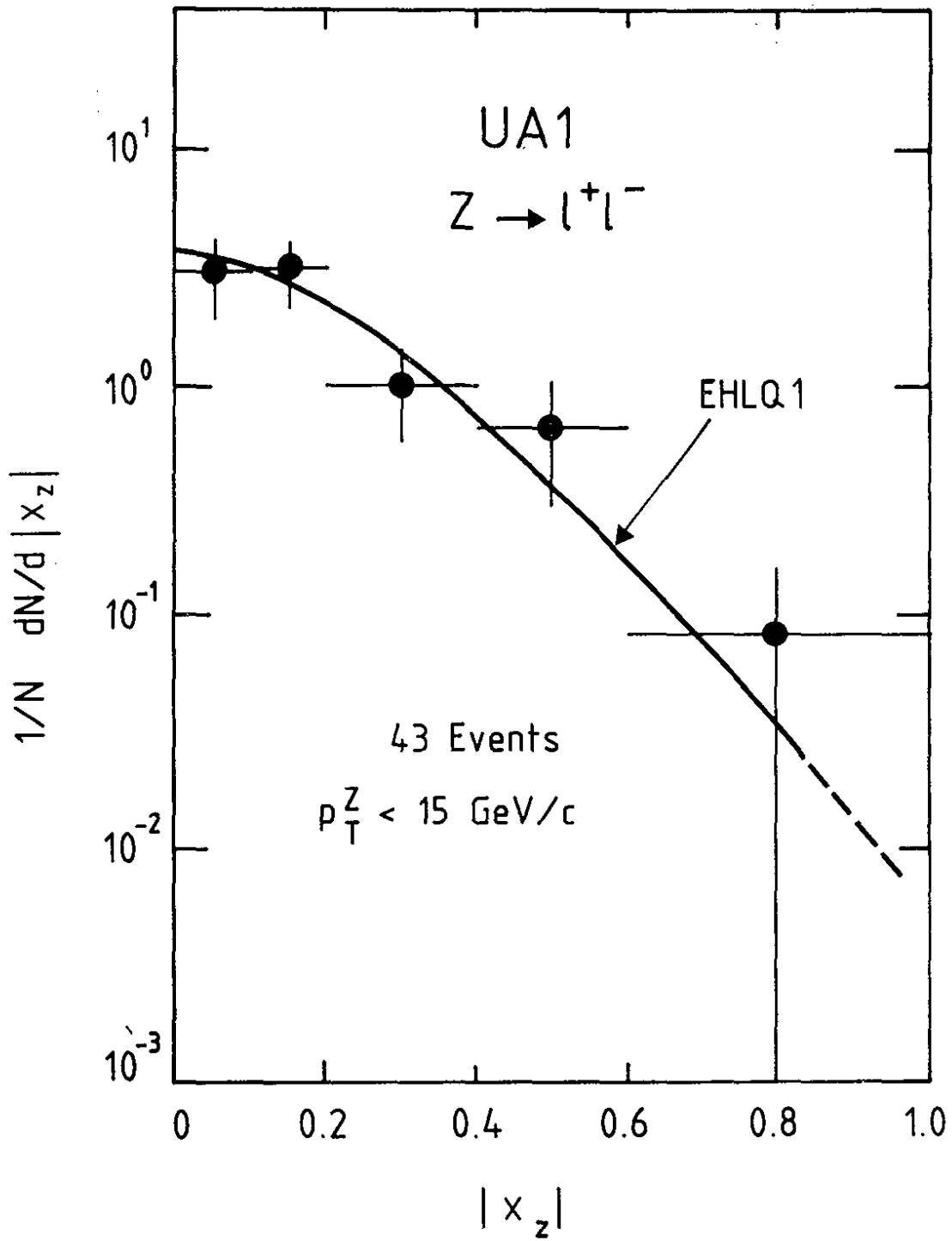
FIG. 26a

FIG.26.b
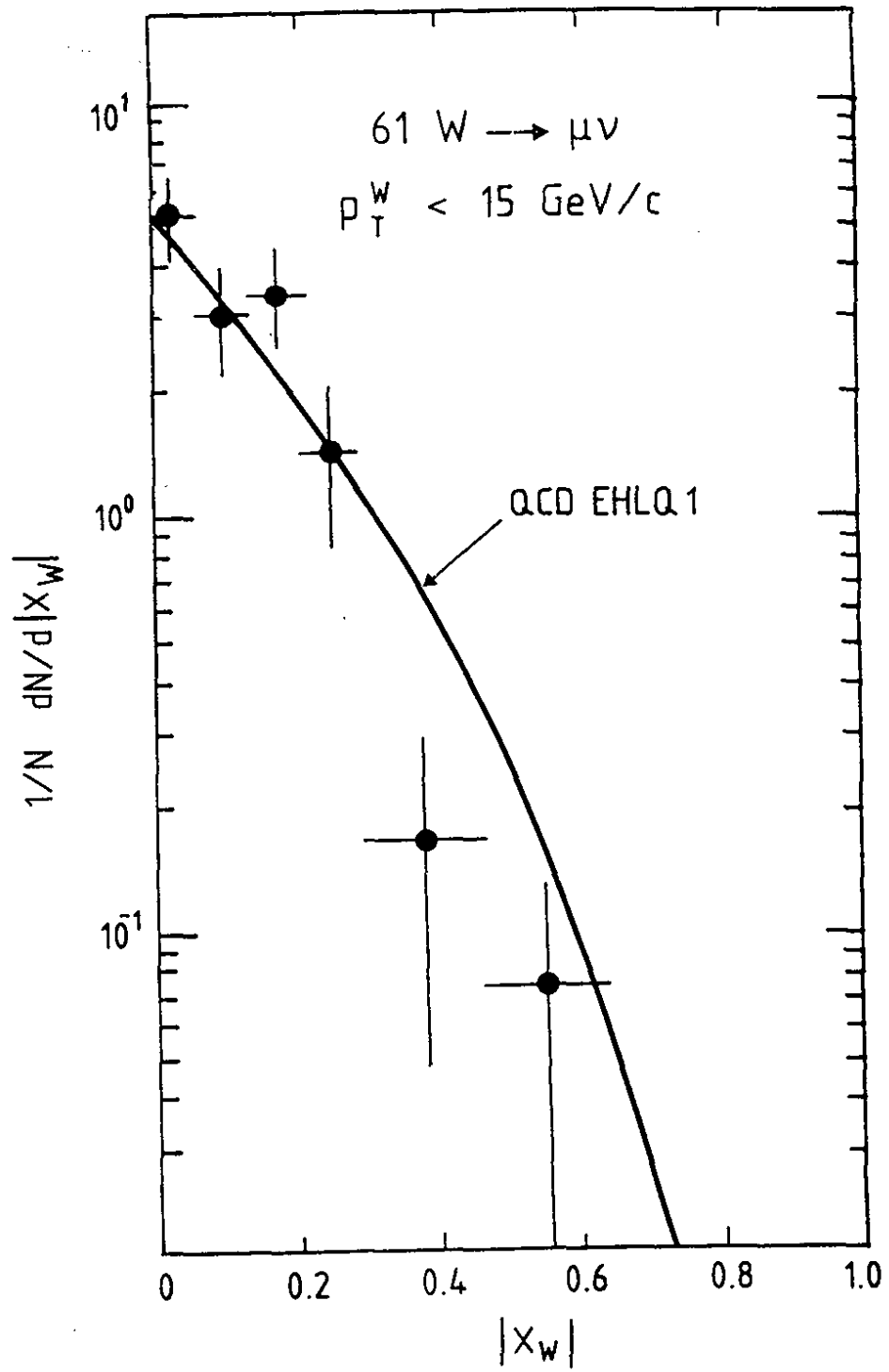
FIG.26.c

FIG.27

FIG.28

correction factor

$Q.x_w$

EHQL1

u(x) = d(x)
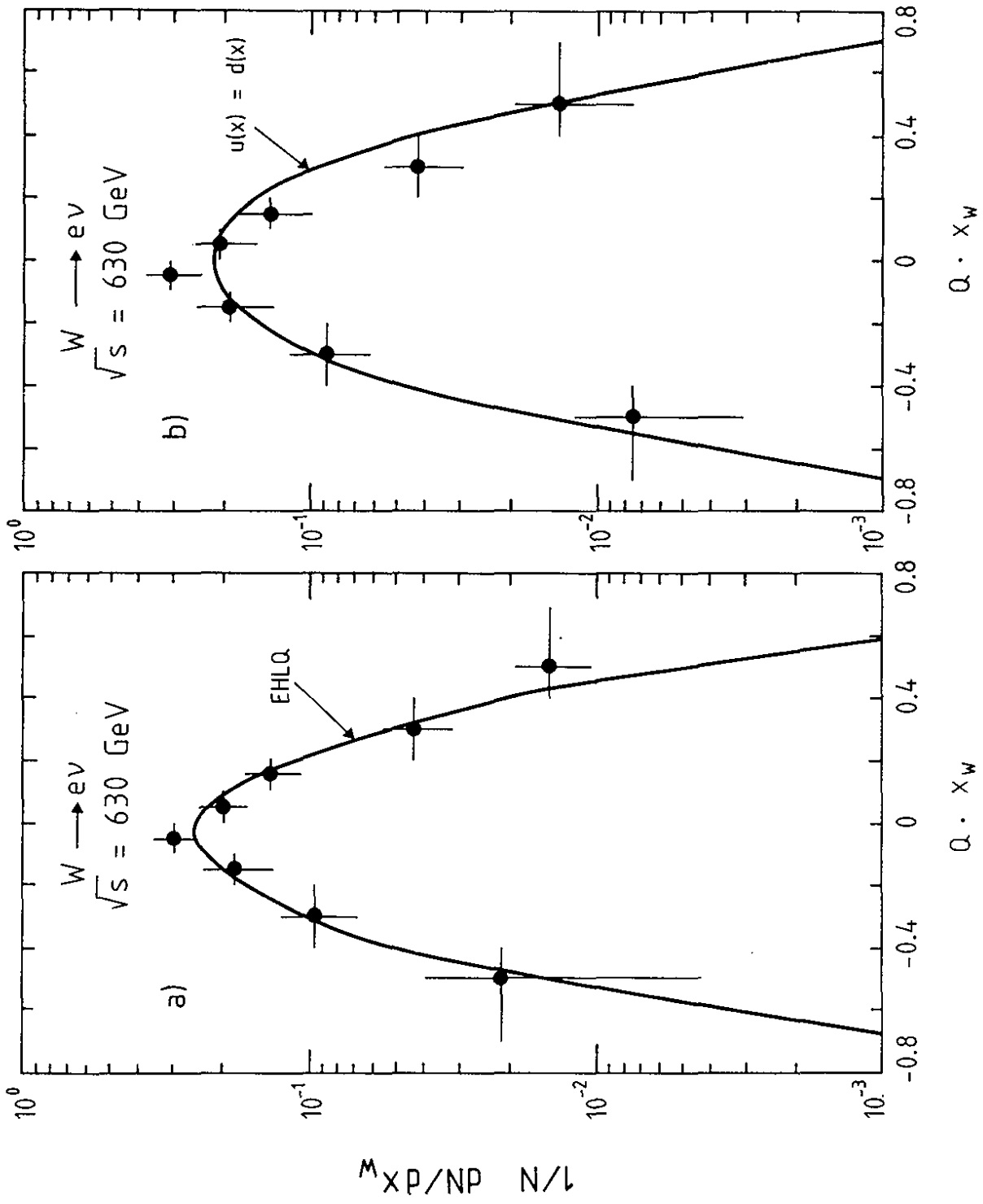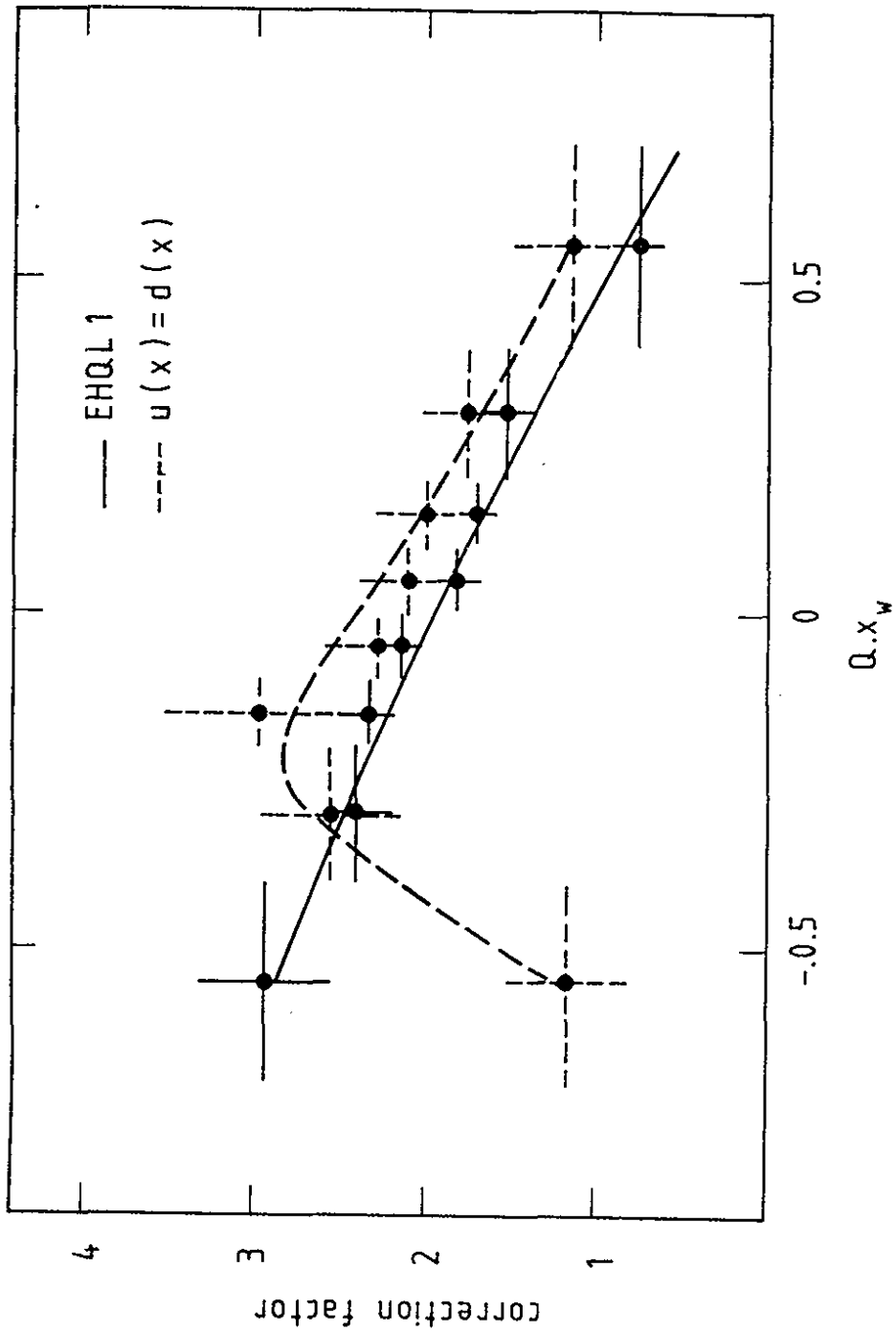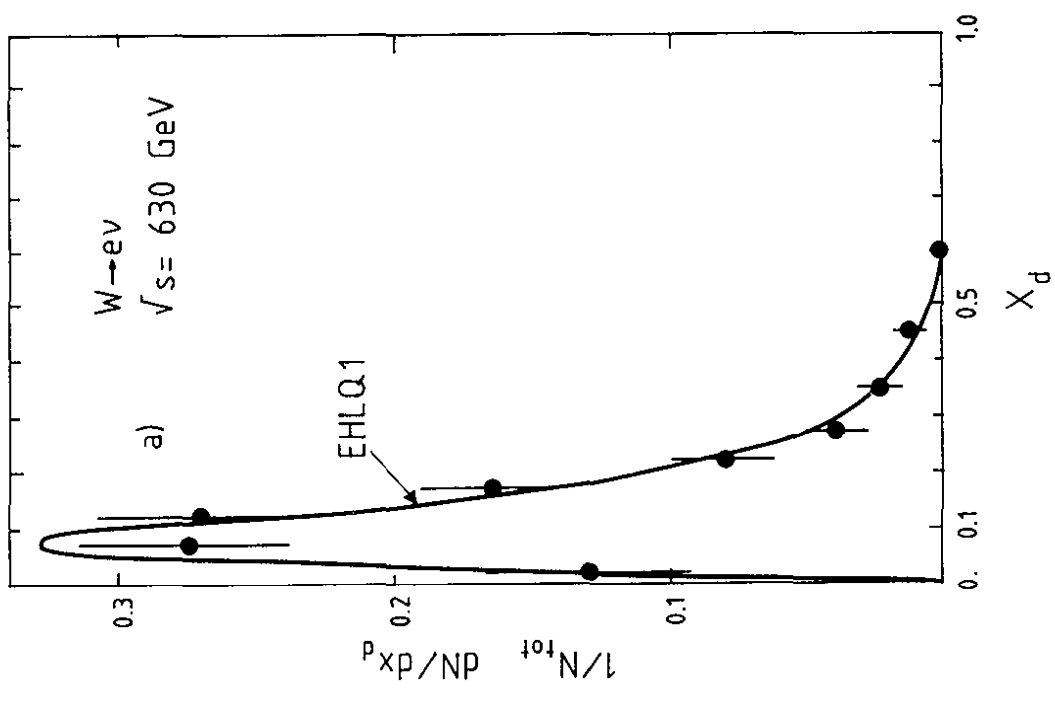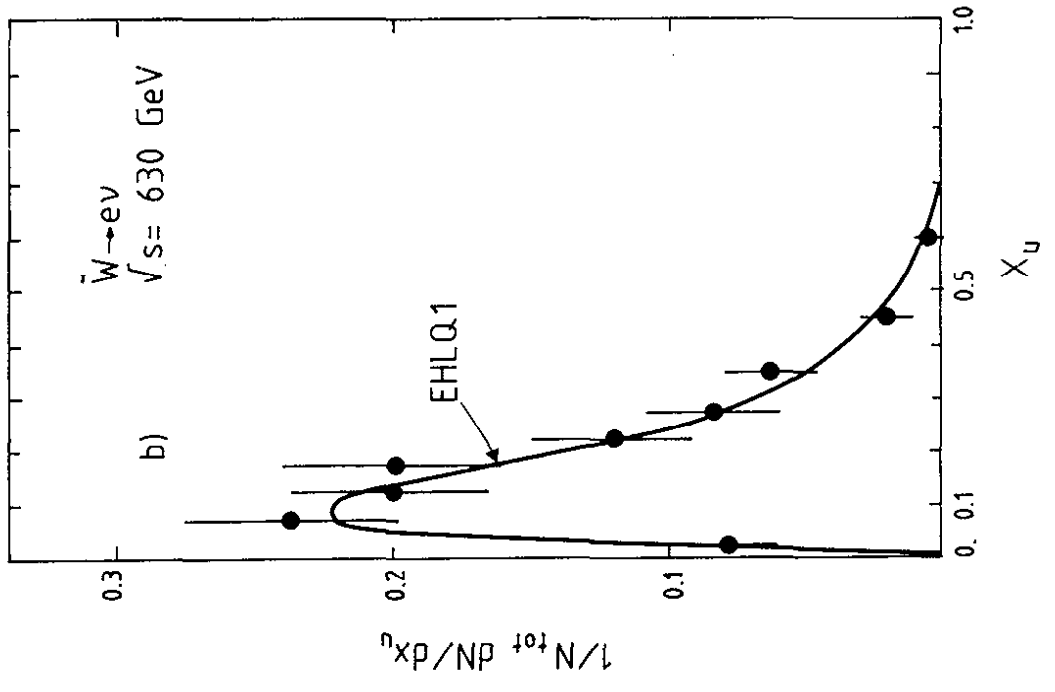
FIG.29
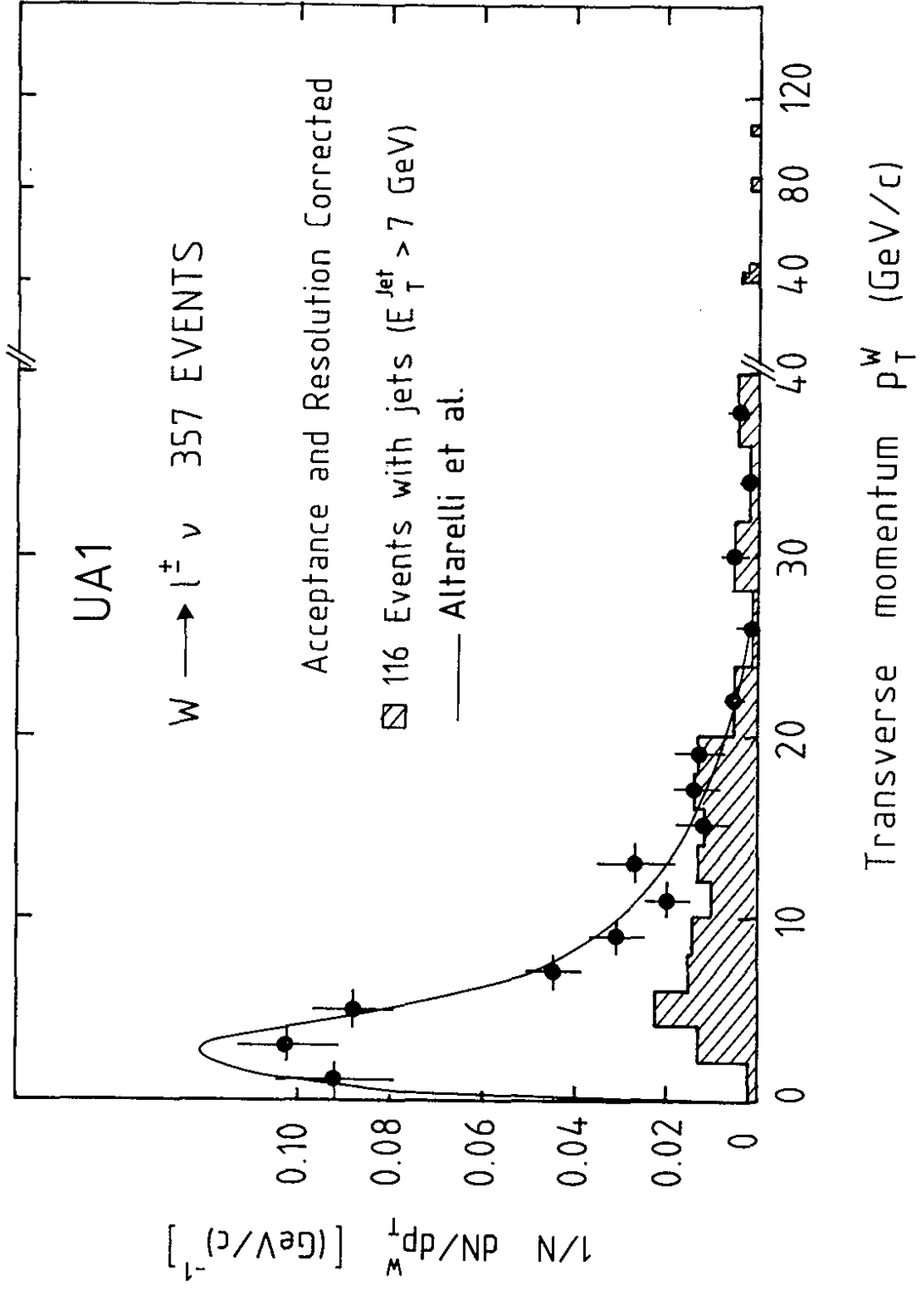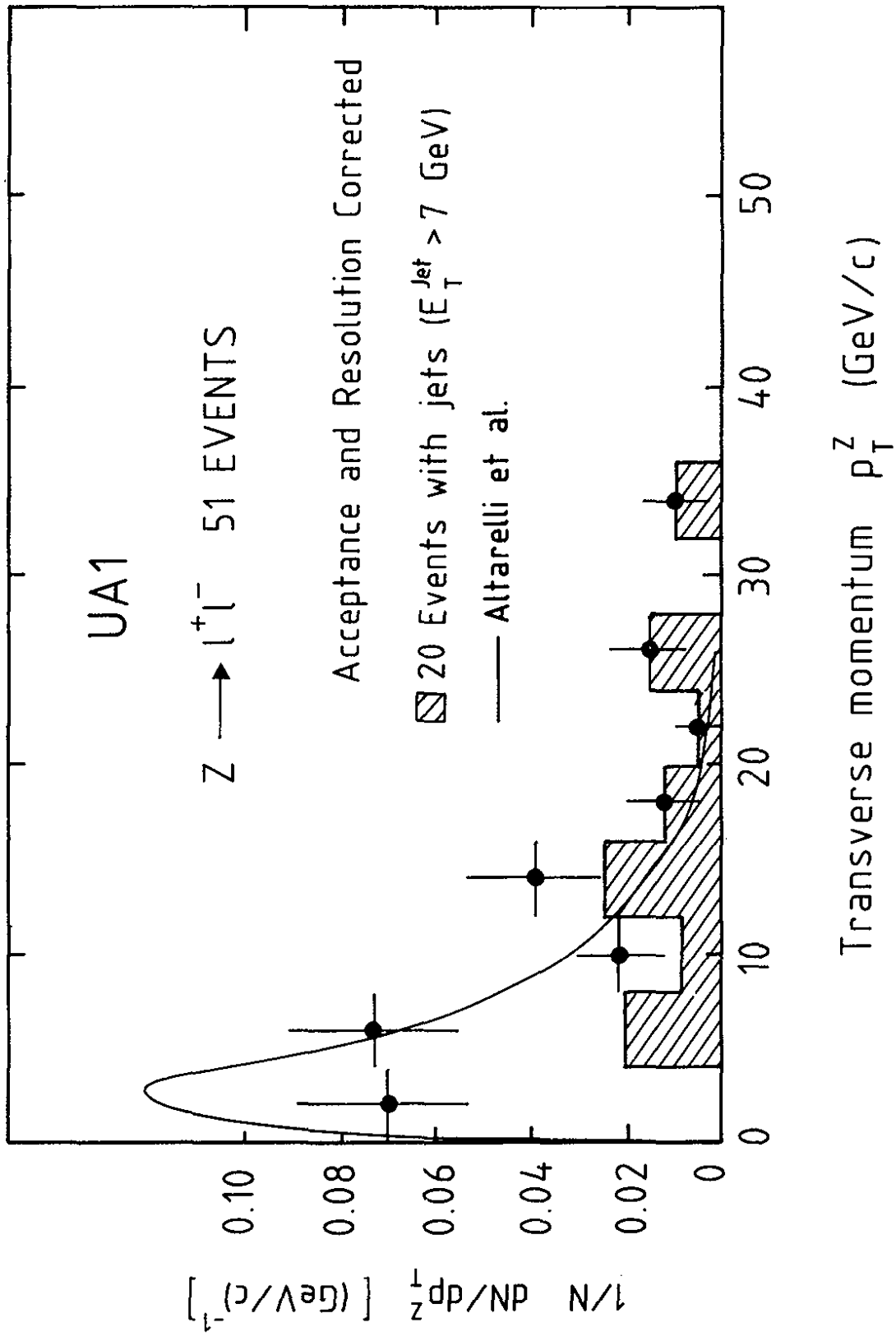
FIG. 30a

FIG. 30b
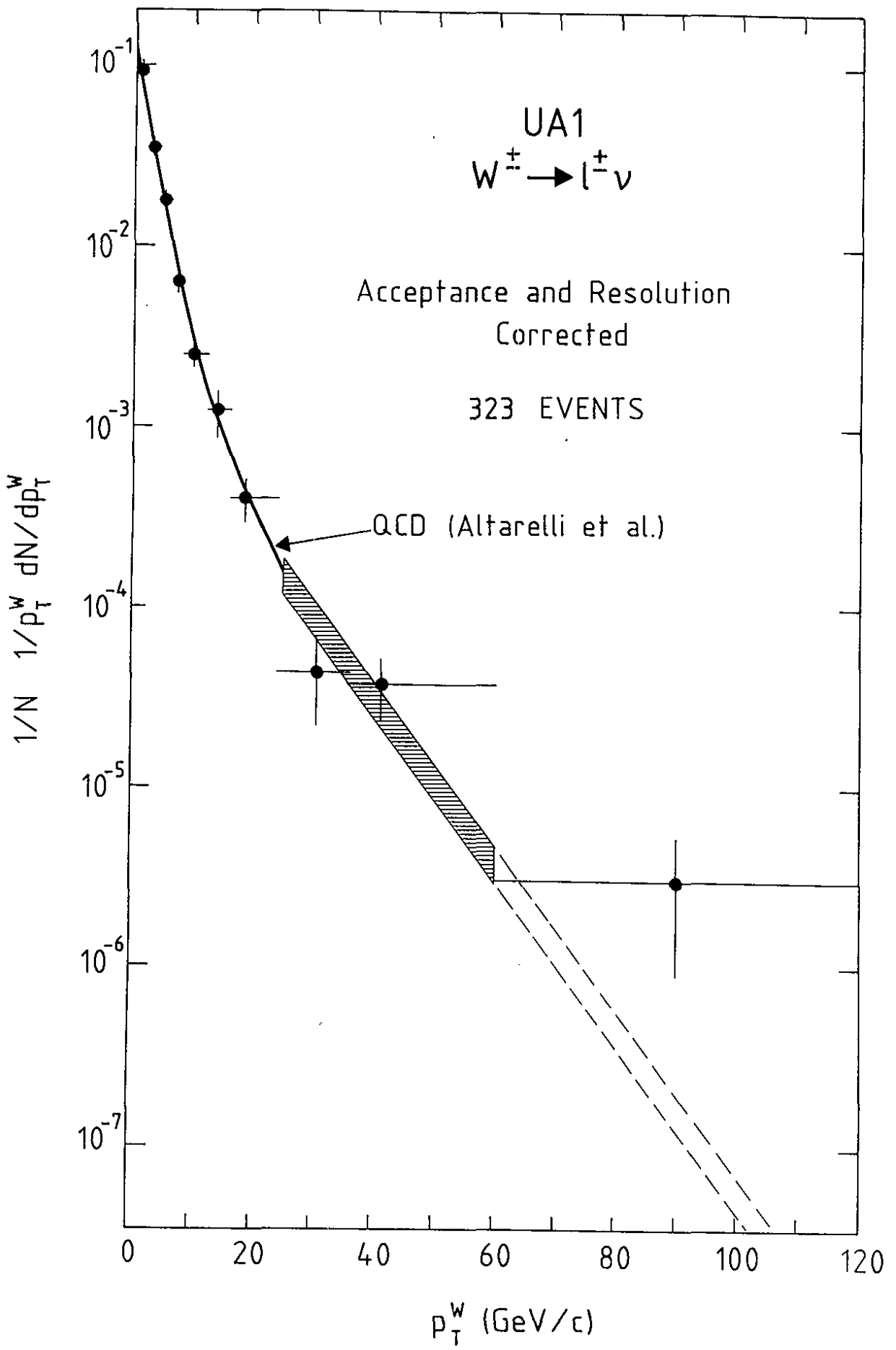
FIG.31
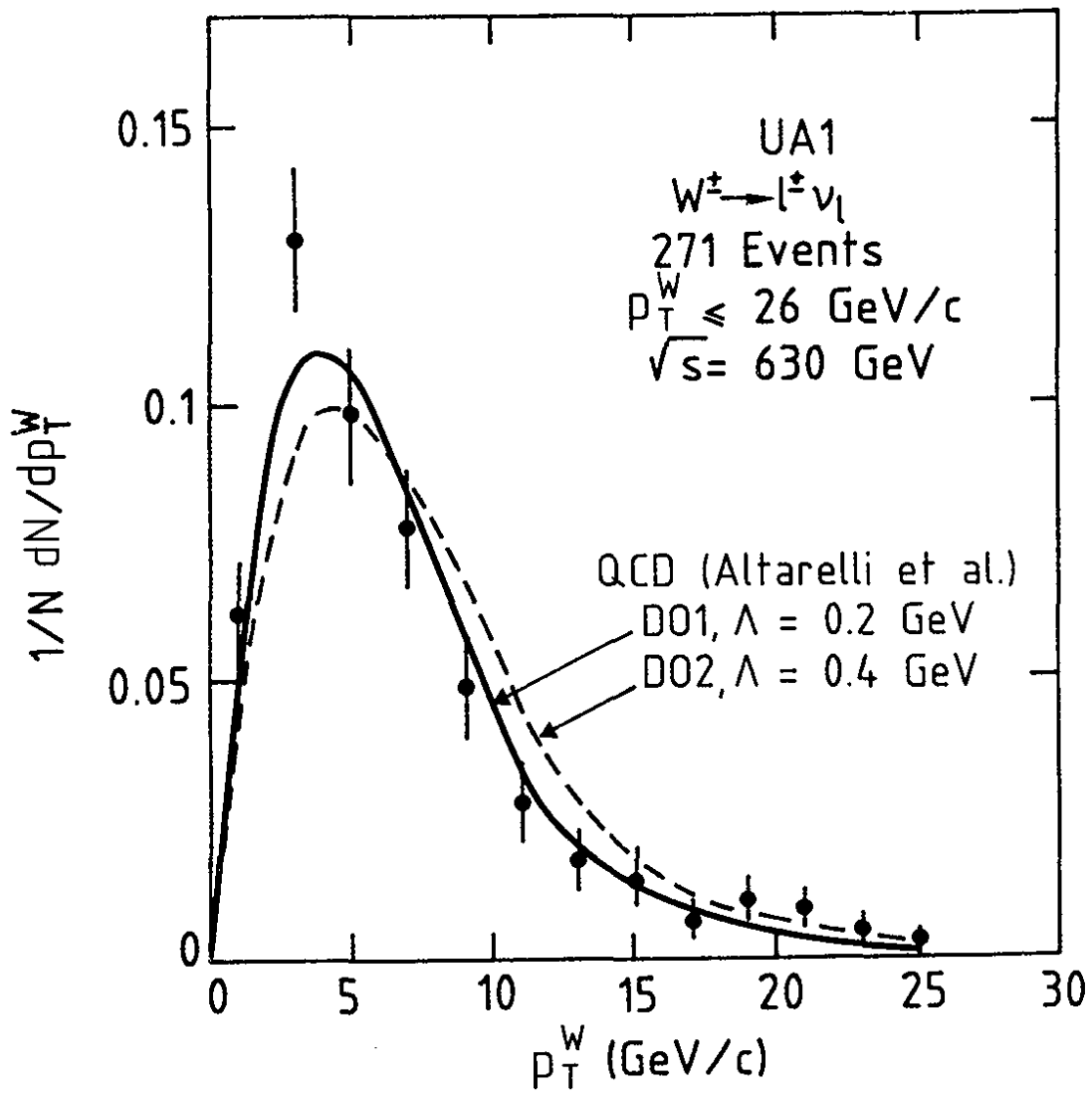
FIG. 32
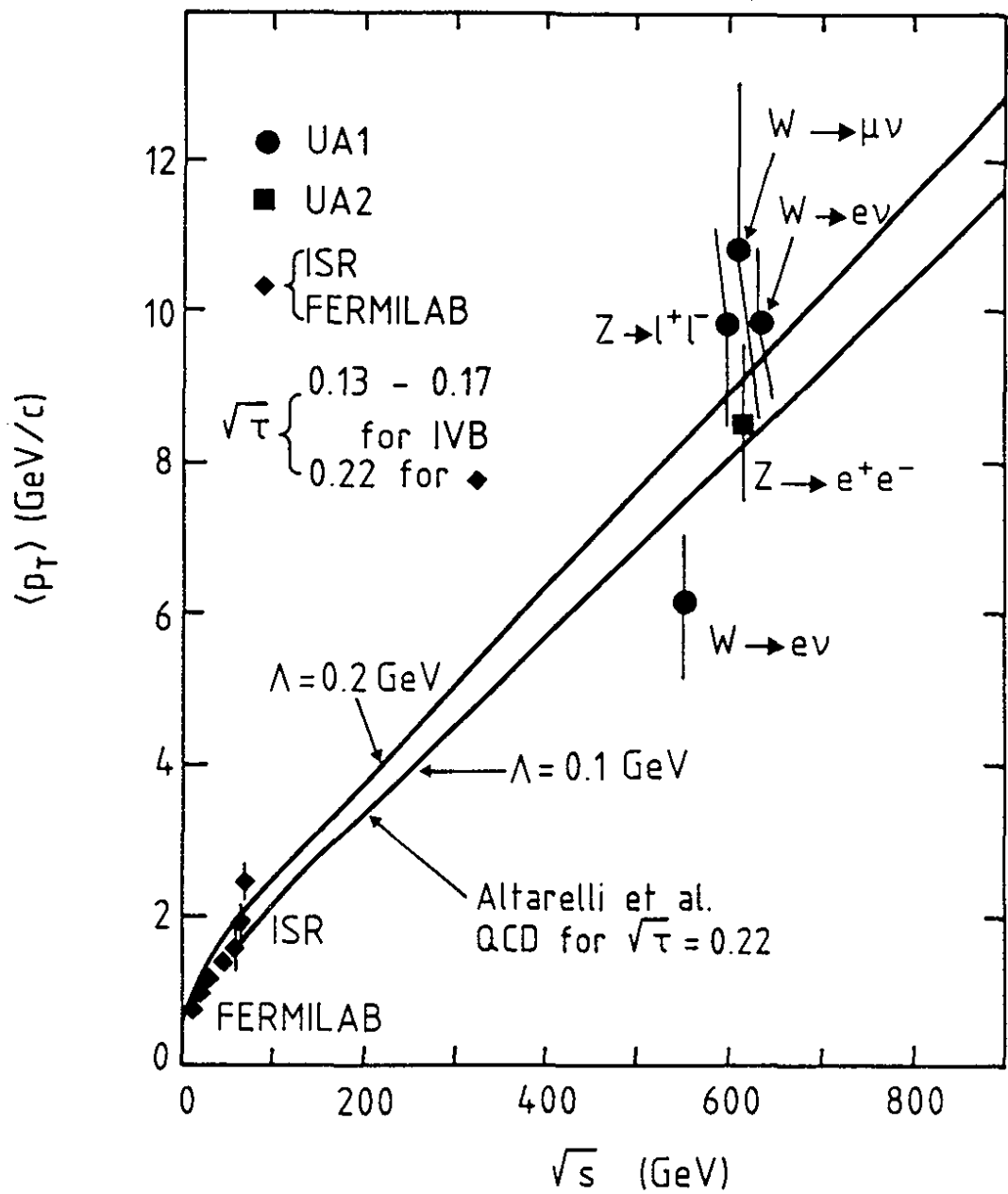
FIG.33
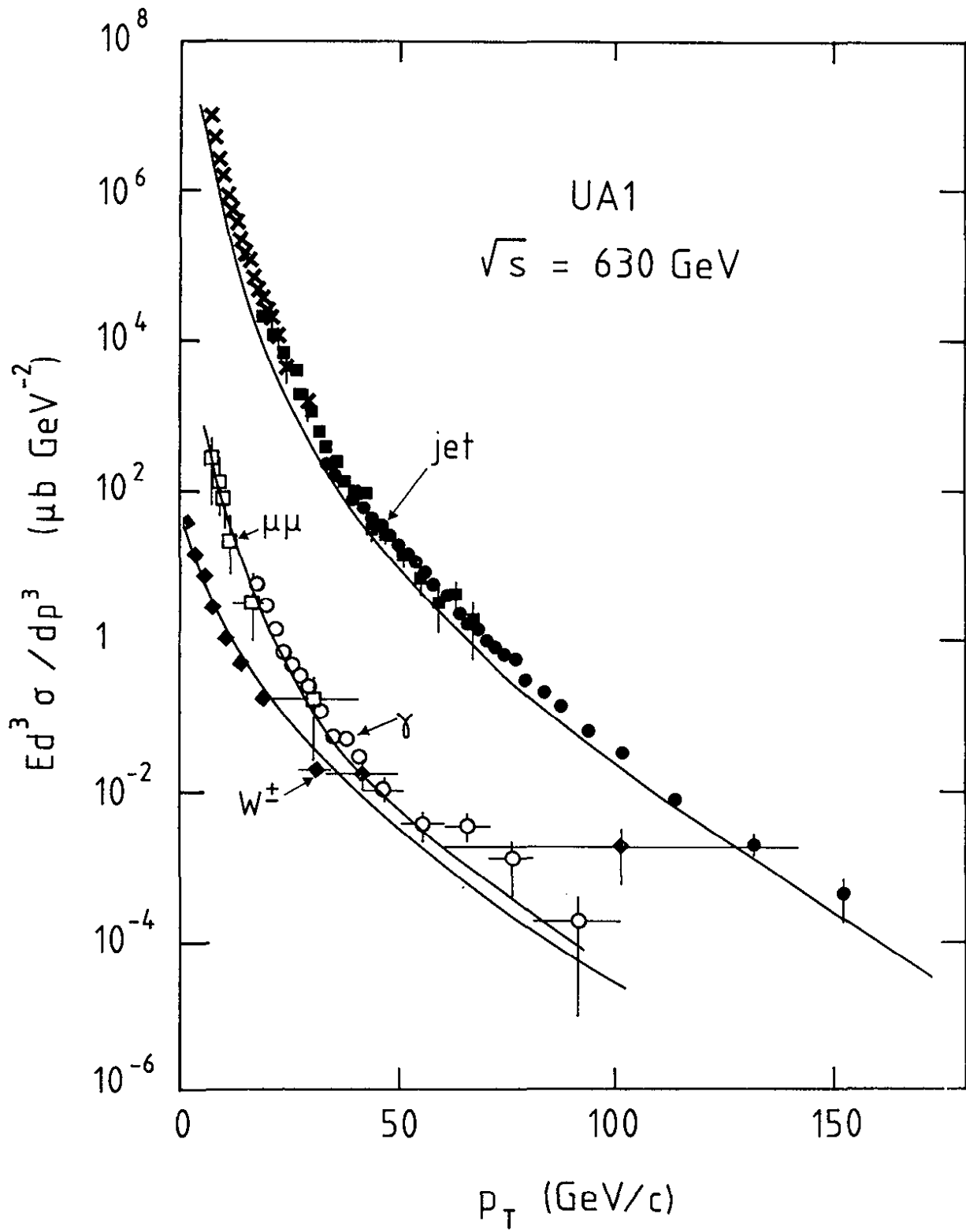
FIG. 34
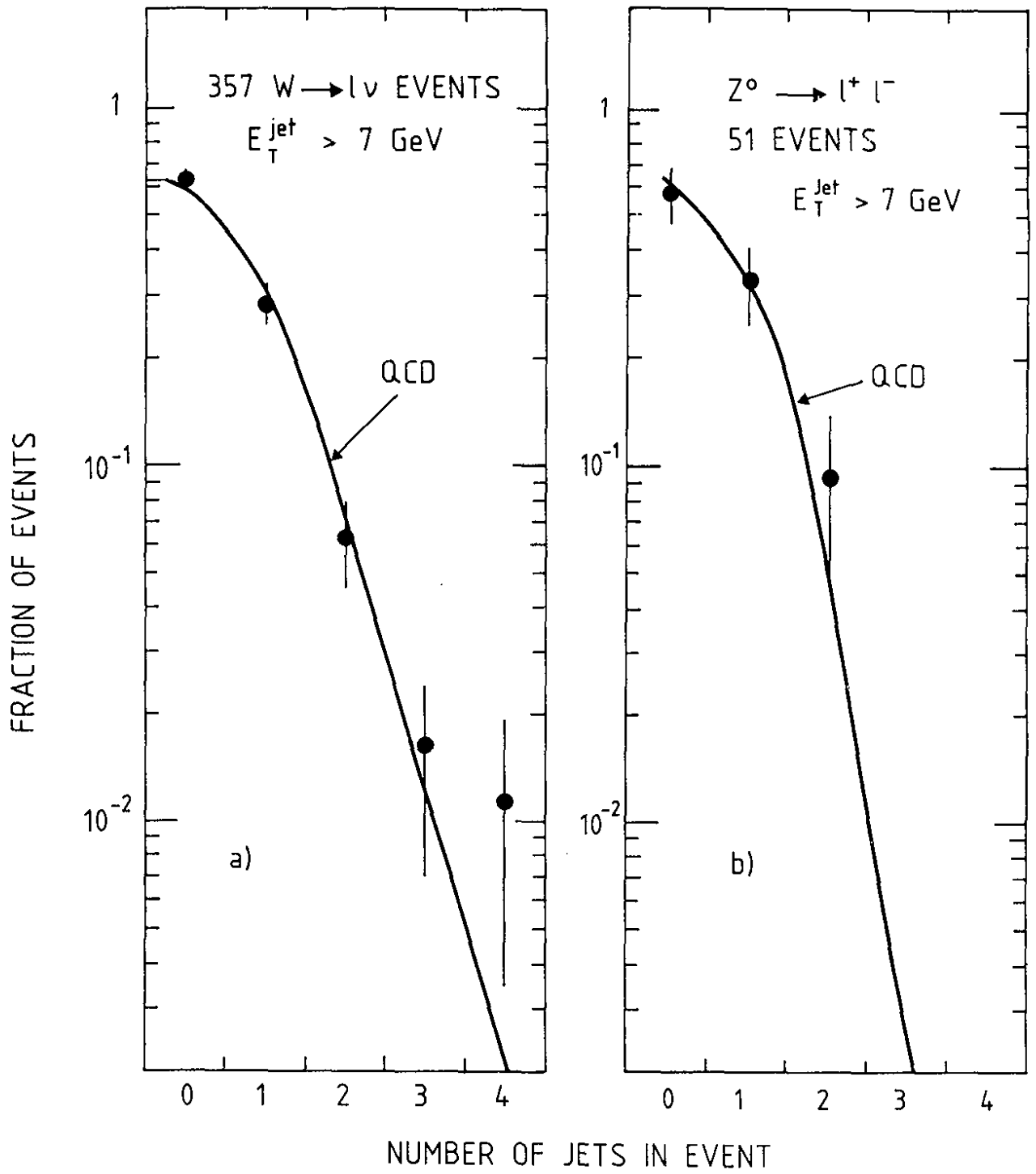
FIG.35
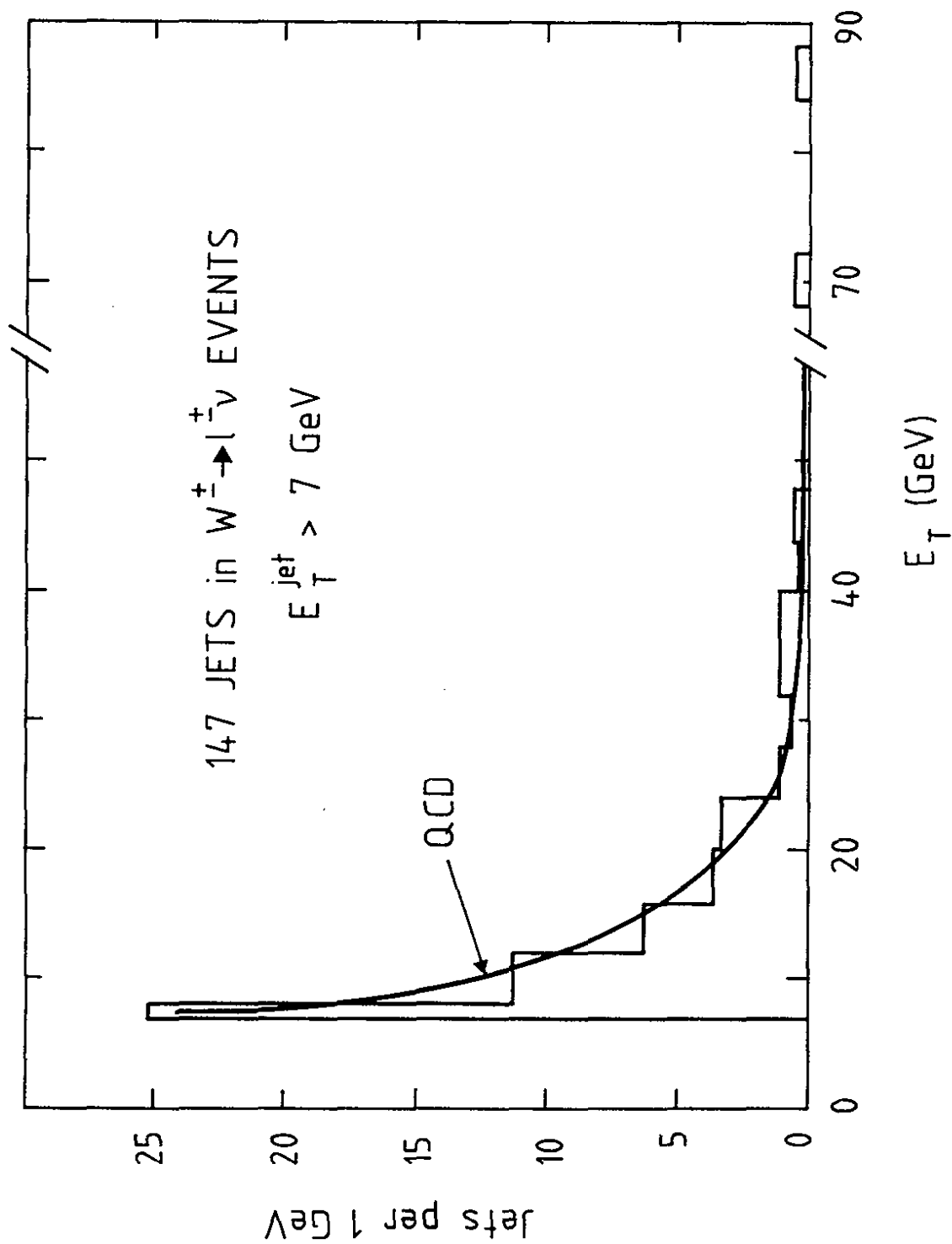
FIG.36
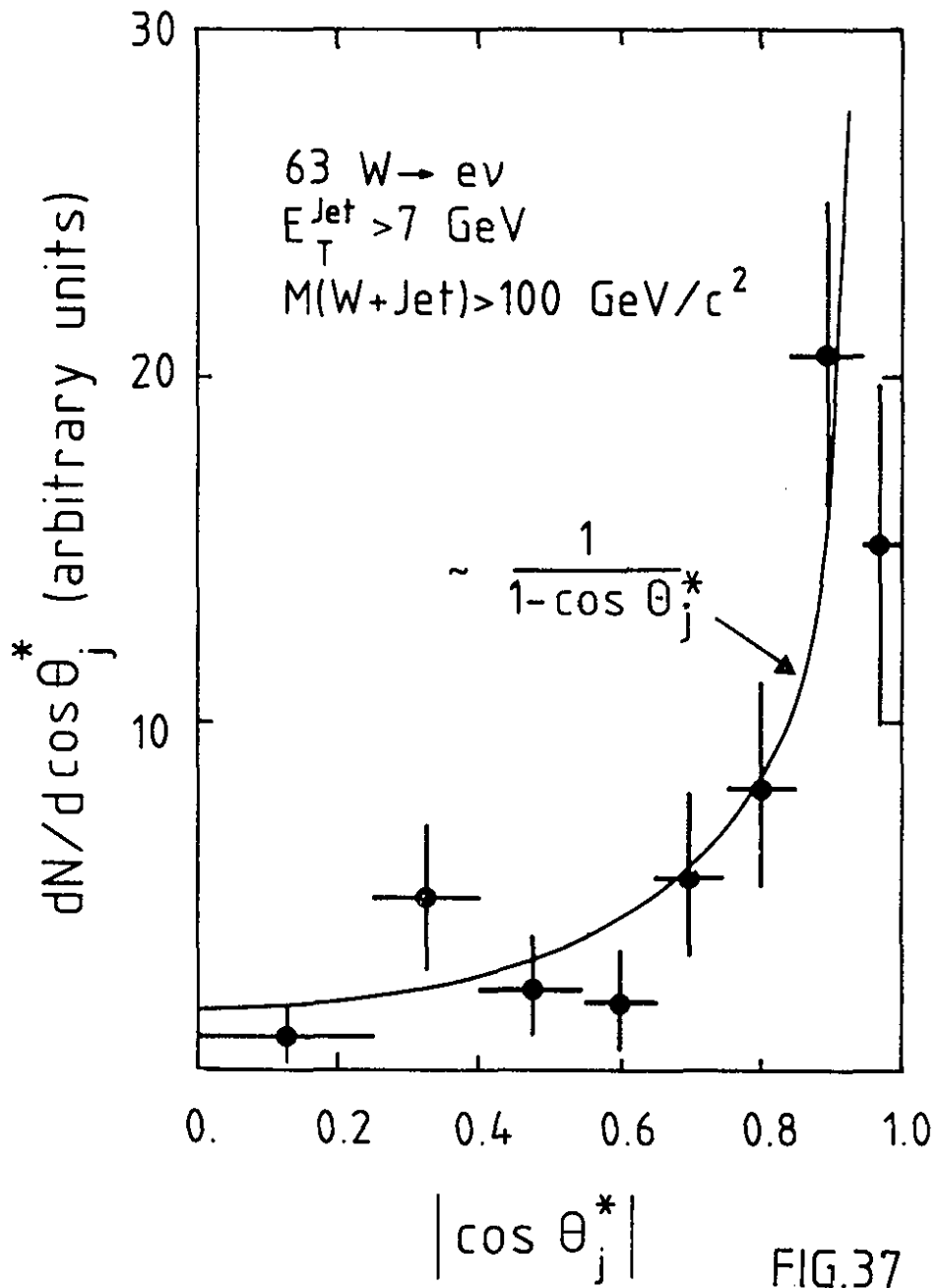
FIG.37
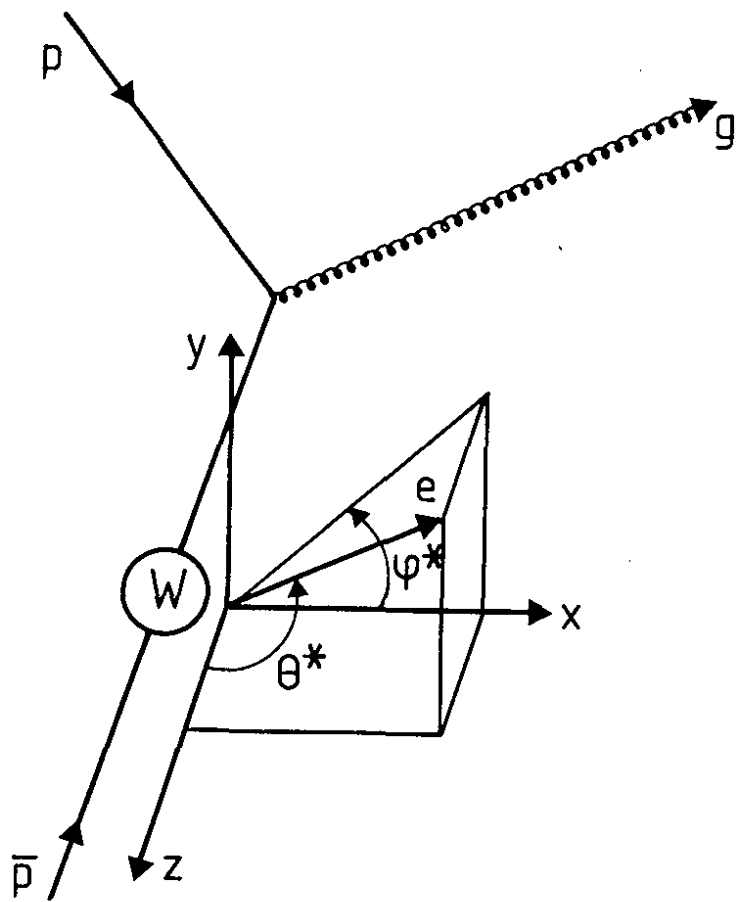
FIG.38
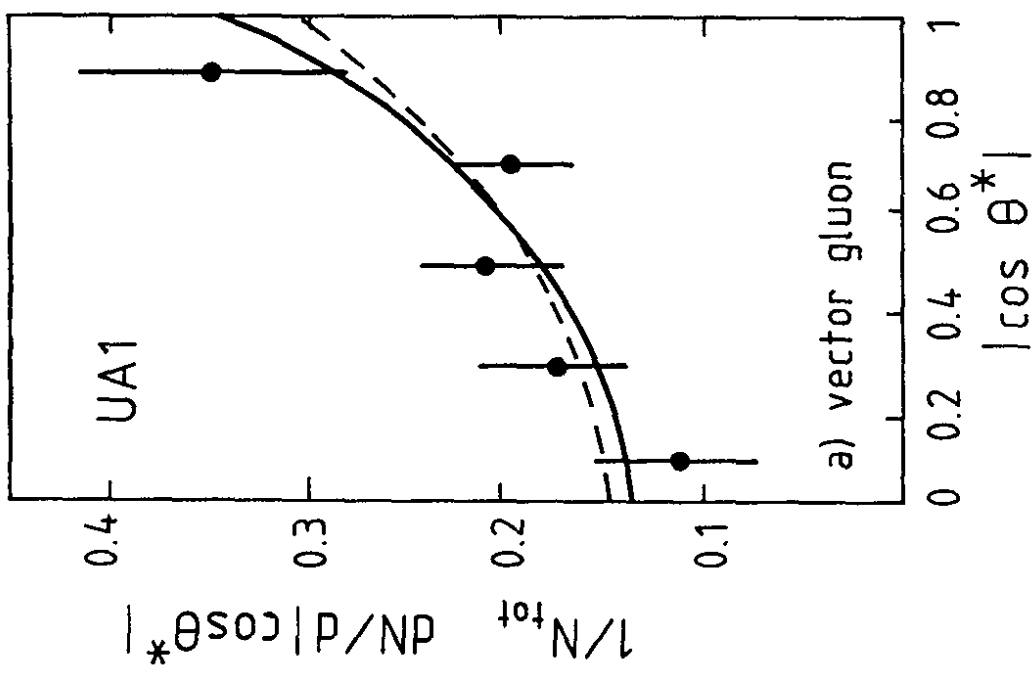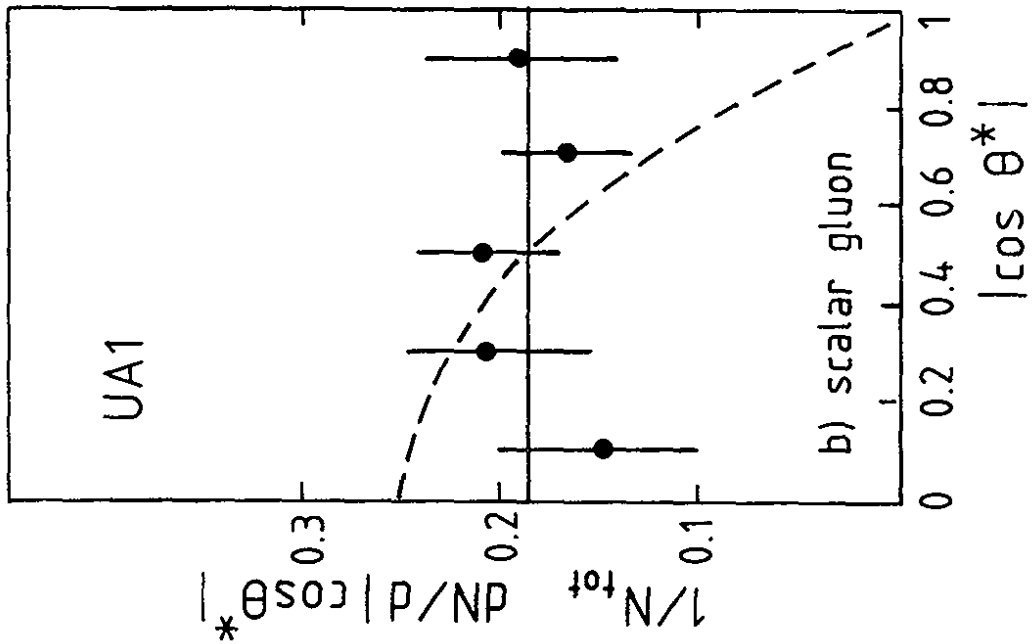
FIG.39
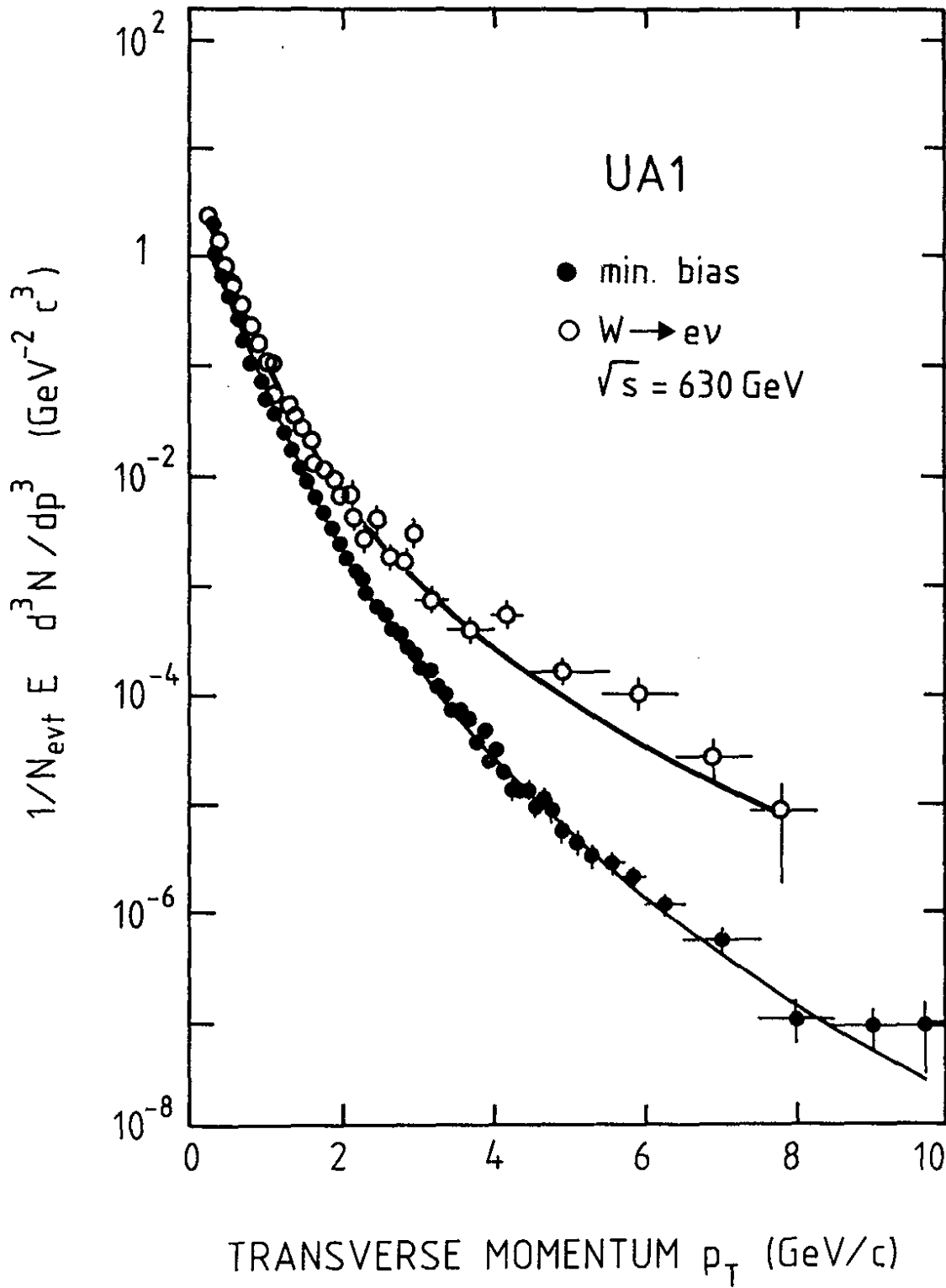
FIG.40
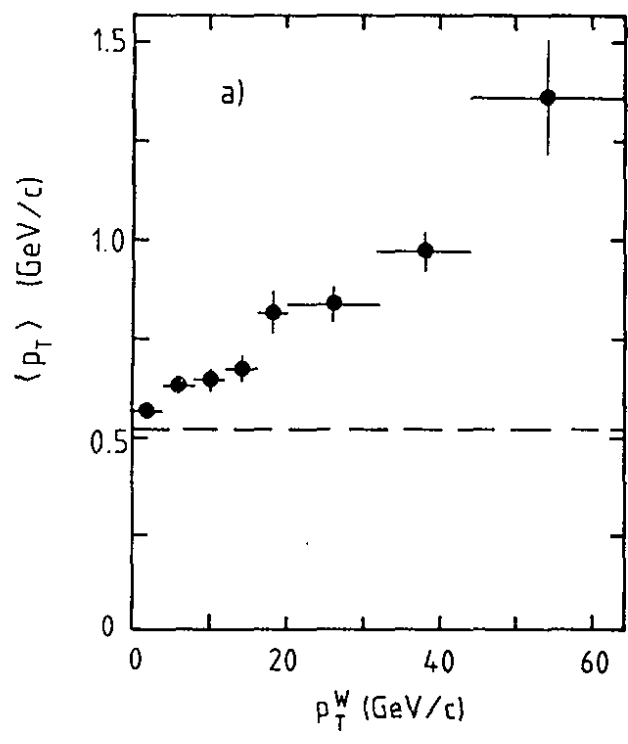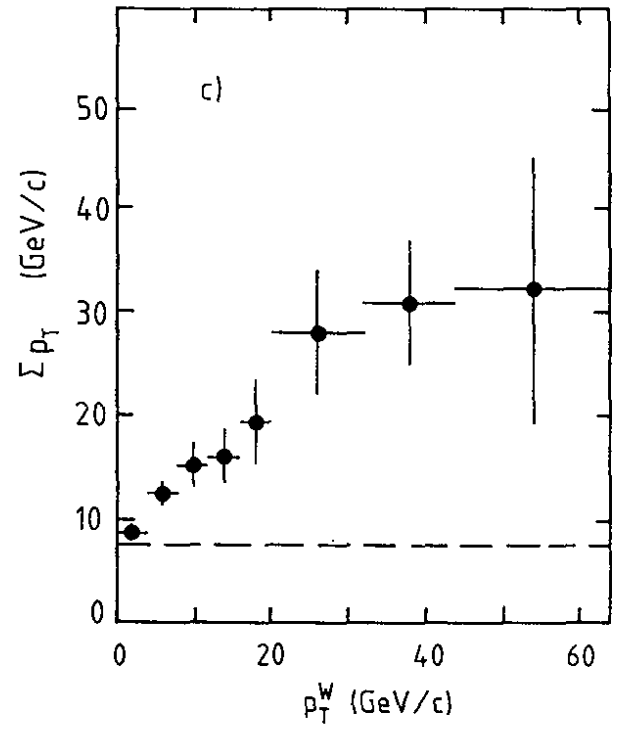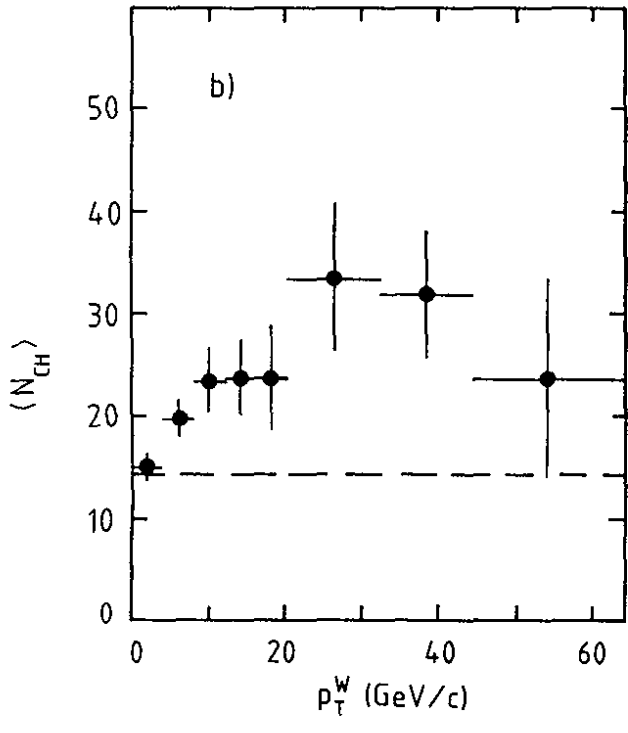
FIG.41
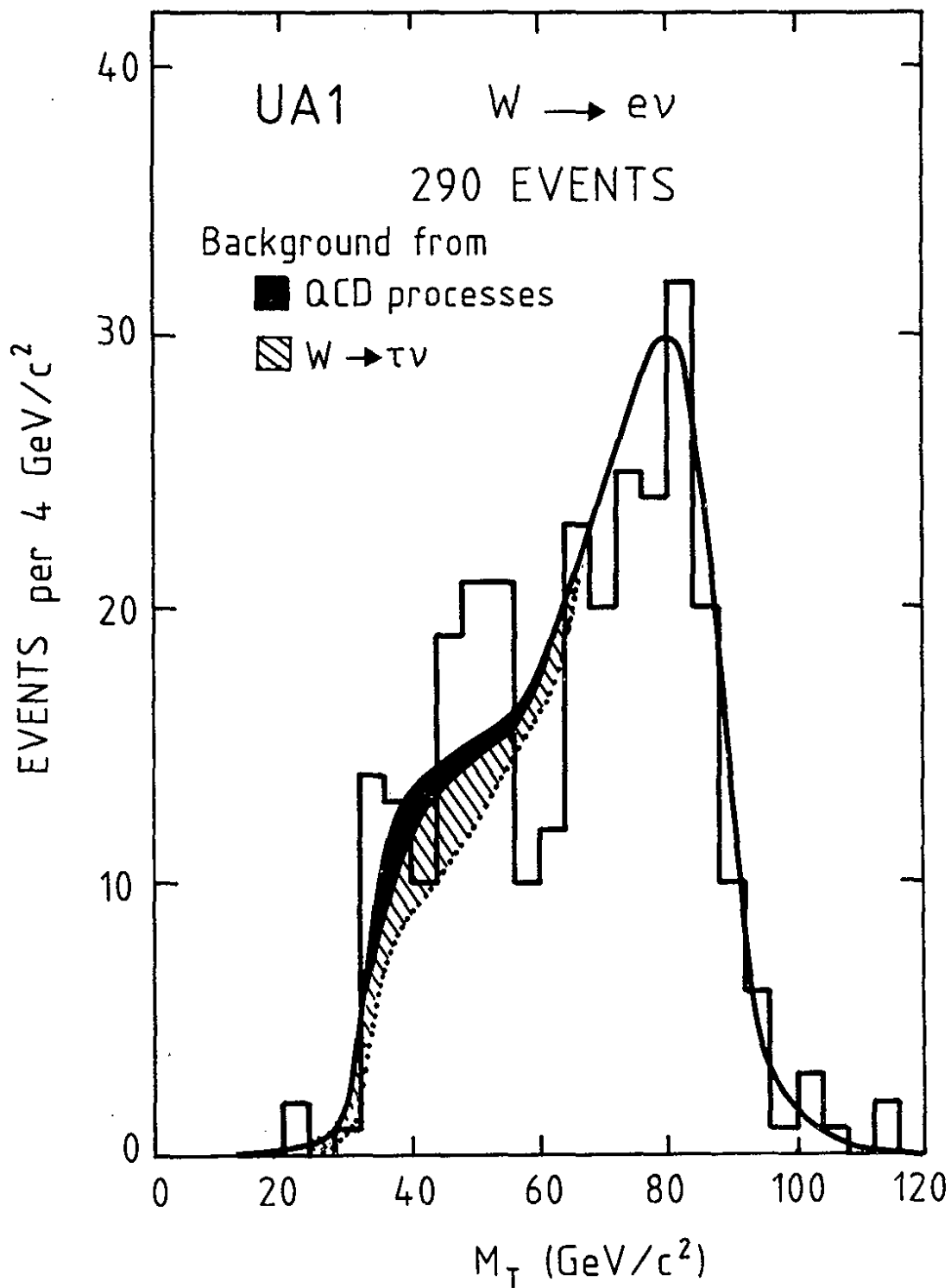
FIG.42
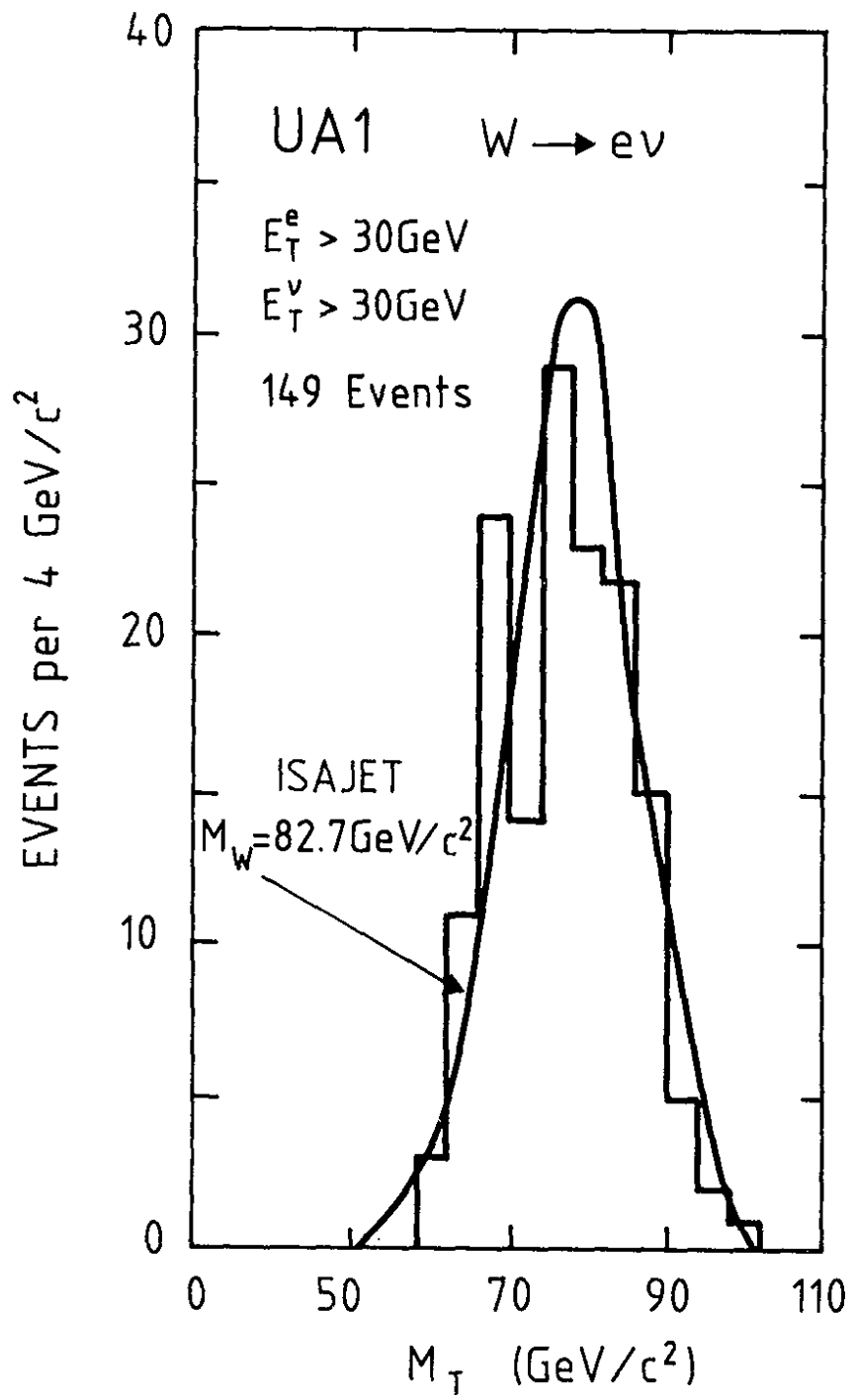
FIG.43
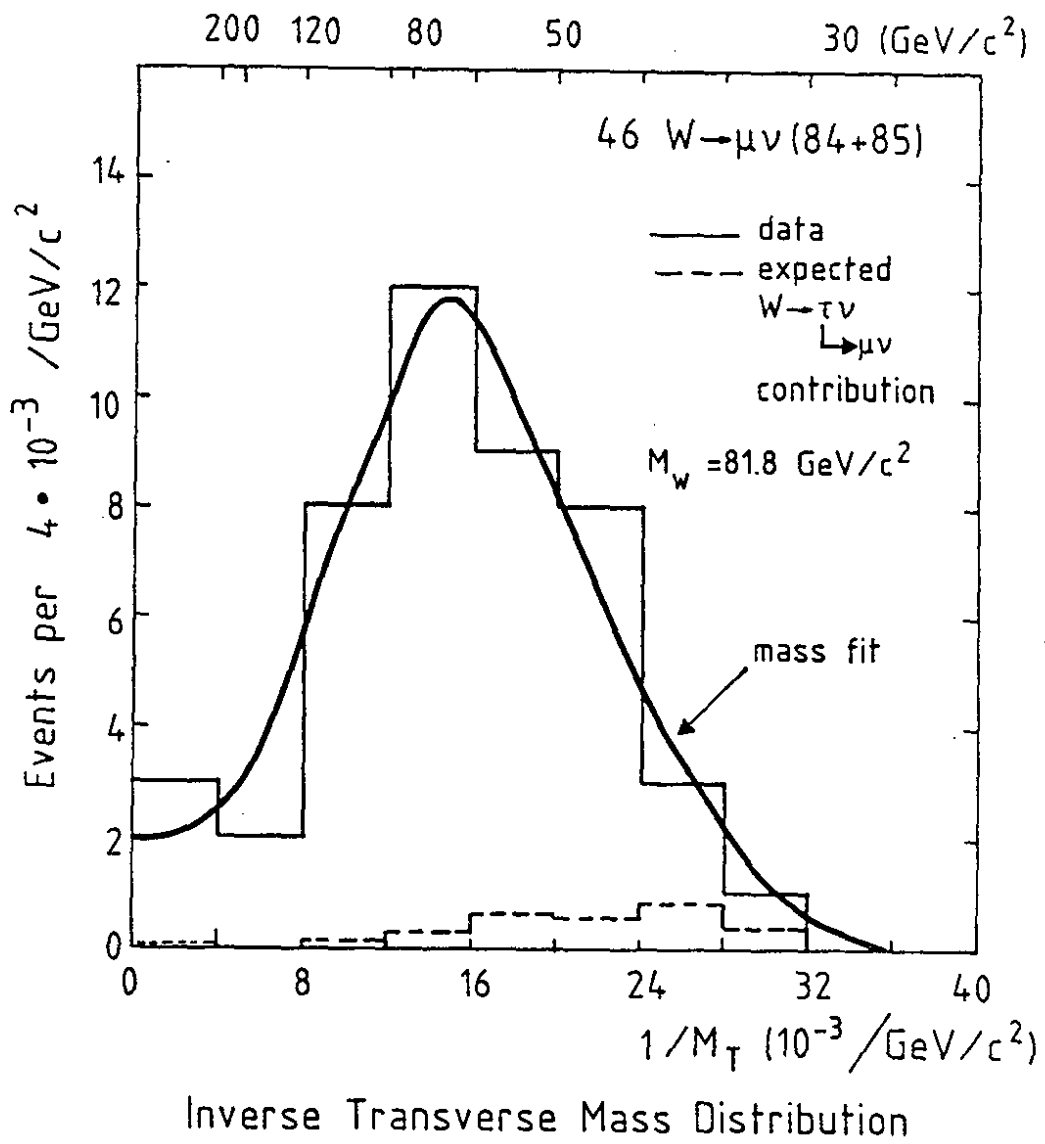
FIG.44
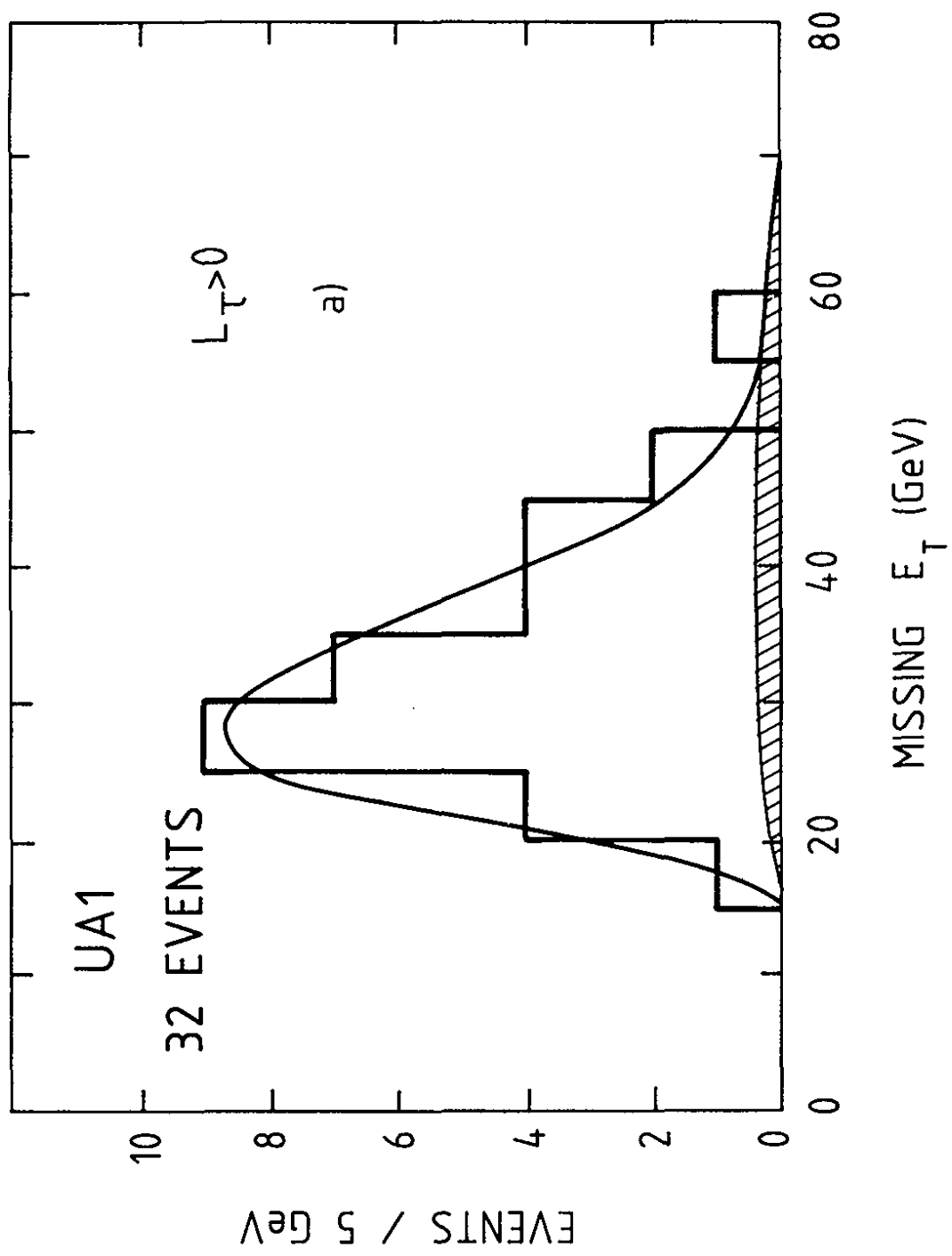
FIG.45
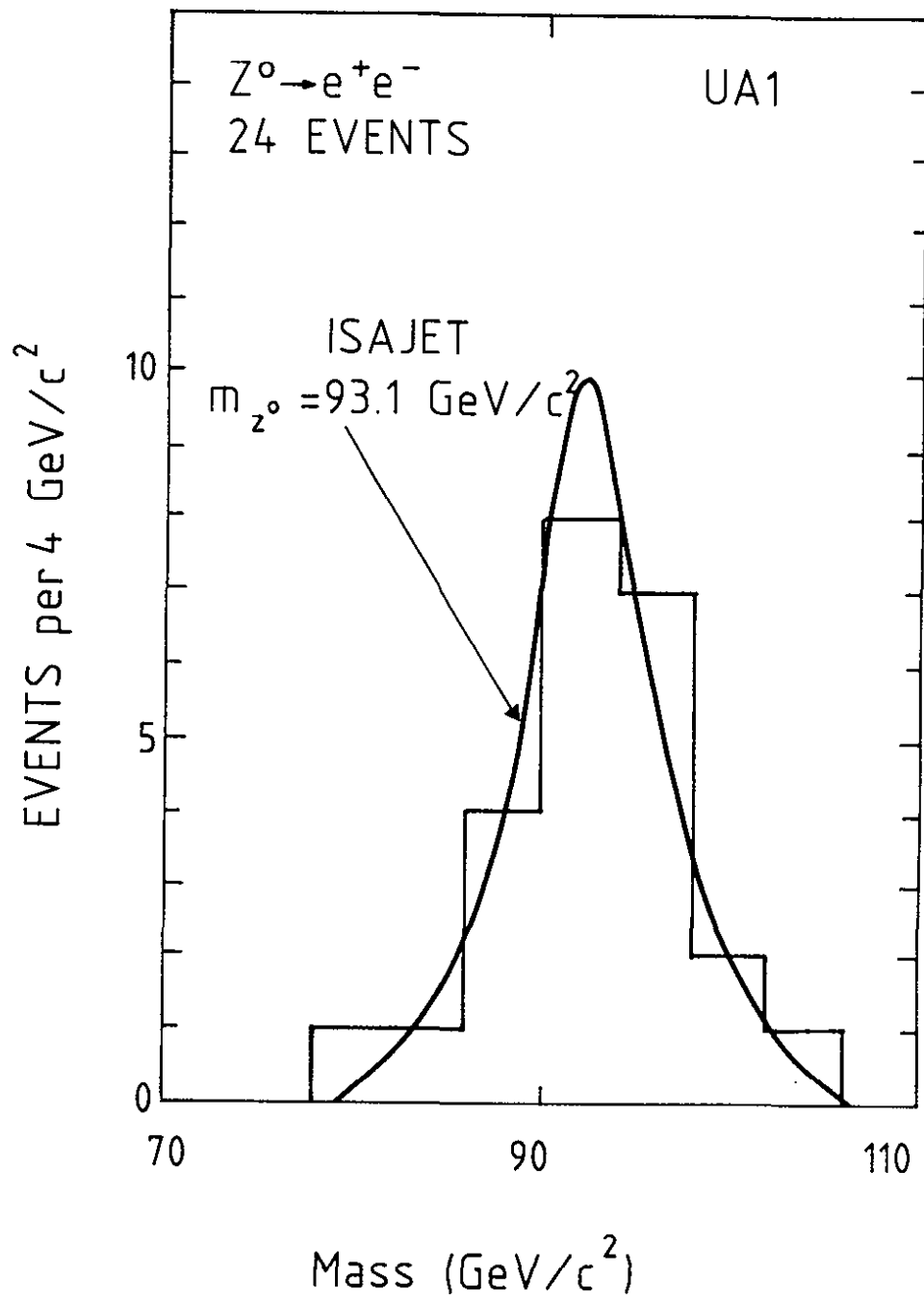
FIG.46
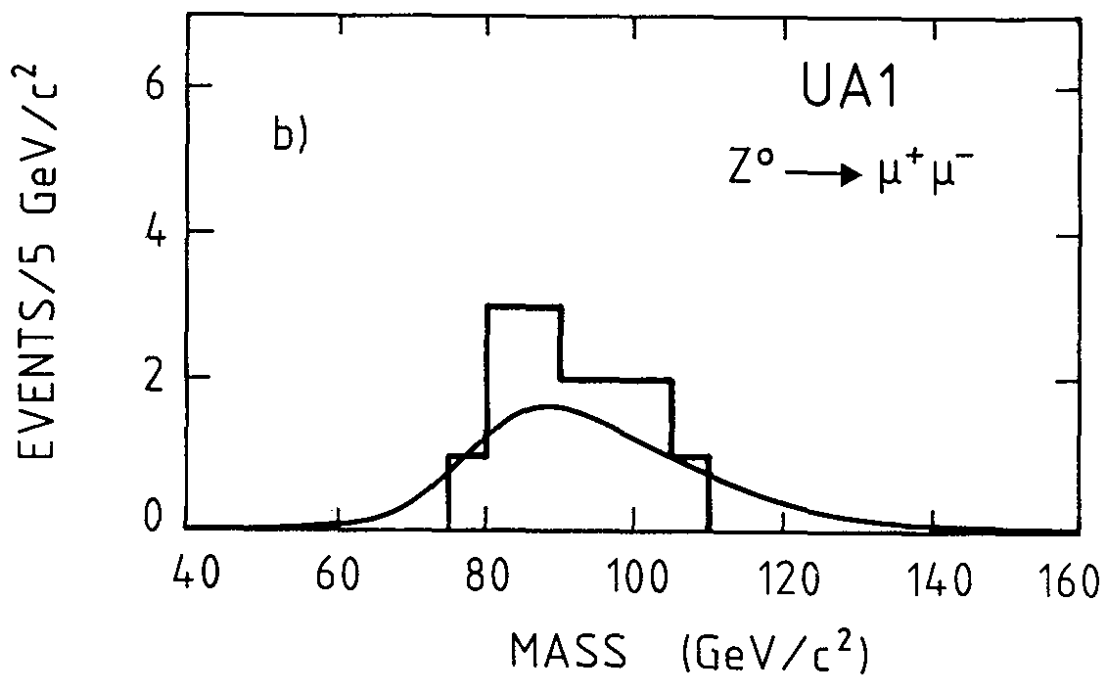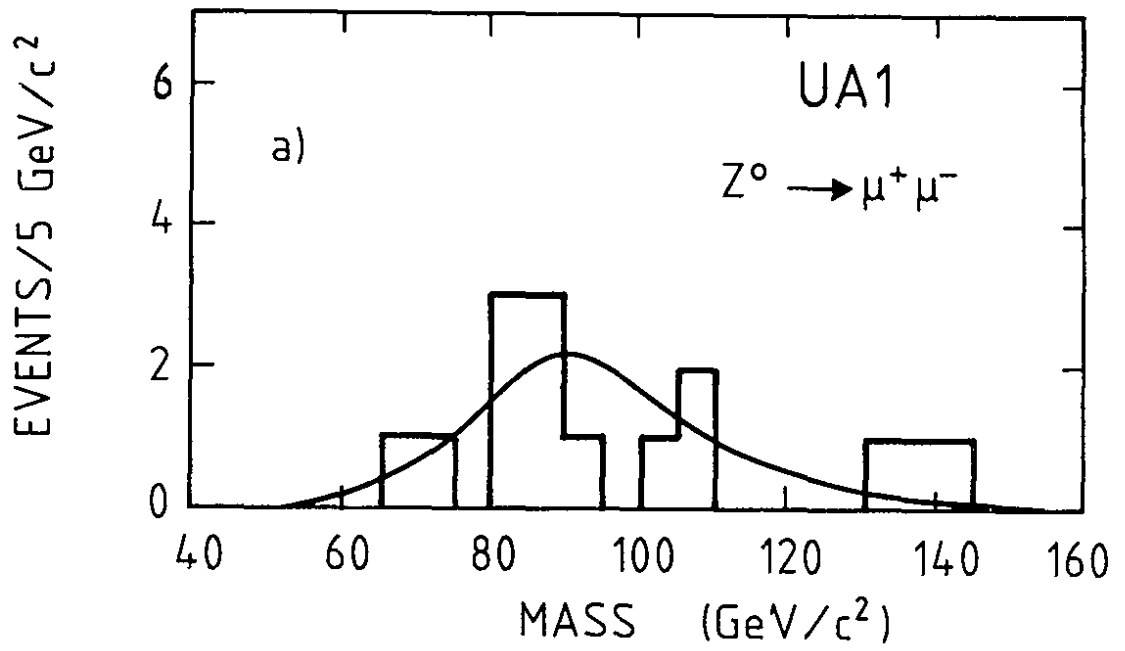
FIG.47
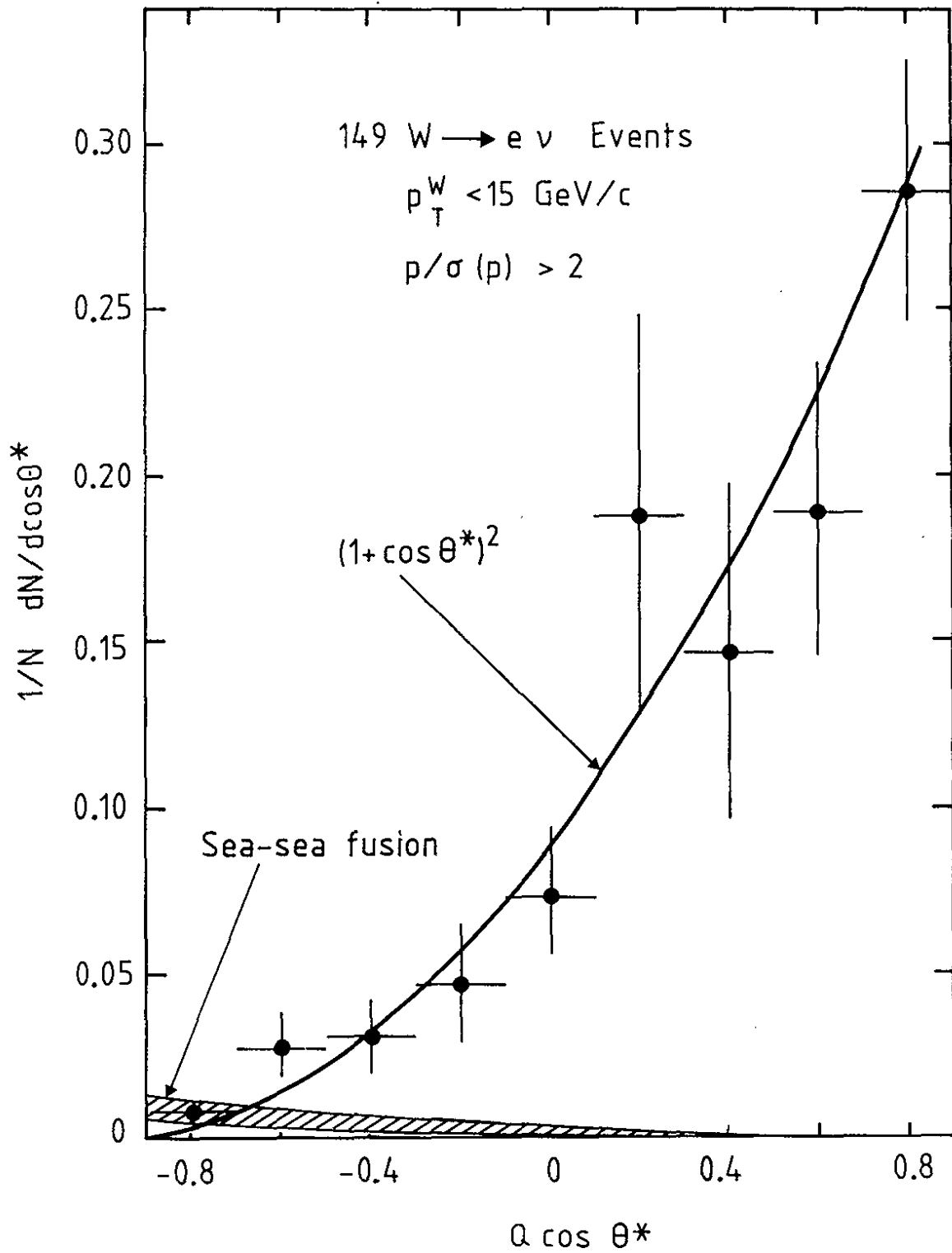
FIG. 48
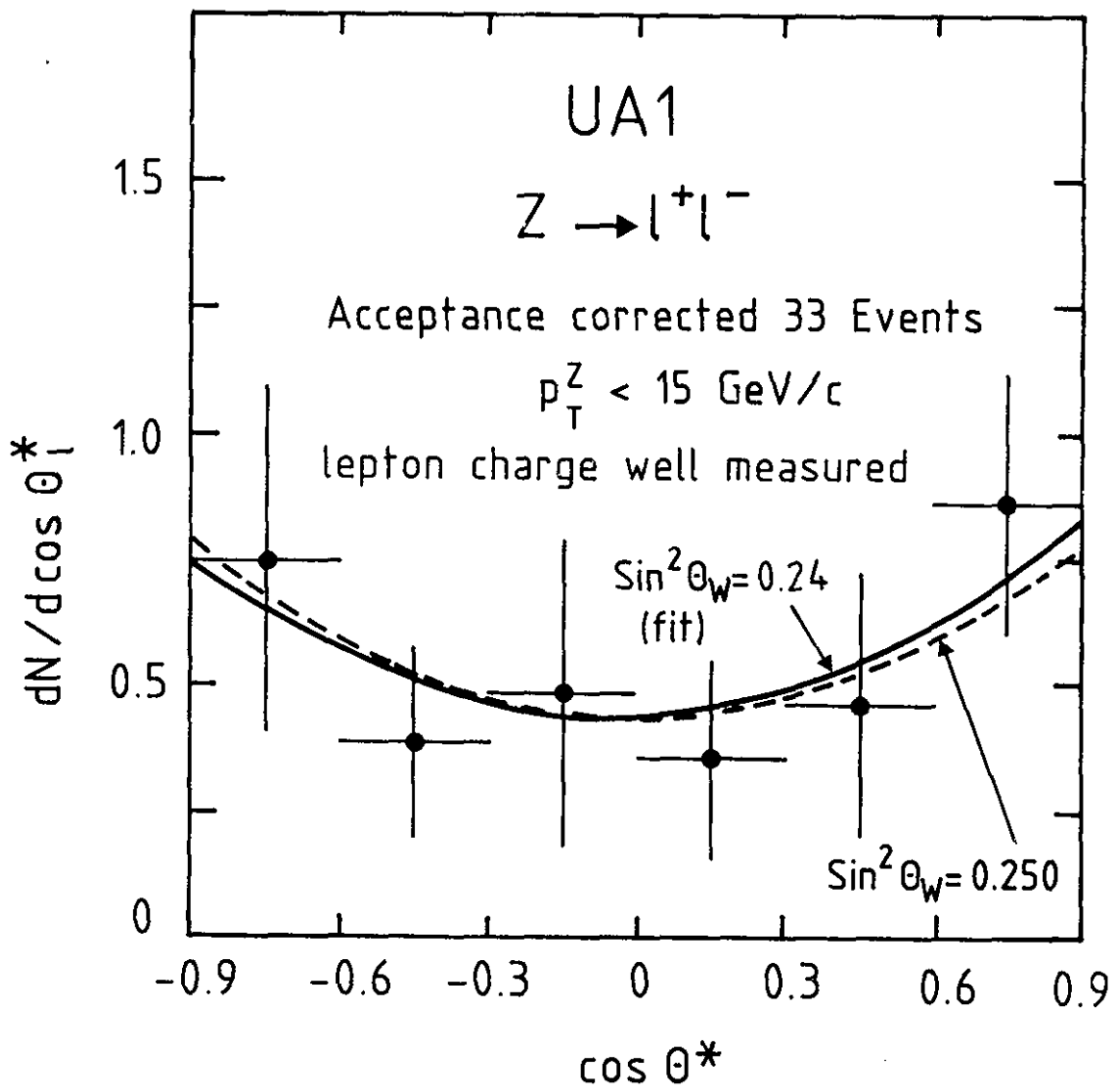
FIG.49
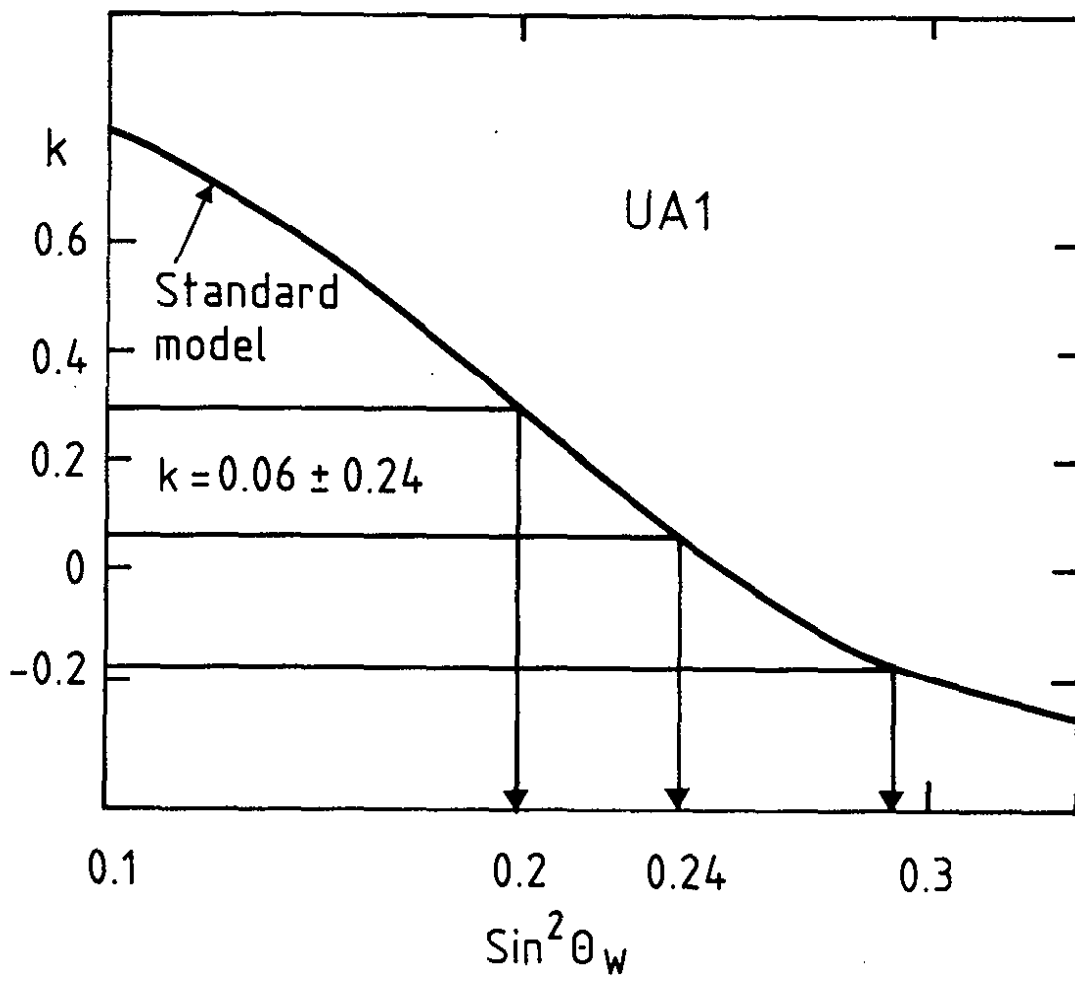
FIG.50
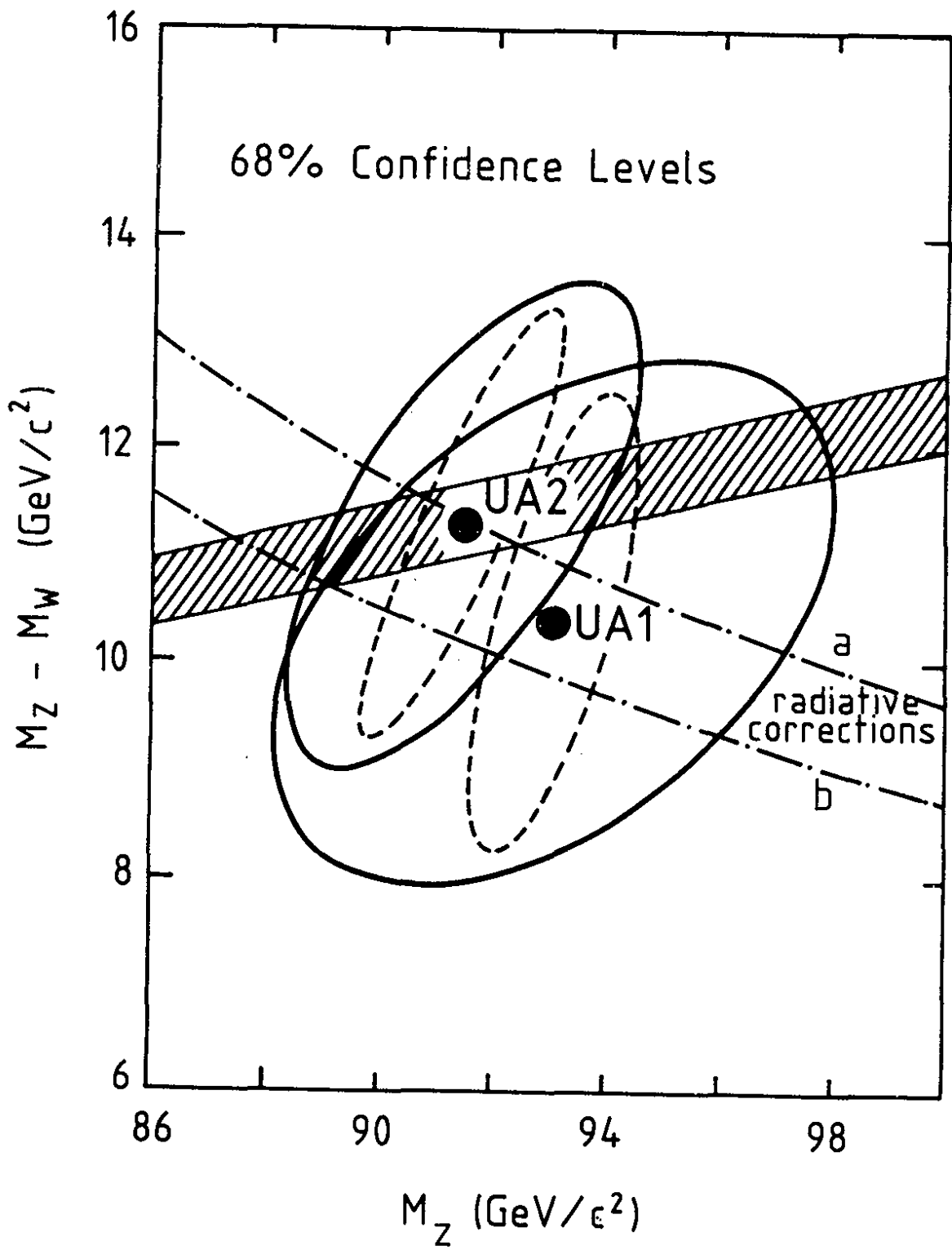
FIG.51

FIG.52

FIG.53

FIG.54

FIG.55

81 W → eν events

W + 1 Jet
$E_T^{Jet} > 7$ GeV

QCD after detector simulation

▨ Background

Events per 4 GeV/c^2

m (W + Jet) (GeV/c^2)

FIG.56